Perfusion Estimation in Volumetric Imaging of Contrast Agents

by

Nelson G. Chen

A dissertation submitted in partial fulfillment
of the requirements for the degree of
Doctor of Philosophy
(Biomedical Engineering)
in the University of Michigan
2009

Doctoral Committee:

Professor J. Brian Fowlkes, Co-Chair
Assistant Research Scientist Gerald L. LeCarpentier, Co-Chair
Professor Karl Grosh
Professor Jonathan M. Rubin
Associate Professor Joseph L. Bull

2009

DEDICATION

To all who seek to learn and discover.

Acknowledgements

The past seven years spent conducting the research described in this work has been quite a journey. There had been numerous difficulties encountered, and many ideas were attempted that did not, for lack of a better term, “work.” However, ultimately substantial contributions were made in spite of these problems. In retrospect, certainly particular parts of the work could have been performed differently, and perhaps more rapidly; however, it has been said that research is a continuous learning process, and there was plenty of knowledge that I have today that I did not possess when the work was performed. First and foremost, the work would not have been possible without the presence of my advisors, Drs. Brian Fowlkes and Jerry LeCarpentier, who were always present to answer questions and offer suggestions whenever I thought of almost anything. I would like to take this opportunity to also thank the members of my committee, who have kindly agreed to serve and who have offered valuable suggestions. In addition, the numerous other people of the Ultrasound Group at the Basic Radiological Sciences Division were always ready to offer help when asked.

In retrospect, the most lasting memories are probably some of the earliest ones. Examples include making my earliest scans with the Toshiba Powervision 8000 and being informed by (now Dr.) Oliver Kripfgans that the acoustic output of such a diagnostic system was sufficiently low that it did not pose a risk of harming me. His help with the machine shop was also invaluable, considering how machining was completely

foreign to me when I began. The trip to Jackson together with Catherine Orifici (now Carneal) was worthwhile not only in terms of obtaining experimental materials, but also in terms of seeing a rural side of the state. Dr. Kim Ives was instrumental in assisting with the harvest and preparation of the preserved porcine kidneys that are described. Dr. Aaron Moskalik gave me some of the initial advice on a vessel normalization scheme that ultimately led to the development of the absolute perfusion measurements reported. Finally, Dr. Scott Swanson was always willing to lend whatever equipment needed from his laboratory.

As numerous masters in almost every field have noted, everyone was a beginner once. Using supersaturated water as a background material, and running the translation apparatus at ridiculously slow rates to increase acquisition time are just two examples of actions someone more experienced would not do. Experience only can be developed over time; nevertheless the purpose of publication is hopefully to allow others to build their own experiences on items different from what had already been experienced, saving them the time to go through the same. As one of my former chemistry professors (Dr. Richard Pagni) once remarked years ago, the things that are done right are quickly forgotten, but the unusual mess-ups are remembered for a lifetime.

In addition to the ultrasound-specific knowledge that was taught to me through the course of performing this work, several more general tips in conducting research were learned. First, previous students have stating the importance of conducting periodic “sanity checks” throughout any experimental plan in order to ensure everything is correctly functioning. This emphasis is well placed. Second is the importance in listing one’s assumptions, and examining them when results are unexpected. Usually at least one

assumption is incorrect, and the incorrect assumption led to the unexpected result. Finally, the importance of having graphs plotted on the same scale, and having histograms available for any set of distributed data are invaluable in data analysis.

It is probably impossible to list by name everyone who has helped with the work presented here, simply because there are so many of them. Nevertheless, in addition to everyone already named, I would like to single out Drs. Paul Carson and Jonathan Rubin for their help. Dr. Carson was always willing to offer suggestions that pointed the research in a broader direction, toward having us see the “bigger picture.” Dr. Rubin, in addition to the clinical insights offered during group meetings, was available to answer a variety of flow related questions almost at any time. Dr. Matthew Schipper was instrumental in creating the statistical model presented in chapter 3. Dr. Jamie Myles at the University of Michigan Institute of Clinical Health Research helped with running and modifying the statistical routines run, and was kind enough to listen to me explain in detail the entire experiment and complications from scratch.

Finally, I would like to thank my parents for their support these many years. They were always available in the way only parents can, being there to offer advice and encouragement on almost anything, They were present when I needed support the most, when I felt most like giving up. My father said it best when he reminded me that something truly worth doing would not be easy; if it were, someone would have already done it long ago.

Table of Contents

List of Figures

List of Tables

Table

Abstract

Perfusion Estimation in Volumetric Imaging of Ultrasound Contrast Agents

by

Nelson G. Chen

Co-Chairs: J. Brian Fowlkes and Gerald L. LeCarpentier

This dissertation presents research involving the investigation of perfusion measured using volumetric imaging of ultrasound contrast agents. Ultrasound contrast agents are micrometer-sized gas bubbles that track the blood circulation. They strongly reflect ultrasound; therefore, a small quantity of agent produces strong echoes, enabling the examination of microcirculation.

The development of three-dimensional ultrasound has led to entire tissue volumes being imaged. Such imaging, now even being performed with two-dimensional arrays, provides more information for diagnostic purposes. Therefore, exploration of contrast imaging in three-dimensions is needed to determine potential benefits in clinical use.

The study of blood flow using contrast agent has been dominated by the imaging of contrast refill into a volume previously cleared of contrast. First, a mechanical method of performing contrast clearance/refill in a three-dimensional volume using two one-dimensional arrays is introduced. The method generated expected volumetric contrast

images in a perfused tube phantom, based on the well-known parabolic velocity profiles of laminar flow. This consistency showed that the mechanical method properly images the refill into a volume at every time after contrast clearance.

Second, the apparatus was applied to a perfused kidney phantom. Refill curves were obtained for the kidney cortex throughout the volume. Refill curves were also obtained using a modified interval imaging technique for comparison. A normalization scheme, which uses the renal artery as a measure of the instantaneous contrast signal intensity, was used to correct for contrast degradation, and to make absolute perfusion estimates. No significant difference was observed between the volumetric perfusion measurements and those obtained from the modified interval imaging, suggesting the independence of refill curves from contrast clearance volume.

Finally, a general form of the normalization scheme was developed that permits normalization from a generic large vessel. The model was tested by imaging different-sized tubes at two orientations, and examining the normalization factor derived. Comparisons were made to values obtained using simpler approaches (global mean and attenuation only models). Values obtained using the model were similar across tube sizes, and were generally larger than those obtained otherwise. Both partial voluming and contrast attenuation are shown to play substantial roles in proper normalization.

Chapter 1

Introduction

1.1 Ultrasound contrast agents – an overview

Ever since the discovery that gas bubbles introduced into the blood circulation cause an opacification in ultrasound imaging [1-2], various ultrasound contrast agents have been developed. The agents have been used to image a variety of organs and tissues. In the liver, the relative vascularity as determined by the imaging of normal parenchyma was compared to that of hemangiomas, hepatocellular carcinomas, and metastases [3]. In the breast, signal enhancement of color Doppler signals upon contrast injection was greater and longer in malignant tumors than benign ones, and the use of contrast agent enabled the accurate differentiation of benign from malignant tumors [4]. For the prostate, infusion of contrast agent increased the diagnostic sensitivity for prostate cancer from 38% to 65% ($p<0.004$) without sacrificing specificity (insignificant difference of 83% vs. 80%) [5]. A thrombus-specific agent, MRX-408, was shown to improve visualization ($p<0.0001$) of thrombi in arteriovenous fistulae [6]. Differences in canine renal perfusion upon the infusion of drugs bradykinin ($p<0.01$) and norepinephrine ($p<0.01$) were measured using contrast washout time [7]. A similar study [8] was able to

produce results correlated ($R=0.92$, $p<0.01$) with values obtained using a magnetic flow meter for ten blood flow input rates (16-125 mL/min). A third study, made with an albumin-based agent, also measured renal perfusion values that were correlated to electromagnetic flow meter inputs [9]. Subsequently, contrast agents were found to be feasible for determining relative blood flow in transplanted kidneys during surgery [10].

Ultrasound contrast agents typically consist of gas microbubbles with a size of less than 7 μm of either free or encapsulated gas and are capable of passing through the circulation [11]. They are typically injected intravenously into the circulatory system in order to highlight the underlying circulation, and especially flow within capillaries. This dissertation explores the imaging of ultrasound contrast agents in three-dimensions, and the use of the agents in obtaining absolute perfusion.

Ultrasound contrast agents enhance the images of the circulating blood volume by essentially becoming a collection of strong scatterers that are distributed throughout the blood volume after being injected into a vessel. The echoes arising from a dilute suspension (as low as 0.025 mL/kg [12]) of contrast agent are strong, due to the compressibility of the agent relative to blood, resulting in a cross-section scattering ratio of 10^{14} to 1 [13]. In addition, resonant effects play a large role in medical imaging. When insonated near their resonant frequencies, which incidentally are similar to the frequencies employed in diagnostic ultrasound, gas bubbles act as scatterers up to 1000 stronger than what would be expected for their size [12]. The bubbles delineate major blood vessels, and opacify perfused vascular beds by brightening the underlying capillaries, each of which is of subresolution size when imaged at typical (<10 MHz) frequencies. Since contrast agent scatters sound so effectively, a small quantity of agent

(such as 10 μL/kg/min) [14]) infused at a constant rate is sufficient to enhance the imaging target with minimal disruption of the underlying circulation.

Contrast agents include the air-filled agents Albunex, Echovist, Levovist, Myomap, Quantison, and Sonavist, as well as the perfluorocarbon filled agents BR14, Definity, Echogen, Imagent-Imavist, Optison, and Sonazoid. The agent SonoVue is filled with sulfur hexafluoride [15]. The air-filled agents are considered “first-generation,” and agents filled with other gases considered “second-generation.” Second-generation agents used gases that had low diffusion and saturation constants, and therefore were more stable than the first-generation agents, enabling the performance of perfusion studies. The ideal agent is (1) stable over time while being sufficiently fragile to be readily disrupted by ultrasound, (2) be neutrally charged and sufficiently small so that it freely transits the microcirculation, (3) not cause excessive attenuation, which can make image interpretation difficult, and (4) be readily used by physicians and nurses at the bedside [16]. Compensation for insufficient agent stability over the course of the experiment plays a substantial role in the analysis of the experimental data presented in chapter 3.

Currently, the use of contrast agents is indicated clinically in cases where suboptimal echocardiograms are obtained without contrast agent. The Food and Drug Administration (FDA) of the United States has currently only approved the agents Definity and Optison for clinical use [17]. The agent is used to opacify the left ventricle and to help outline the left ventricular endocardial border [18-19]. In Europe, the European Federation of Societies for Ultrasound in Medicine and Biology (EFSUMB) has published guidelines for the use of agents in liver ultrasound. Contrast enhanced ultrasound is indicated for liver scans in order to (1) characterize ambiguous, previously

undetected lesions in order to determine whether the lesion is benign (hemangioma or focal nodular hyperplasia) or malignant (hepatocellular carcinoma), (2) diagnose hepatocellular carcinoma in a cirrhotic liver, (3) detect possible liver metastases in patients diagnosed with cancer elsewhere, and (4) guide and monitor tumor ablation procedures [20].

1.2 Imaging of ultrasound contrast agents

When a contrast bubble is insonated, it can have one of three possible responses depending on the insonation pressure, which is often quoted as the mechanical index. The mechanical index (MI) is defined as follows [21]

$$MI = \frac{P_{r.3}}{C_{MI}\sqrt{f_c}}. \qquad \textbf{(1.1)}$$

where $P_{r.3}$ is the peak rarefactional pressure in water in MPa derated by a factor of 0.3 dB/cm/MHz to account for tissue attenuation. C_{MI} is the constant value of 1 MPa-MHz$^{0.5}$ making the MI a dimensionless quantity, and f_c is the transducer center frequency in MHz. If the insonation pressure is sufficiently low (mechanical index MI≤0.1), the bubble oscillates almost linearly with compression and rarefaction amplitudes being nearly equal. At higher pressures (MI between 0.2 and 0.7), the rarefaction amplitude becomes larger than the compression amplitude [22]. Integer harmonics of the transmitted pulse are generated, along with a subharmonic (one-half of transmit) and ultraharmonics (integer multiples of the subharmonic) [11]. Finally, at even larger pressures, the contrast agent is “destroyed” as the bubble is ruptured and a large transient signal is produced [22].

Ideally, infused contrast agent would be imaged in isolation from the underlying tissue structures when examining blood flow. This isolation has been partially achieved through harmonic imaging, most notably through second harmonic imaging [23]. Here, the transducer is set to process only signals with a center frequency two times the center transmit frequency. Since underlying tissue behaves almost linearly, and therefore generating little harmonic signal, while contrast agent that is sufficiently excited generates harmonic signals, second harmonic imaging results in the contrast agent being preferentially displayed. This preferential display of the contrast over tissue is termed tissue suppression. Tissue suppression by using second harmonic imaging, however, is an imperfect process due to both the slight nonlinear behavior of the tissue, and the overlap of the transmit and receive bandwidths as illustrated in Fig. 1.1. Imaging of the higher harmonics has been limited by transducer bandwidth.

The development of pulse-inversion imaging, also known as phase inversion imaging, is a further attempt to improve tissue suppression in ultrasound contrast imaging [24]. Here, two sufficiently overlapping pulses are transmitted, with the second pulse being the inverse of the first (or equivalently, the second pulse is 180 degrees out of phase with respect to the first). The received signals from each pulse are then summed. The signals from tissue, which is almost linear, cancel while the nonlinear contrast signals add as shown in Fig. 1.2. Nevertheless, some residual tissue signal remains.

Therefore, in experimental quantitative image analysis sometimes images containing no contrast agent are obtained as a baseline using identical machine settings as that used to obtain the contrast images in question. The nonzero baseline is then subtracted from whatever acquired contrast images prior to subsequent processing. This

process is termed baseline subtraction. Baseline subtraction does not account for the effects of speckle; the contrast images will have different speckle patterns from the tissue baseline, and therefore the subtraction process will not completely remove the tissue signal from every location. However, since the echoes arising from contrast agent are typically substantially larger than residual tissue signal, these speckle effects are usually negligible. Subharmonic imaging has been shown to give excellent tissue suppression, and therefore it would make baseline subtraction unnecessary; however, it requires the transmission of narrowband pulses that restrict the achievable resolution [11]. *In vivo*, baseline subtraction is difficult due to motion, and a successful subtraction would require that the contrast enhanced and baseline images be properly registered. As such, baseline subtraction is not typically performed for such studies.

1.3 Study rationale

Perfusion is the amount of fluid (usually blood) that passes through a tissue per unit volume per unit time. Doppler imaging has traditionally been used to image blood flow, in spite of its directionality and sensitivity limitations. For example, malignant breast tumors have been subjectively observed using color Doppler imaging to be hyperperfused, and to have high-velocity flow relative to benign tumors [25]. A later study showed that 99 of 104 cases of benign breast tumors showed no color Doppler signal, while 57 out of 58 cancers had detectable vessels (and hence detectable increases in perfusion) [26]. An automated scheme was developed to quantify (mean pixel density and mean pixel value) color Doppler images [27] and application to malignant breast tumors again showed increased perfusion [28] relative to benign lesions. A further color

Doppler study [4] indicated that the addition of contrast agent caused subjective increases in Doppler signal intensity and duration, as well as increased vessel density and tortuousity in malignant breast tumors. Arteriovenous shunts were observed in the malignant tumors but not in benign ones. The differences in vascular structure histologically found between malignant and benign tumors correlated with the differences observed using color Doppler [29]. As such, visualizing and mapping the perfusion within and surrounding tumors may help differentiate between malignant and benign masses as well as in tumor detection since tumors generally have perfusion values differing from their surrounding tissue [30]. The perfusion level of a tumor can be greater or less than its surroundings; much depends on the type of surrounding tissue, depending on whether it has a high or low metabolic rate. Tumors themselves typically become hypoperfused over time; the tumor outgrows the ability of the circulation to adequately maintain its metabolism and the interiors of tumors are often necrotic. On the other hand, infiltrative tumors often have perfusion values greater than its surroundings.

Extending the imaging into 3D may further improve the ability of discriminating between benign and malignant masses by providing an improved “feel” of the vascular structure for the reader [31] in the case of Doppler scans and increasing the sampling of vascular signals in and around masses. Doppler volumetric scans with various quantitative blood-flow measures such as speed-weighted pixel density (SWD), the vascularization index (VI), flow index (FI), and the vascularization flow index (VFI) (the latter three indices being derived from the VOCAL (virtual organ computer-aided analysis) package) have been conducted in a variety of organs. Examples include breast [31-33], prostate [34-36], uterus [37], placenta [38], and ovary [39]. Various studies

which show the advantages of 3D ultrasound with and without contrast enhancement relative to 2D scans in the detection and staging of prostate cancer are reviewed in [40]. Three-dimensional gray-scale ultrasound showed increased sensitivity (88% versus 72%) and decreased specificity (42% versus 54%) relative to two-dimensional scans in terms of differentiating prostate cancer from benign prostate hyperplasia. Staging accuracy was 94% versus 72% ($p<0.05$) for gray-scale 3D versus 2D scans. Doppler measurements are subject to limitations in the Doppler signal especially of slow capillary flow, which are not detected with standard techniques. Doppler ultrasound detects *macrovessel* flow rather than microvessel flow [41]. Therefore, the blood volume of a capillary dense tissue would be especially underestimated [41] and therefore the perfusion systematically underestimated as well. The one study that did not show an advantage of 3D versus 2D ultrasound [33] in distinguishing between malignant and benign breast masses nevertheless suggested that the masses exhibited differences in the way contrast passed through after contrast agent administration. Hence, overall perfusion, including microvessel flow, as measured using contrast agent in 3D may be a useful tool in characterizing tissues.

Other techniques have been also devised for measuring tissue perfusion. Several other modalities that have been used for perfusion measurements include gas washout, heat diffusion, isotope trapping, radiolabeled microspheres, laser Doppler flow, computed tomography, MRI, and positron emission tomography (PET) [42-43]. These approaches have some drawbacks, including: (1) being invasive, (2) having limited availability, (3) generating hemodynamic effects/artifacts through the measurement process, or (4) filtering of the tracers in question [44]. Some of these techniques cannot be used for *in*

vivo examination, and some cannot be repeated. Perfusion measurements made using contrast-enhanced ultrasound have several advantages over measurements made using these other modalities. Contrast-enhanced ultrasound is especially suitable for highlighting capillary flow because ultrasound contrast agent can be assumed non-diffusible [45] unlike MRI contrast agent. In addition, contrast-enhanced ultrasound is not subject to the directionality issues affecting Doppler measurements.

1.4 Quantification of blood flow measurements

Numerous studies such as the cardiac reperfusion study [46] have demonstrated how ultrasound contrast agents can be used to determine whether a tissue in question is underperfused compared to its surroundings by examining the relative fractional moving blood volumes. The quantification of blood flow measurements which account for the mean speed with which blood passes within tissues using ultrasound contrast agent has been described in the seminal paper [47] that introduced the concept of a contrast refill curve.

Even though historically the imaging of contrast agent in real-time using essentially nondestructive pulses was developed subsequent to imaging in high power, the description of a contrast refill curve is simplified by first considering the case of nondestructive imaging pulses (described in [48]). Initially, a series of high power pulses clear a volume of contrast. Upon the cessation of the high power insonation, contrast agent from surrounding vessels refills the volume with time. The refill process is monitored by the imaging pulses in real time as illustrated in Fig. 1.3, and the contrast intensity can be fit with the exponential expression $y(t) = A*[1-\exp(-t/MTT)]$, where *MTT*

is the mean transit time, *t* is time, and *A* the asymptotic value, which equals the intensity level of the contrast-filled tissue prior to contrast clearance. Other expressions such as a sigmoidal curve [49] and an error function [50-51] have been developed for fitting the contrast intensities. The sigmoidal curve accounts for the sometimes observed entrance phenomenon, caused by partial contrast destruction in the vessels supplying the region of interest after contrast clearance. The error function fit takes into account the elevational beam shape, and differences between the contrast clearance and readout zones. However, as yet, neither of these methods have been widely used, presumably because they introduce additional parameters unique to each imaging system. Accounting for beam shape effects plays a significant role in the material presented in chapters 3 and 4. The refill curve can also be obtained using a series of contrast clearances and differing subsequent delays to fill in the refill curve in what has come to be known as interval imaging [3, 52-53] as illustrated in Fig. 1.4, which however is no longer obtained in real-time. Any slight signal remaining after contrast clearance, arising from imperfect tissue suppression is removed using baseline subtraction when possible, such as when imaging a stationary object in the laboratory. Otherwise, the tissue baseline is either ignored, or an estimate of its intensity level is independently made and it is subtracted from all measured values. The dual transducer technique, introduced in chapter 2, modifies interval imaging in order to obtain the contrast refill of entire volumes at every selected interval.

With the parameters of a refill curve, the relative perfusion among tissues in question is A/MTT, or the initial slope of the refill curve. For direct comparison between image acquisitions and to perfusion measurements obtained using other methods,

estimation of the value of *A* corresponding to pure circulating blood is needed for a given infusion. The estimation is performed through examination of one or more relatively large vessels present within the image. Without this information, the comparison of perfusion measurements to those obtained otherwise can only be relative (i.e. the perfusion measured using one method is correlated with the perfusion measured using another method, such as that reported by Forsberg [54]).

1.5 Contribution of dissertation

The focus of this dissertation is on the effect of imaging of contrast destruction/refill in three spatial dimensions as a function of time (hence the references to both 3D and 4D imaging), and the effects of this imaging on the estimated contrast refill curve. The recent development of 2D arrays has allowed ultrasound scanners to collect volumetric images. Volumetric imaging has numerous advantages over conventional imaging in two dimensions. The acquisition of the volume directly permits the operator to avoid having to mentally integrate a series of 2D images in order to visualize the volume. In addition, the image is far more reproducible since there is no need to reimage the same plane, such as to monitor treatment progress (imaging the same or similar volume is enough). Finally, volumetric measurements are more accurate [55]. Although 2D arrays were not yet widely available at the time the work described was performed, the results obtained are nevertheless readily generalized to the volumetric images acquired. Imaging contrast destruction/refill in three vs. two spatial dimensions involves potential differences in contrast clearance and refill patterns, which could affect the resulting refill curve measurements.

The following chapters are arranged in the order in which the work was completed. An overview of each chapter follows.

Chapter 2 describes the dual transducer mechanical scheme used to achieve contrast clearance and refill that was used for the studies. Two 1D arrays were mounted and translated as a unit; the leading transducer cleared contrast, and the lagging transducer imaged the amount of contrast in the tissue after known, fixed times *t*. A tube phantom was imaged using this apparatus, with expected and observed contrast profiles compared. The phantom was designed to provide laminar fluid flow such that a composite contrast position profile was known. The imaging of the tube phantom indicated that the contrast agent does follow expected behavior when cleared and imaged in time and space. The relevant citation is

> Chen NG, Fowlkes JB, Carson PL, LeCarpentier GL. Rapid 3D Imaging of Contrast Flow: Demonstration of a Dual Beam Technique. Ultrasound Med Biol 2007; 33(6): 915-923.

Chapter 3 describes the use of the apparatus from chapter 2 to image a preserved porcine kidney that provided a vascular bed within which contrast agent was perfused. Perfusion was estimated at two different flow rates at locations within the entire volume. A normalization scheme was developed in order to account for both the drop in contrast signal over the course of the experiment and the level of contrast signal in the circulated "blood" (actually water with suspended contrast). As previously described, knowledge of this estimate is necessary in order to estimate absolute perfusion. Perfusion estimates at

the higher flow rate were consistent with thermal diffusion estimates reported in the literature [56]. Perfusion estimates at a given slice plane were consistent between measurements taken using the dual transducer apparatus and that taken using a modified low power interval imaging technique, which suggests that contrast refill is independent of contrast clearance volume.

Chapter 4 expands upon the normalization scheme presented in chapter 3 to different sized vessels oriented at differing orientations. The model was shown to give similar intensity values for contrast agent for pairs of perfused vessels of different sizes. The values predicted generally were larger than those values that would have been obtained using two simpler approaches, namely taking the global mean of the intensity values, and compensating solely for contrast attenuation. The results suggest that partial voluming effects play a significant role in the estimation of A for vessels likely to be encountered *in vivo*. Methods for beam width estimation are described, both *in vitro* and *in vivo*.

Chapter 5 summarizes the achievements of this work, and discusses possible directions for future work based from this work. Dynamic estimation of the contrast agent intensity together with the use of multiple vessels, further accounting of vessel geometry, and the generation of perfusion maps are discussed.

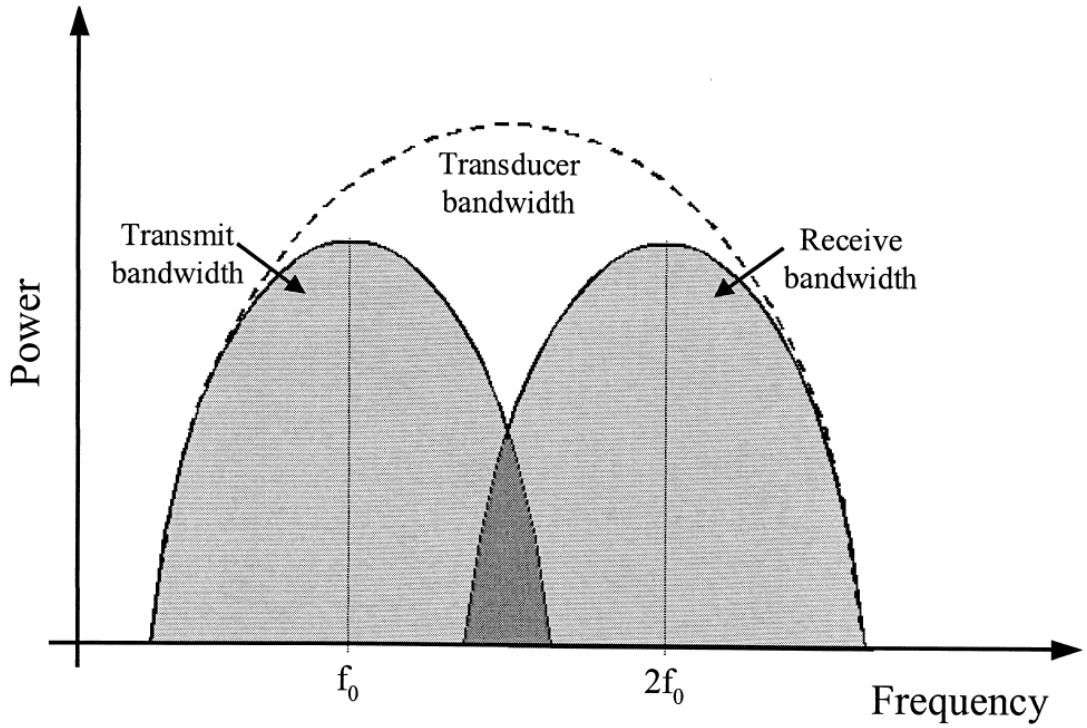

Fig. 1.1. Overlap of transmit and receive bandwidths. When imaging at the second harmonic, some of the fundamental transmit frequencies signal contains frequencies that overlap with the receive frequencies [11] (reprinted with permission).

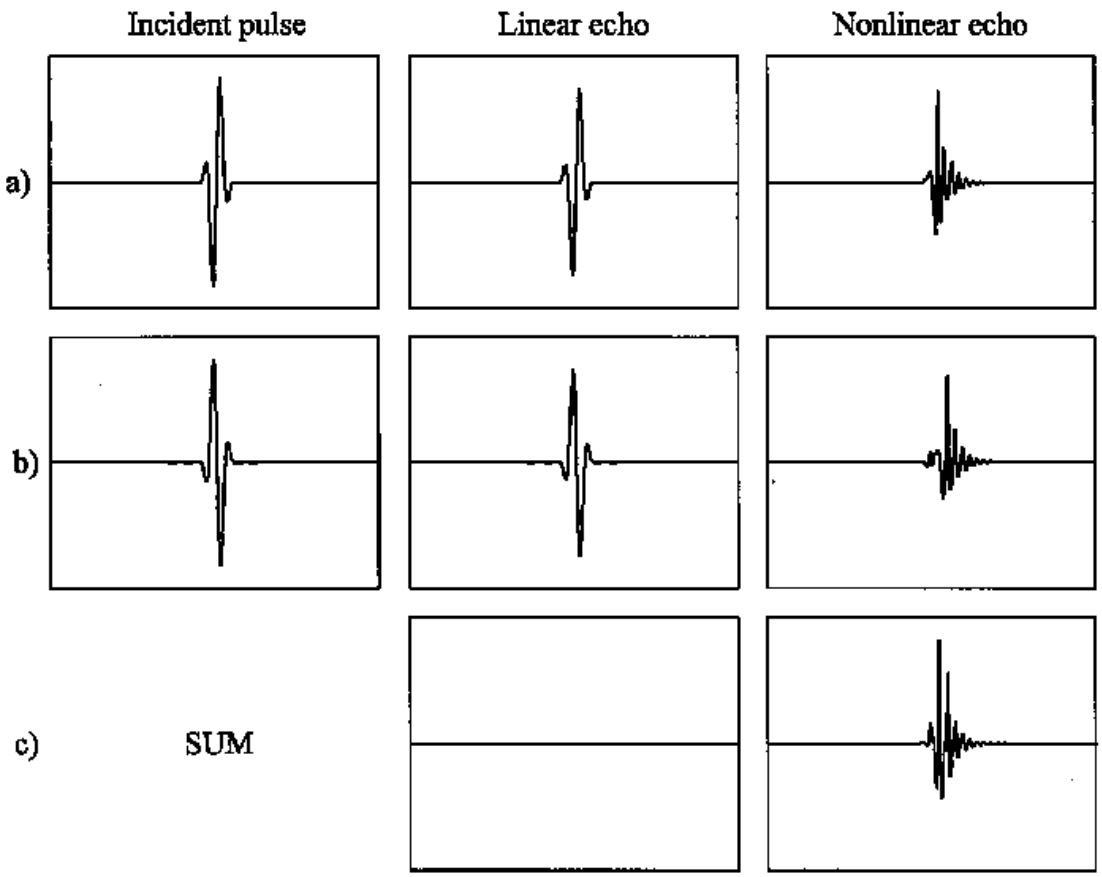

Fig 1.2. Illustration of pulse-inversion imaging. In pulse inversion imaging, two incident pulses are transmitted down each scan line that are 180º out-of-phase, and the echoes recorded and summed. In the case of linear scattering, the echoes cancel. For nonlinear scatterers such as ultrasound contrast agents however, the echoes do not cancel. Hence pulse-inversion imaging is useful in achieving tissue suppression [11] (reprinted with permission).

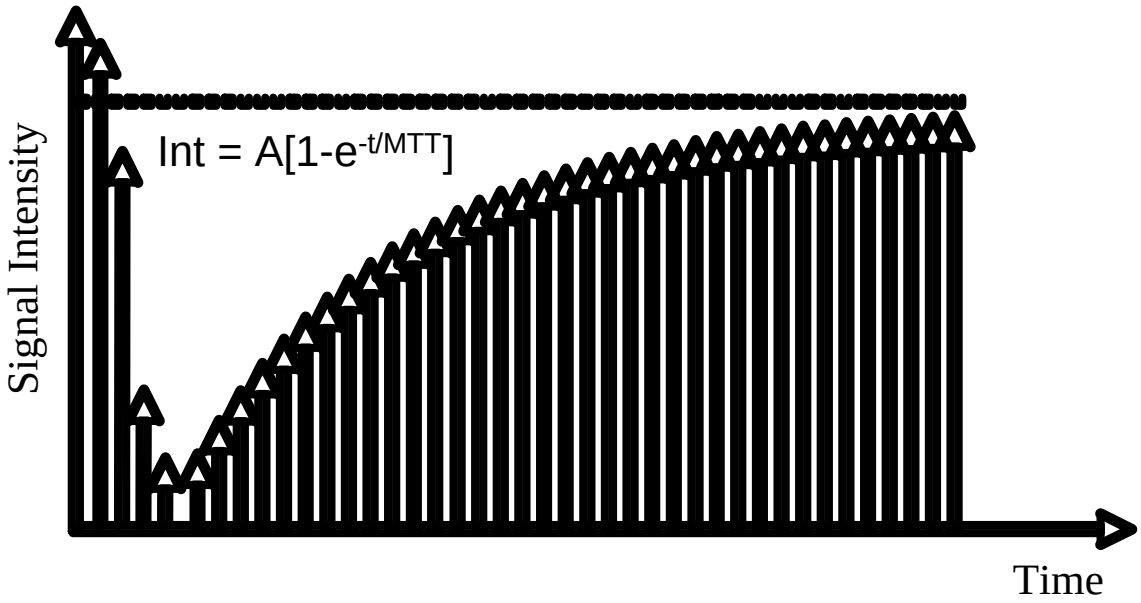

Fig 1.3. Real-time refill curve. After a volume is cleared of contrast agent with a series of high-power pulses, contrast agent from outside the volume begins to refill the "negative bolus." The refill process can be monitored in real-time using a series of low power pulses in what is known as real-time imaging. The refill curve is typically fit to an exponential expression, with asymptotic value *A* and mean transit time *MTT*. Relative perfusion is the initial slope of the curve, or *A*/*MTT*.

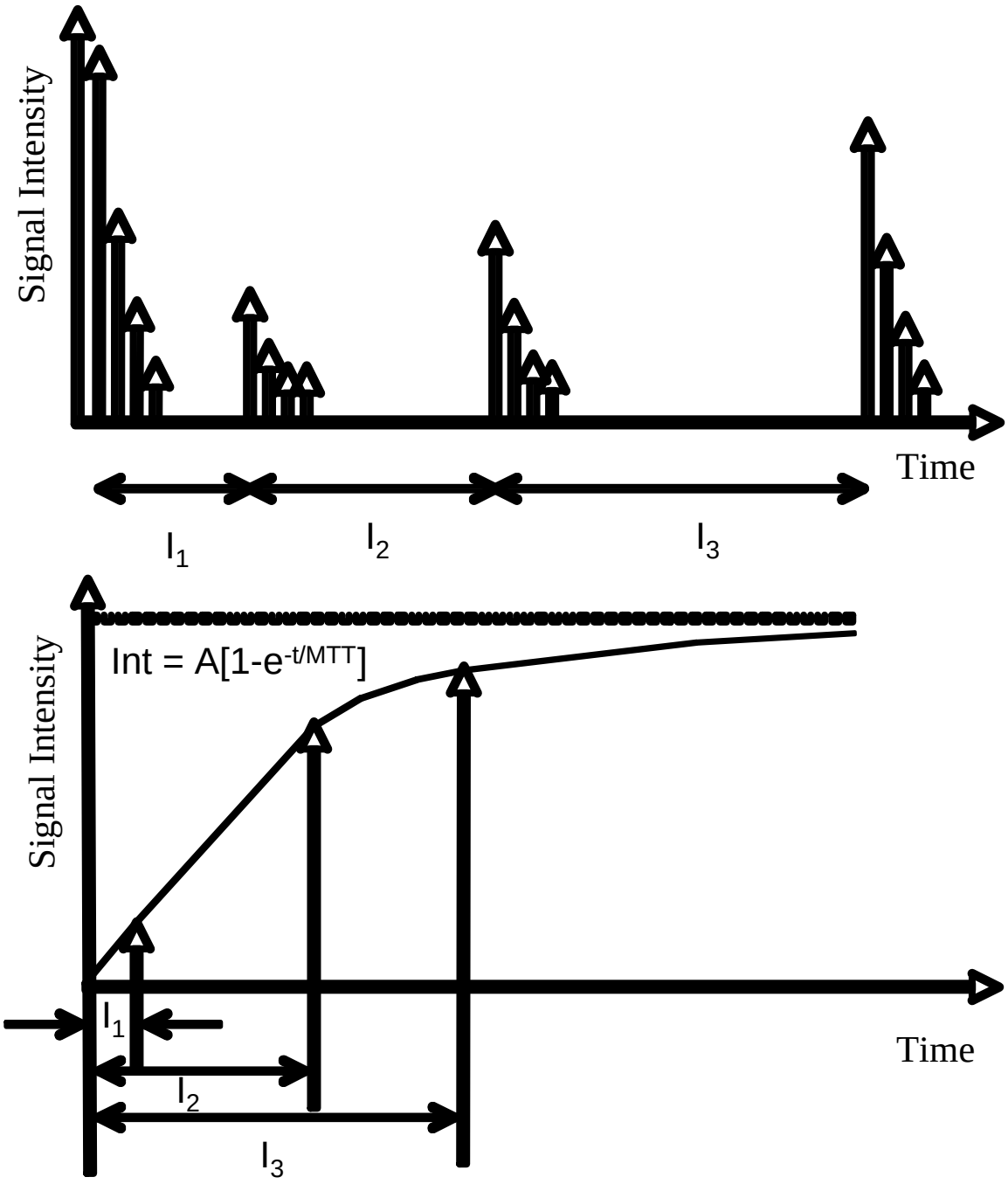

Fig. 1.4. Interval imaging. Historically developed prior to real-time refill, the interval imaging process involves clearing contrast with a series of high-power pulses following by imaging the contrast that has refilled after various intervals *I*. The combination of the resultant signal intensities at different values of *I* is then fitted to a refill curve.

1.6 References

[1] Gramiak R, Shah PM. Echocardiography of the aortic root. Invest. Radiol. 1968; 3:356-366.

[2] Gramiak R, Shah PM, Kramer DH. Ultrasound cardiography: Contrast studies in anatomy and function. Radiology 1969; 92: 939.

[3] Wilson SR, Burns PN, Muradali D, Wilson JA, Lai X. Harmonic hepatic US with microbubble contrast agent: initial experience showing improved characterization of hemangioma, hepatocellular carcinoma, and metastasis. Radiology 2000; 215: 153-161.

[4] Kedar RP, Cosgrove D, McCready VR, Bamber JC, Carter ER. Microbubble contrast agent for color Doppler US: effect on breast masses. Work in progress. Radiology 1996; 198: 679-686.

[5] Halpern EJ, Rosenberg M, Gomella LG. Prostate cancer: contrast enhanced us for detection. Radiology 2001; 219: 219-225.

[6] Unger E, Metzger P 3rd, Krupinski E, Baker M, Hulett R, Gabaeff D, Mills J, Ihnat D, McCreery T. The use of a thrombus-specific ultrasound contrast agent to detect thrombus in arterioveneous fistulae. Invest Radiol 2000; 35: 86-89.

[7] Lang RM, Feinstein SB, Powsner SM, McCoy CE, Frederickson ED, Neumann A, Goldberg LI, Borow KM. Contrast ultrasonography of the kidney: a new method for evaluation of renal perfusion *in vivo*. Circulation 1987; 75: 229-234.

[8] Voci P, Heidenreich P, Aronson S, Wiencek JG, Zaroff JG, Feinstein SB, Reale A. Quantitation of renal blood flow by contrast ultrasonography: preliminary results. Cardiologia 1989; 34: 1001-1006.

[9] Aronson S, Feinstein S, Walker R, Heidenreich P, Zaroff JG, Walker R, Roizen MF. Assessment of renal blood flow with contrast ultrasonography. Anesth Analg 1993; 76: 964-970.

[10] Aronson S, Thristelwaite R, Walker R, Beezhold C, Feinstein SB. Safety and feasibility of renal blood flow determination during kidney surgery with perfusion ultrasonography. Anesth Analg 1995; 80: 353-359.

[11] Frinking PJA, Bouakaz A, Kirkhorn J, Ten Cate FJ, De Jong N. Ultrasound Contrast Imaging: Current and New Potential Methods. Ultrasound Med Biol 2000; 26(6) 965-975.

[12] Goldberg BB, Liu JB, Forsberg F. Ultrasound contrast agents: a review. Ultrasound Med Biol 1994; 20: 319-333.

[13] Ophir J, Parker KJ. Contrast agents in diagnostic ultrasound. Ultrasound Med Biol 1989; 15:319-333.

[14] Potdevin TCU, Fowlkes JB, Moskalik AP, Carson PL. Refill model of rabbit kidney vasculature. Ultrasound Med Biol 2006; 32(9): 1331-1338.

[15] Quaia E. Microbubble ultrasound contrast agents: an update. Eur Radiol 2007; 17: 1995-2008.

[16] Miller AP, Nanda NC. New agents in contrast echocardiography. Ultrasound Med Biol 2004; 30(4): 425-434.

[17] United States Food and Drug Administration Center for Drug Evaluation and Research. Information for Healthcare Professionals Micro-bubble Contrast Agents (marketed as Definity (Perflutren Lipid Microsphere) Injectable Suspension and Optison (Perflutren Protein-Type A Microspheres for Injection). Silver Spring MD, USA: FDA Alert. October 2007 (updated July 2008). http://www.fda.gov/cder/drug/InfoSheets/HCP/microbubbleHCP.htm.

[18] Lantheus Medical Imaging. Definity Vial for Perflutren Lipid Microsphere Injectable Suspension (package insert). N Billerica MA, USA: Lantheus Medical Imaging. April 2008.

[19] Amersham Health. OPTISON™ (Perflutren Protein-Type A Microspheres for Injection, USP) (package insert). Princeton NJ, USA: Amersham Health Inc. June 2003.

[20] Albrecht T, Blomley M, Bolondi L, Claudon M, Correas JM, Cosgrove D, Greiner L, Jäger K, de Jong N, Leen E, Lencioni R, Lindsell D, Martegani A, Solbiati L, Thorelius L, Tranquart F, Weskott HP, Whittingham T. EFSUMB Study Group (2004). Guidelines for the use of contrast agents in ultrasound. January 2004. Ultraschall Med 25:249–256.

[21] American Institute of Ultrasound in Medicine, National Electrical Manufacturers Association. Acoustic Output Measurement and Labeling Standard for Diagnostic Ultrasound Equipment. Rockville, MD: American Institute of Ultrasound in Medicine; Rosslyn, VA: National Electrical Manufacturers Association. 1992.

[22] Becher H, Burns PN. Handbook of contrast echocardiography: Left ventricular function and myocardial perfusion. Heidelberg: Springer Verlag. 2000.

[23] Burns PN. Contrast agents for Doppler ultrasound. In: Taylor KJW, Burns PN, Wells PNT (eds) Clinical Applications of Doppler ultrasound, 2nd edn. Raven, New York, 367-379. 1995.

[24] Hope Simpson D, Chin CT, Burns PN. Pulse inversion Doppler: A new method for detecting nonlinear echoes from microbubble contrast agents. IEEE Trans Ultrason Ferr Freq Cont 1999; 46(2): 372-382.

[25] Cosgrove DO, Bamber JC, Davey JB, McKinna JA, Sinnett HD. Color Doppler signals from breast tumors. Work in progress. Radiology 1990; 176(1): 175-180.

[26] Cosgrove DO, Kedar RP, Bamber JC, Almurrani B, Davey JBN, Fisher C, McKinna JA, Svensson WE, Tohno E, Vagios E, Alsanjari NA. Breast Diseases - Color Doppler US in Differential-Diagnosis. Radiology 1993; 189(1): 99-104.

[27] Delorme S, Weisser G, Zuna I, Fein M, Lorenz A, VanKaick G. Quantitative characterization of color Doppler images: Reproducibility, accuracy and limitations. J Clin Ultrasound 1995; 23(9): 537-550.

[28] Kedar RP, Cosgrove DO, Bamber JC, Bell DS. Automated quantification of color Doppler signals: A preliminary study in breast tumors. Radiology 1995; 197(1): 39-43.

[29] Lee WJ, Chu JS, Huang CS, Chang MF, Chang KJ, Chem KM. Breast cancer vascularity: color Doppler sonography and histopathology study. Breast Cancer Res Treat 1996; 37(3): 291-298.

[30] Vaupel P, Kallinowski F, Okunieff P. Blood flow, oxygen and nutrient supply, and metabolic microenvironments of human tumors: A review. Cancer Research 1989; 49(23): 6449-6465.

[31] Carson PL, Moskalik AP, Govil A, Roubidoux MA, Fowlkes JB, Normolle D, Adler DD, Rubin JM, Helvie M. The 3D and 2D color flow display of breast masses. Ultrasound Med Biol 1997; 23(6): 837-49.

[32] Bhatti PT, LeCarpentier GL, Roubidoux MA, Fowlkes JB, Helvie MA, Carson PL. Discrimination of sonographically detected breast masses using frequency shift color Doppler imaging in combination with age and gray scale criteria. J Ultrasound Med 2001; 20(4): 343-50.

[33] Hochmuth A, Boehm T, Bitzer C, Fleck M, Schneider A, Kaiser WA. Differentiation of breast masses using 3-D sonographic and echo-enhancer-based evaluation of the vascular pattern: Initial experiences. Ultrasound Med Biol 2002; 28(7): 845-851.

[34] Moskalik A, Carson PL, Rubin JM, Bree RL, Fowlkes JB, Rubin MA, Wojno K, Manley S, Montie JE. Analysis of three-dimensional ultrasound Doppler for the detection of prostate cancer. Urology 2001; 57(6): 1128-32.

[35] Moskalik AP, Rubin MA, Wojno KJ, Bree R, Rubin JM, Fowlkes JB, Montie JE, Manley S, Carson PL. Analysis of three-dimensional Doppler ultrasonographic quantitative measures for the discrimination of prostate cancer. J Ultrasound Med 2001; 20(7): 713-22.

[36] Potdevin TC, Moskalik AP, Fowlkes JB, Bude RO, Carson PL. Doppler quantitative measures by region to discriminate prostate cancer. Ultrasound Med Biol 2001; 27(10): 1305-10.

[37] Jokubkiene L, Sladkevicius P, Rovas L, Valentin L. Assessment of changes in endometrial and subendometrial volume and vascularity during the normal menstrual cycle using three-dimensional power Doppler ultrasound. Ultrasound Obstet Gynecol 2006; 27:672-679.

[38] Merce LT, Barco MJ, Bau S, Kupesic S, Kurjak A. Assessment of placental vascularization by three-dimensional power Doppler “vascular biopsy” in normal pregnancies. Croat Med J 2005; 46(5): 765-771.

[39] Chan CCW, Ng EHY, Li CF, Ho PC. Impaired ovarian blood flow and reduced antral follicle count following laparoscopic salpingectomy for ectopic pregnancy. Hum Reprod 2003; 18(10): 2175-2180.

[40] Mehta SS, Azzouzi AR, Hamdy FC. Three dimensional ultrasound and prostate cancer. World J Urol 2004; 22: 339-345.

[41] Peters-Engl C, Medl M, Mirau M, Wanner C, Bilgi S, Sevelda P, Obermair A.. A Color-coded and spectral Doppler flow in breast carcinomas-relationship with the tumor microvasculature. Breast Cancer Res Treat 1998; 47(1): 83-89.

[41] Rubin JM, Adler RS, Fowlkes JB, Spratt S, Pallister JE, Chen JF, Carson PL. Fractional moving blood volume: estimation with power Doppler US. Radiology 1995; 197: 183-190.

[42] Aukland K. Methods for measuring renal blood flow: total flow and regional distribution. Ann Rev Physiol 1980; 42: 543-555.

[43] Young LS, Regan MC, Barry MK, Geraghty JG, Fitzpatrick JM. Methods of renal blood flow measurement. Urol Res 1996; 24(3) 149-160.

[44] Wei K, Le E, Bin JP, Coggins BA, Thorpe J, Kaul S. Quantification of renal blood flow with contrast-enhanced ultrasound. J Am Coll Cardiol 2001; 37(4): 1135-1140.

[45] Lucidarme O, Kono Y, Corbeil J, Choi SH, Golmard JL, Varner J, Mattrey RF. Angiogenesis: Noninvasive Quantitative Assessment with Contrast-enhanced Functional US in Murine Model. Radiology 2006; 239(3): 730-739.

[46] Ito H, Tomooka T, Sakai N, Yu H, Higashino Y, Fujii K, Matsuyama T, Kitabatake A, Minamino T. Lack of myocardial perfusion immediately after successful thrombolysis. A predictor of poor recovery of left ventricular function in anterior myocardial infarction. Circulation 1992; 85: 1699-1705.

[47] Wei K, Jayaweera AR, Firoozan S, Linka A, Skyba DM, Kaul S. Quantification of myocardial blood flow with ultrasound-induced destruction of microbubbles administered as a constant infusion. Circulation 1998; 97: 473-483.

[48] Tiemann K, Lohmeier S, Kuntz S, Koster J, Burns PN, Porter TR, Becher H. Real-time contrast echo assessment of myocardial perfusion at low emission power: first experimental and clinical results using power pulse inversion imaging. Echocardiography 1999; 16: 799-809.

[49] Lucidarme O, Franchi-Abella S, Correas JM, Bridal S, Kurtisovski E, Berger G. Blood flow quantification with contrast-enhanced US: “Entrance in the section” phenomenon-Phantom and rabbit study. Radiology 2003; 228: 473-479.

[50] Potdevin TC, Fowlkes JB, Moskalik AP, Carson PL. Analysis of refill curve shape in ultrasound contrast agent studies. Med Phys. 2004; 31(3): 623-632.

[51] Arditi M, Frinking PJA, Zhou X, Rognin NG. A New Formalism for the Quantification of Tissue Perfusion by the Destruction-Replenishment Method in Contrast Ultrasound Imaging. IEEE Trans. Ultrason. Ferroelect., Freq. Contr. 2006; 53(6): 1118-1129.

[52] Broillet A, Puginier J, Ventrone R, Schneider M. Assessment of myocardial perfusion by intermittent harmonic power Doppler using SonoVue, a new ultrasound contrast agent. Invest Radiol 1998; 33: 209-215.

[53] Burns PN, Wilson SR, Simpson DH. Pulse inversion imaging of liver blood flow: improved method for characterizing focal masses with microbubble contrast. Invest Radiol 2000; 35: 58-71.

[54] Forsberg F, Liu JB, Shi WT, Ro R, Lipcan KJ, Deng X, Hall AL. *In Vivo* Perfusion Estimation Using Subharmonic Contrast Microbubble Signals. J Ultrasound Med 2006; 25: 15-21.

[55] Fenster A, Surry K, Smith W, Downey DB. The use of three-dimensional ultrasound imaging in breast biopsy and prostate therapy. Measurement 2004; 36: 245:256.

[56] Kraus T, Klar E, Osswald BR, Fernandes L, Mehrabi A, Gebhard MM, Herfarth C. Continuous Measurement of Porcine Renal Cortex Microcirculation with Enhanced Thermal Diffusion Technology. J Surg Res 1996; 61(2): 531-536.

Chapter 2

Development and testing of a dual-transducer apparatus

2.1 Chapter overview

This chapter describes the dual-transducer apparatus that was built using two one-dimensional arrays to investigate the clearance of contrast agent in a volume and its subsequent imaging as contrast agent refills. The dual transducer apparatus permitted the clearance of contrast agent in a volume and its subsequent imaging as contrast agent refills using one-dimensional arrays. The apparatus was tested on a tube phantom. Contrast agent is assumed to track the fluid flow within the phantom. Since the velocity profile for laminar fluid flow through a circular pipe is well known, a composite contrast agent profile as a function of both transducer translation distance and time can be derived. Comparison of the theoretical and experimental profiles allows verification of the three dimensional nature of the contrast clearance and refill. The apparatus was originally intended to permit three-dimensional scanning in a reasonable time without resorting to using two-dimensional arrays. As such, theoretical scan time comparisons are included as an appendix. The chapter is adapted from a previously published paper [1].

2.2 Theory

2.2.1 Development of contrast profile

Assuming that suspended contrast agent tracks the fluid flow within a circular vessel, and assuming that the flow is laminar, the expected contrast profile is derived as follows. First, laminar viscous fluid flow through a straight circular cylinder has a well-known velocity profile given by

$$u(r) = V_c\left[1-\left(\frac{r}{R}\right)^2\right] \quad \textbf{(2.1)}$$

where *u(r)* is the flow velocity at radius *r* from the center, V_c is the center velocity, and *R* the tube radius. This velocity profile is independent of time.

Suppose the cylinder is initially cleared of contrast agent, with fresh agent refilling from the left for position p=0 at time t=0 as illustrated in Fig. 2.1. Then the position of the front of refilled agent $p(r,t)$ is simply $tu(r)$. The front stretches with increasing t. Substituting provides

$$p(r,t) = tu(r) = d = tV_c\left[1-\left(\frac{r}{R}\right)^2\right]. \quad \textbf{(2.2)}$$

Letting *d* represent the distance along the tube where the imaging transducer samples the contrast agent radii, with *d=0* being the initial uniform position of the front at *t=0,* solving for the radius *r* as a function of *d* gives the following expression for *r(d,t)*

$$r(d,t) = R\sqrt{1-\frac{d}{tV_c}} \quad \textbf{(2.3)}$$

Notice how, since the imaging transducer is translated along the length of the tube as the profile stretches, the combination of the contrast cross-sections forms a time-dilated parabola.

2.2.2 Dual transducer technique

A schematic of the dual transducer technique is illustrated in Fig. 2.2. The technique uses two mechanically translated transducers, separated by a known distance *s* and an effective separation distance *s'*<s (arising from the presence of a substantial clearance zone thickness) that are passed over a volume of interest. The clearance transducer is operated at sufficient power and pulse repetition frequency (PRF) to clear the volume of interest of contrast agent during each sweep. The imaging transducer is operated in a minimally destructive mode, and it reads the amount of contrast agent that has refilled since contrast clearance. Both transducers are swept through the volume of interest at constant velocity *v*. Based on the separation distance *s'*, the refill associated with a specific interval Δt can be measured for the entire volume. Additional delay can be added by pausing the sweep after clearance and before imaging.

2.3 Methods

2.3.1 Experimental plan

For a given transducer translation velocity v_T and transducer separation *s* (known from the dual-transducer configuration) and an observed time-dilated parabola, one could

derive the center flow velocity V_c by substituting the expression $v_T t$ - s for d in eqn 2.3, reducing $r(d,t)$ to a function of only t

$$r(d,t) = R\sqrt{1-\frac{d}{tV_c}} \rightarrow r(t) = R\sqrt{1-\frac{v_T t - s}{tV_c}}. \quad \textbf{(2.4)}$$

One can fit all the measured radii at their known times t to the expression $r(t)$, and estimate the parameter V_c for any given experiment. Comparing the estimated and known V_c values (based on flow rates) provides a measure of the accuracy of the dual transducer technique.

2.3.2 Translation apparatus and transducer settings

The translation apparatus was constructed using two stepper-motors and controls (Microkinetics Corporation, Kennesaw, GA, USA) and is shown in Fig 2.3. The motors were controlled from a laptop computer through LabVIEW (National Instruments Corporation, Austin TX, USA) scripts and the DAQCard-700 (National Instruments). The scripts allowed control of both transducer separation and translation along the transducers' elevational direction. The transducer assembly was mounted upon a second stand that placed the transducers above the phantom being scanned.

A Toshiba Powervision 8000 scanner (Toshiba America Medical Systems, Tustin, CA, USA) with a 3.75 MHz (PVN-375AT) transducer in harmonic mode (power setting of P6 giving a MI=0.2 with a frame rate of 10 Hz) was used for contrast clearance. A GE Logiq 9 scanner (General Electric Healthcare, Milwaukee, WI, USA) with a 7L transducer in CPI (coded phase inversion) mode was used to image.

2.3.3 Tube phantom and contrast circulation

To build the tube phantom, a block of tissue-mimicking foam (S80 - Crest Foam Industries, Inc., Moonachie, NJ, USA) was saturated with water and frozen in order to temporarily harden the block sufficiently for drilling. A circular hole with a diameter of 6.4 mm was drilled through the block and the foam was subsequently allowed to thaw. Next, a thin-walled (0.79 mm) latex rubber tube with a 6.35 mm inner diameter (Kent Elastomer, Kent, OH, USA) was threaded through the block, with sufficient additional tubing (~20 times diameter) on both ends of the block to dampen transitional flow effects due to connections. The foam block was degassed prior to use by submersion in boiling water and subsequently allowed to cool, after which the phantom was maintained under water at all times.

The tube phantom was connected to form a recirculating flow system using intravenous (IV) tubing. A variable rate IV pump (IVAC 560, IVAC Corporation, San Diego, CA, USA) drove the flow. All flow originated and terminated at a stirred flask containing a contrast suspension (Definity Bristol-Myers Squibb Medical Imaging at a 1:5000 dilution in water). The suspension was continuously circulated through the phantom for the course of the experiment. A schematic of the overall setup is shown in Fig. 2.4. All scans were conducted within a water tank lined with sound absorbent rubber that had been allowed to come to gas saturation.

2.3.4 Measurement of effective transducer separation

Since the clearance transducer has a significant contrast disruption zone, the effective clearance width in the elevational direction of the clearance transducer was

measured by stopping the pump, applying a series of frames, and imaging laterally the contrast gap produced using the imaging transducer at low-power (1% acoustic output power setting giving a MI=0.06, focus at 10 mm). The width of the contrast gap (illustrated in Fig. 2.5) as the number of frames was increased without bound was recorded as 3 mm. The effective transducer separation was then computed by subtracting half of that width from the center-to-center distance.

2.3.5 Scans with dual transducer apparatus

The dual transducer system was used to image the tube phantom at two different flow rates (1.75 and 2.50 mm/s peak velocity) with effective transducer separations of 42, 57, 72, and 87 mm. The imaging transducer axial focus was changed to 20 mm in order to place it closer to the tube within the phantom. Cross-sectional images of the tube phantom were acquired and assembled. Images through the tube center in the lateral-elevational plane were then extracted from the reconstructed 3D imaging volume and scaled appropriately for the transducer translation velocity v_T (6 mm/s) and frame acquisition rate (19 Hz). Imaged contrast was subsequently compared to expected "time-dilated" parabolae. Observed and expected profiles were compared visually and quantified by fitting the observed profiles to their corresponding measures of center velocity v_c provided by eqn 2.4. Observed radii were estimated by a human reader by first enlarging the images, and then selecting locations where the pixel values substantially exceed the water-only background (using the MATLAB command *pixval*) and subsequently converting the number of pixels at each physical distance to a radius. The lateral-elevational plane was selected for comparison to avoid asymmetric effects of

overlying attenuation on the contrast profile. In addition, overlying attenuation due to contrast is eliminated at the profile edge, and a constant point-spread function is maintained throughout the plane.

2.4 Results

For a given cross-sectional plane imaged over time, one would expect a series of enlarging discs of contrast as depicted in Fig. 2.6, which shows a single plane extracted from three-dimensional data sets acquired using the dual transducer technique, with circles outlining the expected discs. Representative composite images of time-dilated parabolas assembled from the cross-sectional images with their expected contrast outlines superimposed are shown in Fig. 2.7 for each sweep, with the flow rate and effective transducer separation noted. Since the transducer translation velocity v_T (6 mm/s throughout) was greater than the maximum flow velocity v_c, the imaging transducer reached and overtook the refilling front for each sweep. At all times, the radius of the observed contrast should be that found by eqn 2.3. As expected, for the reduced flow rate shown in Fig. 2.7B, the contrast profile does not progress as far as that for an identical Δt (14.5 s). Examination of the images in Fig. 2.7 reveals a generally good match between the observed profiles and those predicted with the clear exception being the axial center of each profile. The center of the profile does not progress as far as the prediction, and the discrepancy is greater for higher flow rates. Fitting the measured radii to eqn 2.4 to estimate v_c gives estimated values shown in Fig. 2.8 for all scans acquired. The mean measured center velocities were (±std dev) 1.46±0.21 and 2.25±0.5 corresponding respectively to expected values of 1.75 and 2.50 (all in mm/s). In a statistical comparison

to the expected values, a Student t-test yields p=0.07 and 0.39; as such the measured velocities cannot be said to statistically differ from those expected although there may be a trend toward an underestimation.

The slight discrepancy between the expected and observed contrast profiles within the cylindrical tube phantom may be due to some minimal amount of contrast clearance from repeated low-power ultrasound exposure during the imaging process. Contrast clearance is more pronounced near the center of the tube than at the edges, due to the reduction in relative velocities between the flow and transducer. The reduction in relative velocity causes contrast near the tube center to receive more exposure, and hence preferentially clearing it relative to other contrast as modeled in Fig. 2.9. In addition, the reduction in overlying attenuation at the axial center also contributes to increased contrast clearance. In spite of the effects of slight contrast clearance, peak flow velocity was measured on average to within 13.2% of that expected.

2.5 Conclusions and discussion

This chapter has introduced the dual transducer technique, which is one approach for obtaining contrast agent clearance/refill data in a three-dimensional volume. The technique was applied to a perfused tube that provided a four-dimensional model that allowed for its verification by comparing expected and observed contrast profiles. Fitting observed profile radii to those predicted by eqn 2.4 gave center velocity measurements v_c measurements that tended to be less than those expected except for one case (Δt = 14.5 s, 0.040 mL/s flow rate), although the difference in all cases was not statistically significant ($p>0.05$). The v_c measurements may be low because of slight contrast clearance, which is

exhibited in two ways. Looking closely at Fig. 2.7, one notes first that the observed profiles were truncated at their center. Second, the edge of the contrast profile tended to fall on or within ($r \leq r_{expected}$) the theoretical edge. Radii measurements less than those expected would depress the fitted v_c value.

The exception to the depressed v_c measurements is notable in that the observed contrast profile as illustrated in Fig. 2.7 exceeds the theoretical curve ($r > r_{expected}$) in places, and that the profile is notably brighter than the others. The increase in brightness could be due to higher contrast agent concentration for this scan. This scan was the first in the series and the contrast concentration could have been greater than in the other scans due to contrast depletion through the course of the experiment. Without adjusting for this brightness increase, the observed edge for a given threshold would be farther from the center due to partial volume effects. This increase in the observed radii would then raise the fitted v_c.

Theoretically, radiation force effects could distort the flow of contrast agent through the flow phantom by pushing the contrast away from the tube center. However, radiation force effects were not evident in the observed profiles since the circular cross-sectional images of the contrast tended to remain centered in the tube throughout, as seen in Fig. 2.6.

This chapter has introduced the dual transducer technique and the apparatus that was used to implement it. The laminar tube flow phantom provided a four-dimensional flow with well-known characteristics, albeit one that is directional. In perfused tissues, the vasculature is much less directional, often having no clear direction of flow visible in the capillary bed. A perfused vascular bed, nevertheless, should be imageable in 3D with

this method using alternative measures of agent flow such as contrast mean transit time previously mentioned. Application of the technique toward a perfused vascular bed is the subject of the following chapter.

2.6 Appendix

The work described in this chapter was originally motivated by a desire to reduce required scan times in terms of acquiring volumetric refill images using one-dimensional arrays. Acquiring an image volume of substantial thickness with such an array using traditional methods (real-time refill [2-3] and interval imaging [4-7]) would require scan times that are excessive, an example which is given in Table 2.1. The scan times presented are calculated as follows:

ρ: slice density (slices/unit length)

T: volume thickness (length units)

N_s: number of slices, $N_s = \rho T$

N_t: number of time points

t_{clear}: contrast clearance time needed for one slice

t_{max}: maximum time point acquired on refill curve

v_T: transducer translation speed (distance/unit time), $v_T = N_t t_{trans}$ (see below)

t_{trans}: time to translate one slice thickness, $t_{trans} = 1/(\rho v_T)$, $t_{trans} \rightarrow 0$ for two dimensional arrays where translation is unnecessary to image the volume and imaging rates are controlled by propagation and other processing considerations.

t_M: time to reach time point M, $t_M \leq t_{max}$

t_r: time to return transducers to starting position

For real-time imaging with a one-dimensional array, the time required is

$$N_S\left[t_{clear} + t_{\max} + t_{trans}\right] \quad \textbf{(2.5)}$$

which is the number of slices N_s multiplied by the time required to acquire one slice (time to clear the plane plus the maximum time point in the refill curve), plus the time needed to translate the transducer one slice thickness. The number of time points acquired is limited only by the transducer frame rate and does not affect the acquisition time.

For interval imaging, the time required is

$$N_s\left[\sum_{M=1}^{N_t}\left(t_{clear} + t_M\right) + t_{trans}\right] \quad \textbf{(2.6)}$$

where $t_M \leq t_{max}$ and the sum is the total time required to obtain the image for all time points t_M. The required time can vary significantly depending on the selection of points t_M.

The time required for the scans using two transducers to demonstrate the dual beam technique is given by

$$\sum_{M=1}^{N_t}\left[N_s t_{trans} + t_M + t_r\right] - t_r \quad \textbf{(2.7)}$$

where the clearance transducer has traversed the volume in $N_s t_{trans}$ and the imaging transducer arrives at the volume boundary after time t_M. As N_s is moved into the summation, one can understand how a dramatic reduction in required scan time generally takes place compared to conventional real-time and interval acquisition. If imaging and clearance could be alternated between the two transducers, there is no need to return the transducers to their starting position after each sweep. Under such circumstances, t_r would be 0.

Note that the time required with the dual transducer technique does not depend on the number of slices acquired for a given v_T. That is, for a given v_T, an increase in the number of slices N_s would result in a corresponding decreases in the translation time between slices t_{trans}, and overall acquisition time would remain constant. The velocity v_T is generally constrained by the acoustic frame rate (AFR) and desired slice density ρ, i.e. $v_T \leq AFR/\rho$ rather than by the capabilities of the translation system. The minimum t_M that can be acquired is limited by translation velocity v_T and the minimum transducer separation. Clearance time t_{clear} is not present because the clearance transducer clears the volume as it is swept.

For a 2D array imaging a volume completely contained within its field of view, the scan time required is given by eqns 2.5 and 2.6 for real-time and interval imaging, respectively (with $N = 1$). The term $t_{trans} \rightarrow 0$ and the imaging rate is limited by the volumetric frame rate and beam propagation considerations. The minimum acquirable t_M is based on the time required to electronically sweep through and read the volume. The development of two-dimensional arrays has reduced the need for further scan time reductions; however, the dual transducer technique presented not only permitted the imaging of volumes in a reasonable time with 1D arrays, but also allowed one to investigate the effect of contrast clearance pattern differences on observed refill curves.

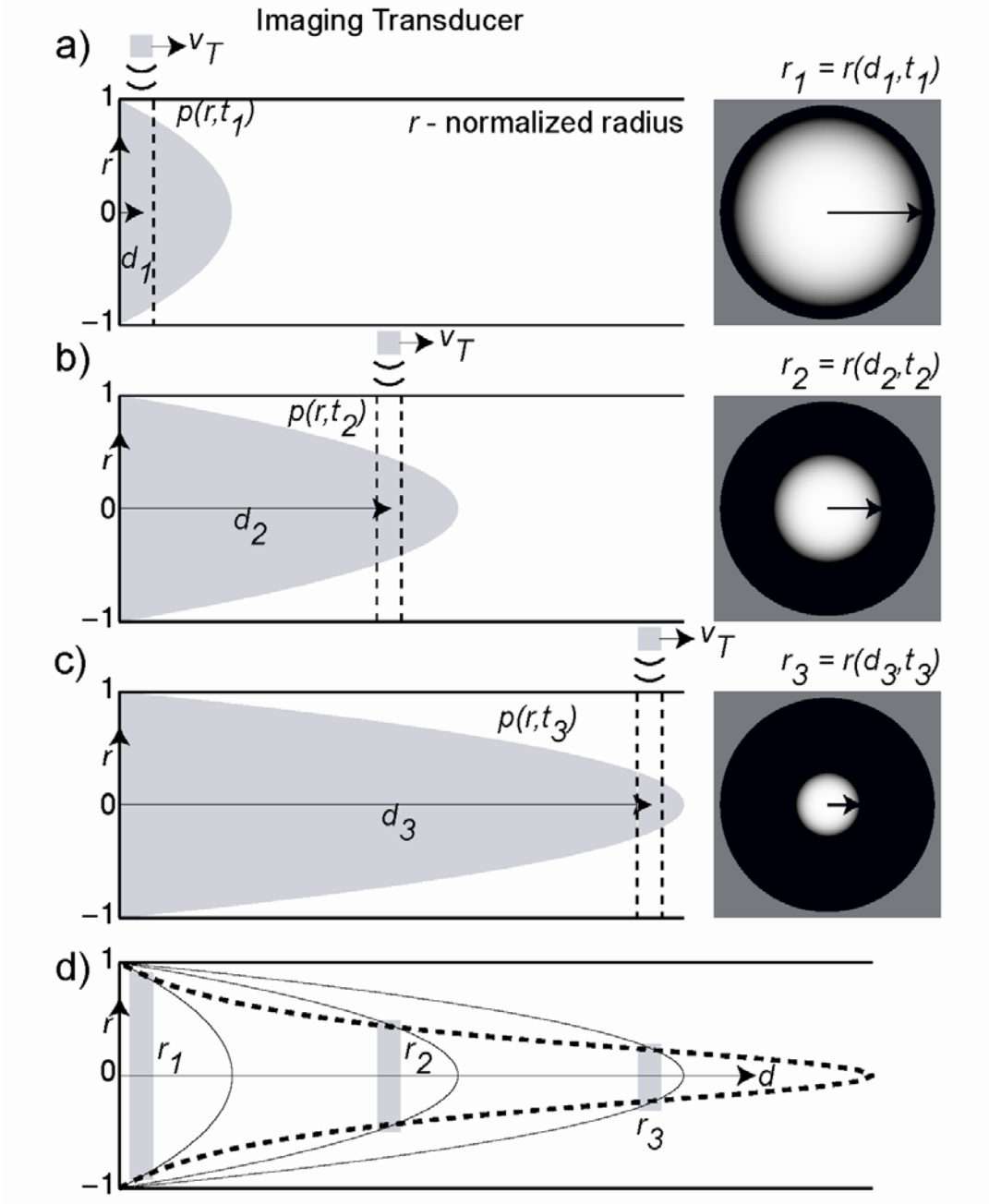

Fig. 2.1. Dual transducer tube flow dynamics. a) At a given time t_1, contrast refilling the tube cleared previously by the clearance transducer forms a parabolic profile. The imaging transducer images a slice of the profile in cross-section at position d_1. Within that cross-section, the refilled contrast has a radius r_1. b and c) The contrast profile remains parabolic as the tube refills. At times t_2 and t_3, the cross-sections are imaged at positions d_2 and d_3 respectively. Even though the contrast profile at any instant in time t is parabolic, the measured radii r are taken of contrast profiles at *different* times. d) If the transducer translation velocity v_T were much larger than the flow velocity, the contrast profiles at each time would not substantially evolve, and r would solely be a function of the position d and the initial delay time between contrast clearance and profile imaging. However, there is a simple relationship for $r(d,t)$ (derived in the text) when the contrast profiles evolve significantly, given by $r(d,t)=R\sqrt{(1-d/tV_c)}$, where R and V_c are respectively the tube radius and center flow velocity. Assembling the measured radii from an evolving contrast profile produces a predictable "time-dilated" parabola (shown by the dashed line).

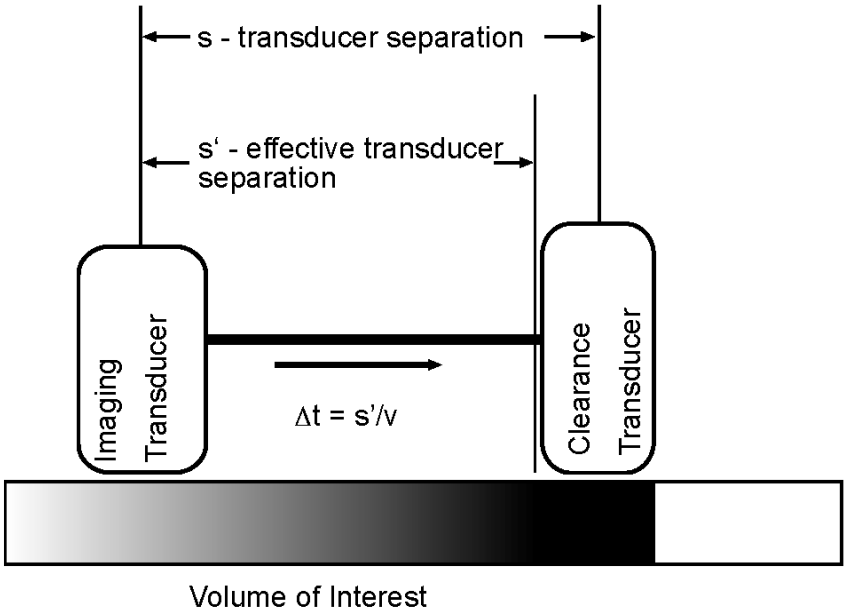

Fig. 2.2. Dual transducer method schematic. Each transducer is assigned a separate task, with the clearance transducer translated over the tissue ahead of the imaging one. The clearance transducer is operated at sufficient power and pulse repetition frequency (PRF) to clear the volume of interest of contrast agent during each sweep. The imaging transducer is operated in a minimally destructive mode, and it reads the amount of contrast agent that has refilled since contrast clearance. Both transducers are swept through the volume of interest at constant velocity *v*. Based on the separation distance *s*, the refill associated with a specific interval Δt can be measured. Due to significant clearance zone thickness, *s'* is less than *s* the transducer center-to-center distance. Additional delay can be added by pausing the sweep after clearance and before imaging.

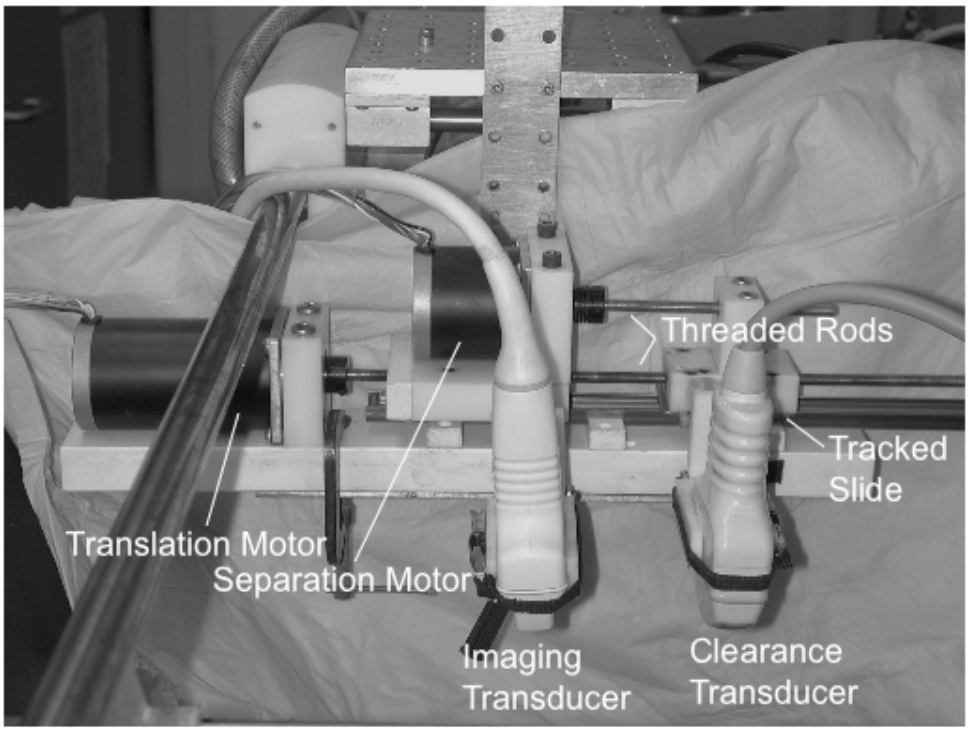

Fig. 2.3. Photograph of the constructed dual-transducer apparatus. Two stepper motors turn two threaded rods parallel to each other to move the ultrasound transducers, which are held by the transducer holders shown. Transducer holders translate on a guided slide (400L - THK Corporation Japan). The separation motor, mounted upon a stand, adjusts transducer separation. The stand in turn is translated by the larger translation motor, which controls the sweeps over the volume of interest. Imaging and clearance transducers are mounted as shown. The complete apparatus was placed above a rubber-lined water tank upon a stand, and cables connect the motors to a control box (not shown), which provided drive power and was in turn controlled by a laptop computer using the DAQCard-700 and LabVIEW scripts.

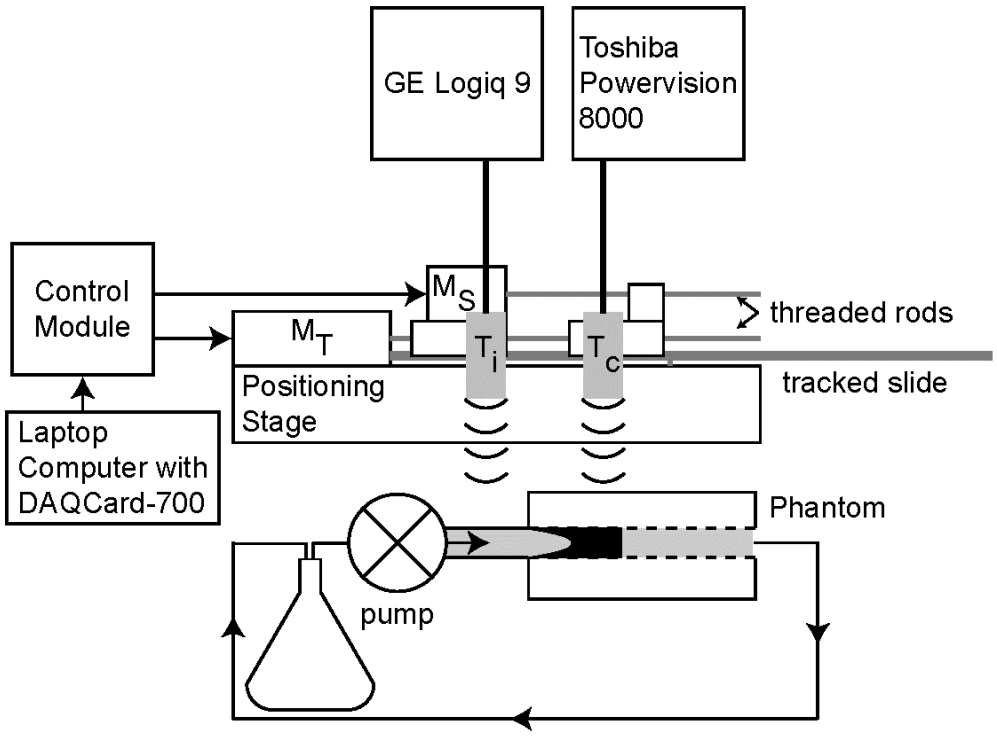

Fig. 2.4. Schematic of dual-transducer apparatus and experimental setup. The dual-transducer apparatus consists of a dual-transducer positioning stage, which consists of translation (M_T) and separation (M_S) motors. Each motor turns a threaded rod, which translates a platform that contains a transducer holder. The platforms translate within the tracked slide. Motors are connected to a powered control module, which contain the electronics driving the motors. The control module is linked to a laptop computer through the DAQCard-700. Using LabVIEW scripts, transducers are translated as required. The transducers are positioned above the phantom being scanned, with the clearance transducer (T_c) positioned at the edge of the volume of interest. The phantom is continuously perfused with dilute (1:5000 concentration) contrast pumped from a stirred flask.

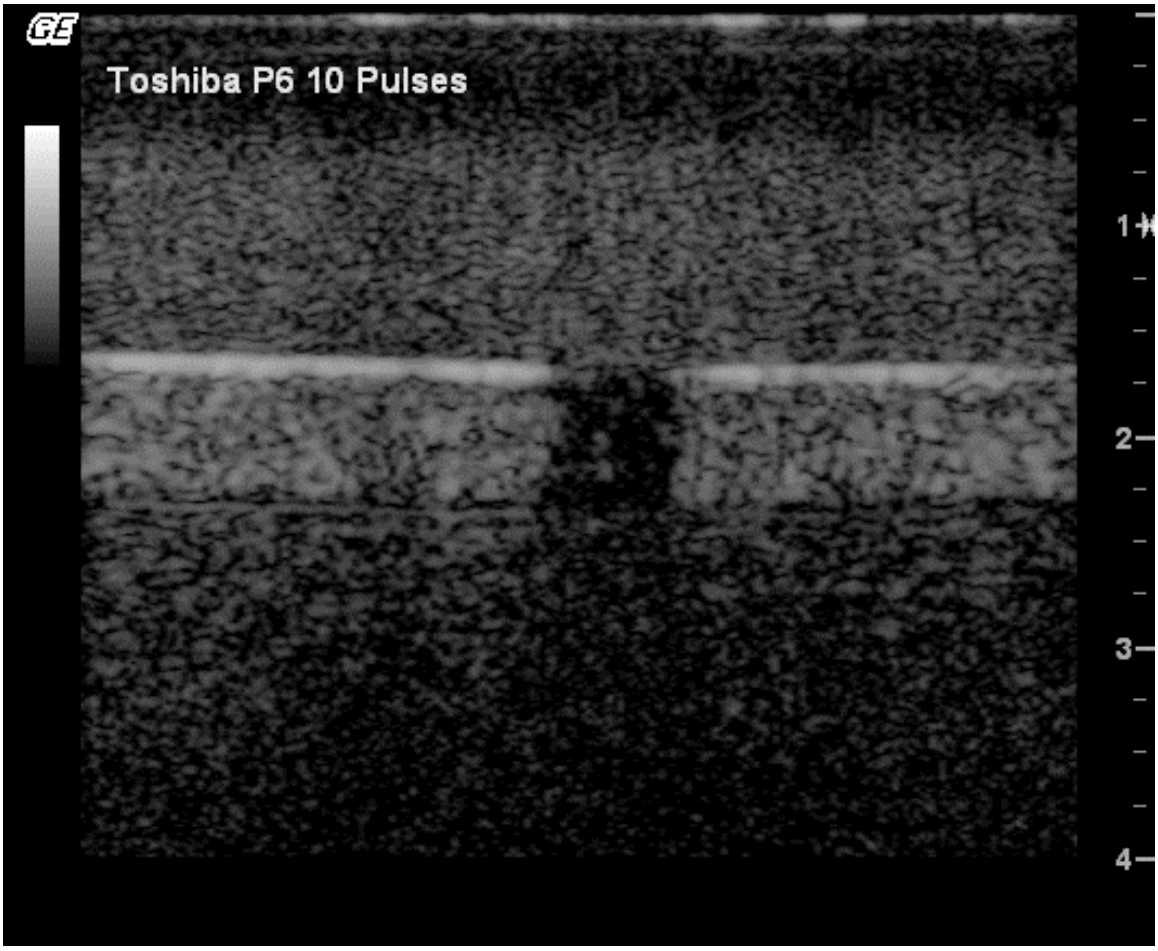

Fig. 2.5. Image of contrast clearance zone thickness. This image, obtained from the imaging transducer at low power shows the 6 mm gap in stationary contrast generated by the clearance transducer after a series of 10 pulses (settings described in the text). The size of the gap asymptotically approaches this value with clearance transducer pulses. As such, the effective transducer separation was considered half of the gap (3 mm) less than the physical transducer separation.

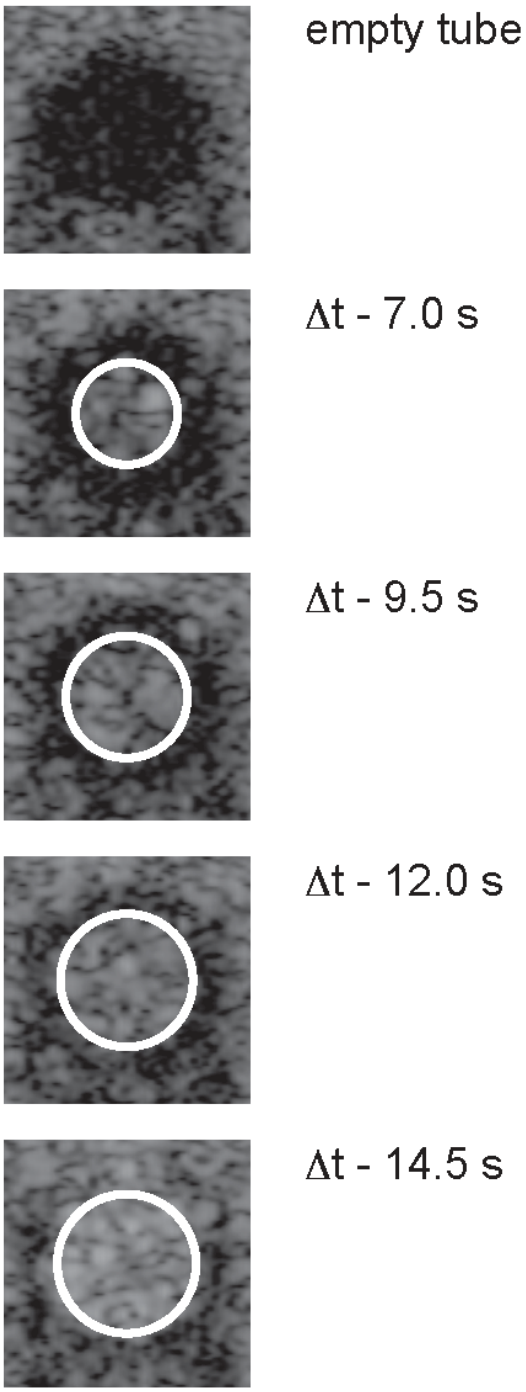

Fig. 2.6. Sample planar images of tube flow. For the 0.040 mL/s flow rate, these images are a sample of those directly obtained in the transducer axial-lateral plane of the flow at a distance *d* of 16 mm for differing values of *Δt*. The circles of contrast have observed diameters respectively of 3.36, 4.47, 5.53, and 5.97 mm corresponding to theoretical values (outlined) of 3.67, 4.36, 4.76, and 5.02 mm with increases in *Δt*.

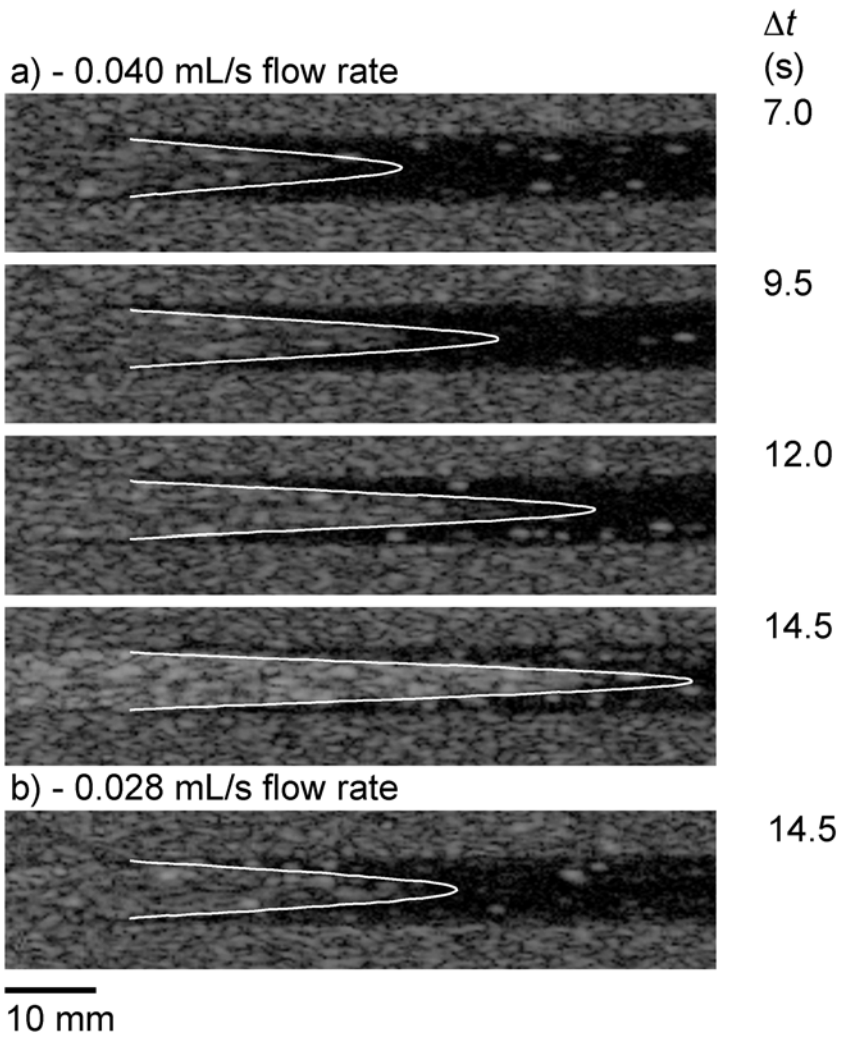

Fig. 2.7. Reconstructed images along the length of the flow tube showing the contrast agent flow. These are corrected for the time-dilation effect described in the text and Fig. 2.1. The white line shows the theoretical position of the contrast front. The flow passed through a tube of radius 3.175 mm at a rate of a) 0.040 mL/s and b) 0.028 mL/s. Transducer translation velocity v_T was 6 mm/s. Expected profiles closely match those observed, except at the center of the leading edge. It is believed that the discrepancy is due to slight contrast destruction due to both increased beam exposure and decreased overlying attenuation from overlying contrast (see text).

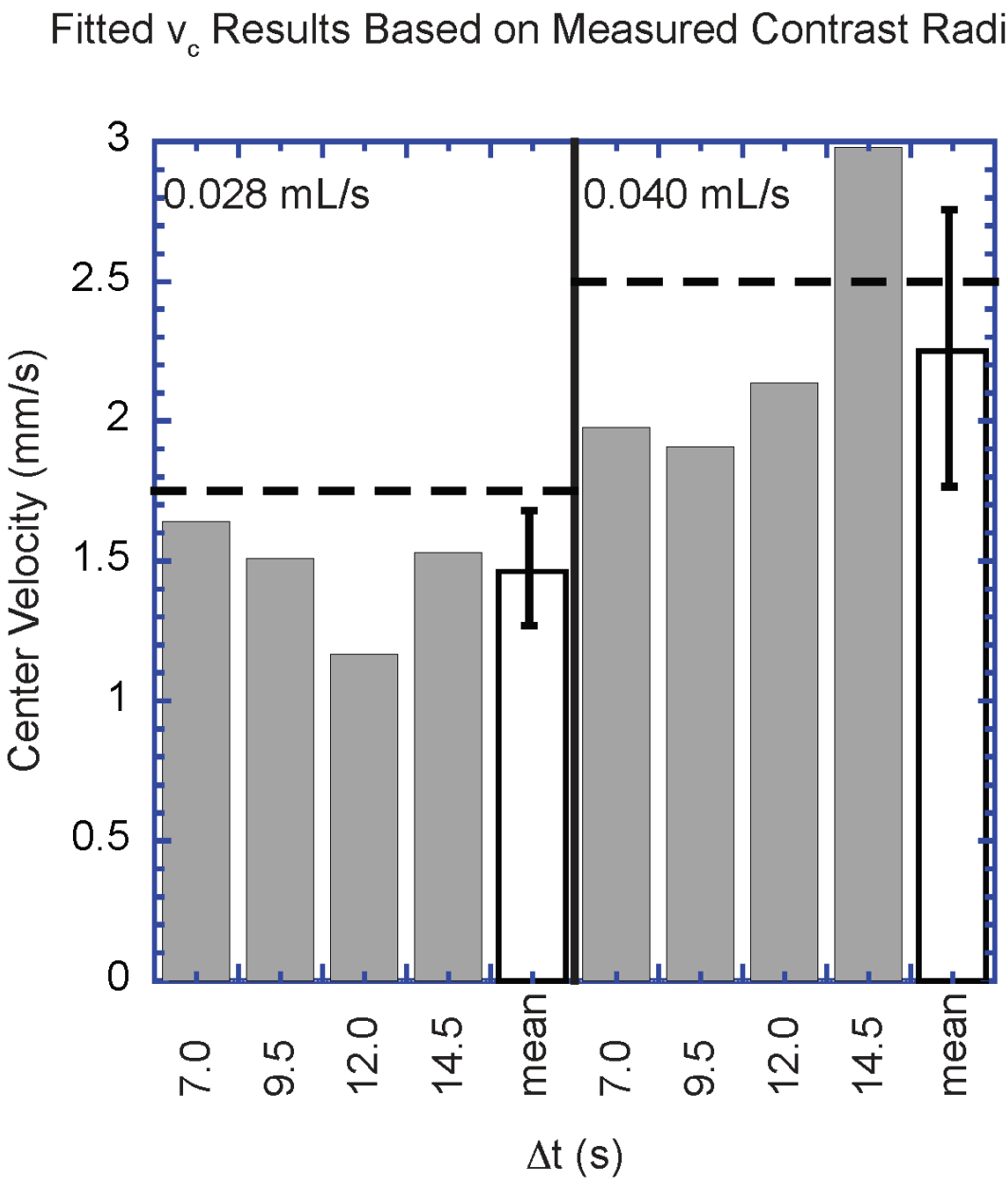

Fig. 2.8. Fitted v_c results for cylindrical tube phantom. Dual transducer scans were acquired for the cylindrical tube phantom with two center flow velocities (1.75 and 2.50 mm/s - corresponding to the flow rates of 0.028 and 0.040 mL/s respectively from Fig. 2.7) using four different refill times. Shown are the measured values of v_c (1.46 and 2.25 mm/s) obtained by fitting measured contrast radii to the expression given in eqn 2.4 for all measurements along with the mean and standard deviation for the measurements grouped by flow rate. Dashed lines denote theoretically known values of v_c. The measurements tended to be less than those expected except for one case (Δt = 14.5 s, 0.040 mL/s flow rate), although the difference in all cases was not statistically significant ($p>0.05$).

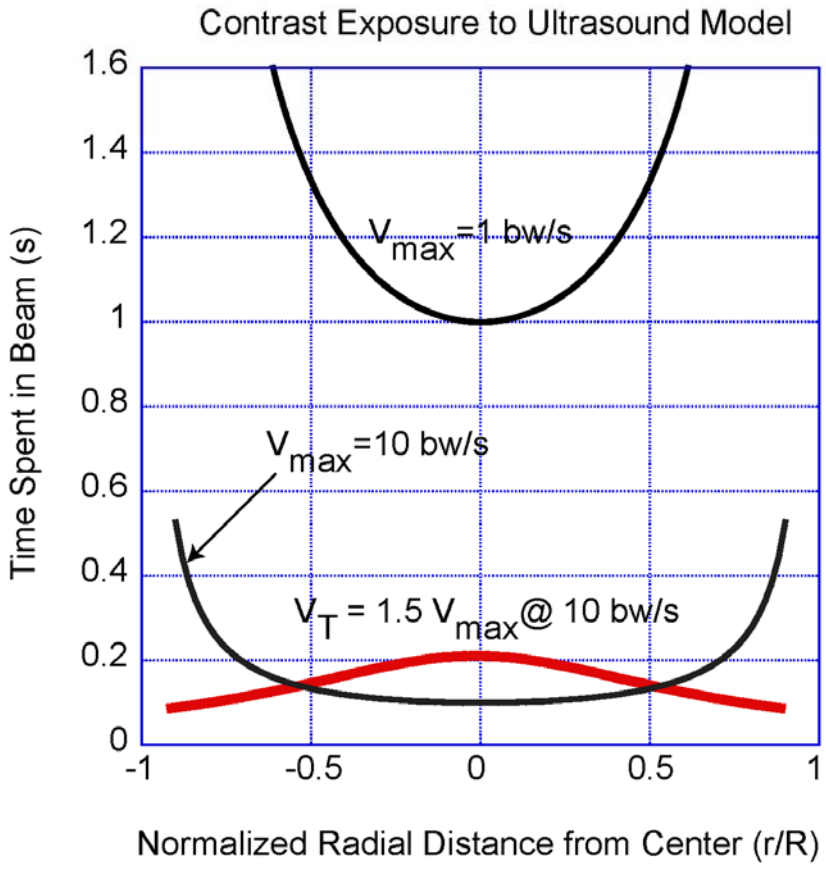

Fig. 2.9. Simplified model of time spent in the ultrasound beam for various flow speeds. Flow speeds are represented in "beam-widths" per second (bw/s) for normalization. Flow velocity V is considered parabolic, with a profile given by $V(r) = V_{max}[1-(r/R)^2]$, where r is the tube radius and V_{max} the maximum velocity. With a stationary transducer, the fluid closest to the tube wall is exposed to the beam for the longest period of time, and these exposure durations decrease with increased flow velocity as shown by the three curves representing V_{max} at 1 and 10 bw/s. The thicker shaded curve represents what happens as the transducer is translated along the axis of the tube at a speed higher than the maximum flow velocity. In this case, where V_{max} was set to 10 bw/s and the transducer speed V_T was set to 1.5 times V_{max}, the maximum exposure to the beam occurs at the center of the tube. This may help explain the center peak cut-off of the flow profiles shown in Fig. 2.7. That is, the contrast may be exposed to sufficient pulses in the center to break the bubbles at higher flow velocities. This effect is compounded by the fact that there is also less overlying attenuation due to the profile shape.

Slice Separation (mm)	Number of Time Points (Interval and Dual Transducer Imaging)	Interval Imaging	Dual-Transducer Technique	Real-Time Refill
0.5	3	80 min	1 min 53 s	40 min
1	3	40 min	1 min 53 s	20 min
2	3	20 min	1 min 53 s	10 min
1	5	67 min	3 min 20 s	20 min

Table 2.1. Comparison of required total time for interval imaging, real-time refill, and the dual transducer technique. Constant parameters used to compute the times are a transducer translational velocity v_T of 6 mm/s, a transducer separation of 60 mm, and a volume of interest thickness of 40 mm. Chosen timepoints for interval imaging and the dual-transducer technique are (in s) 10, 20, 30 for 3 time points, with the additional points 15 and 25 for 5 time points. Real-time refill imaging acquires all time points continuously up to the maximum time point. Transducer translation time is negligible for real-time refill and interval imaging (~6.5 s) and is covered in the rounded times. For the dual-transducer case, the transducer pair is moved back to the starting position after the acquisition of each timepoint, except for the final one. Time required to clear contrast is negligible (< 2 s) for both interval imaging and real-time refill acquisition. Note that using the dual-transducer method causes a dramatic reduction in the time required to image a three-dimensional volume. Since the dual-transducer technique's time requirement is independent of the slice thickness, image slices could be acquired as closely together as necessary without requiring additional time, subject only to the imaging transducer frame rate, unlike traditional techniques.

2.7 References

[1] Chen NG, Fowlkes JB, Carson PL, LeCarpentier GL. Rapid 3D Imaging of Contrast Flow: Demonstration of a Dual Beam Technique. Ultrasound Med Biol 2007; 33(6) 915-923.

[2] Porter TR, Li S, Jiang L, Grayburn P, Deligonul U. Real time visualization of myocardial perfusion and wall thickening in humans with intravenous ultrasound contrast and accelerated intermittent harmonic imaging. J Am Soc Echocardiogr 1999; 12: 266-271.

[3] Simpson DH, Chin CT, Burns PN. Pulse Inversion Doppler: A New Method for Detecting Nonlinear Echoes from Microbubble Contrast Agents. IEEE Ultrason Ferroelectr Freq Control 1999; 46(2): 372-382.

[4] Kamiyama N, Moriyasu F, Kono Y, et al. Investigation of the “flash echo” signal associated with a US contrast agent. Radiology Suppl. S 1996; 201: 165.

[5] Kamiyama N, Moriyasu F, Mine Y, Goto Y. Analysis of flash echo from contrast agent for designing optimal ultrasound diagnostic systems. Ultrasound Med Biol 1999; 25(3): 411-420.

[6] Ohmori K, Cotter B, Kwan OL, Mizushige K, DeMaria A. Relation of contrast echo intensity and flow velocity to the amplification of contrast opacification produced by intermittent ultrasound transmission. Am Heart J 1997; 134: 1066-1074.

[7] Wei K, Jayaweera AR, Firoozan S, et al. Quantification of Myocardial Blood Flow With Ultrasound-Induced Destruction of Microbubbles Administered as a Constant Venous Infusion. Circulation 1998; 97(5): 473-483.

Chapter 3

Application of dual-transducer apparatus to a perfused vascular bed

3.1 Chapter overview

This chapter describes the results of scanning a perfused vascular bed with the dual transducer apparatus previously described in chapter 2. A preserved porcine kidney prepared as described in [1] was perfused at two different flow rates through the renal artery, and scanned using the dual transducer apparatus. A location near the middle of the clearance zone was also imaged using a modified interval imaging technique for comparison. Due to the degradation of contrast agent through the course of the *in vitro* experiment, a vessel model was developed to compensate for the degradation. In addition, the model permitted the fractional moving blood volume (FBV) to be estimated. Refill curves were estimated from both the interval imaging data as well as from the dual transducer scans. The dual transducer scans had perfusion values that were 1.06 ± 0.04 times those obtained using the interval imaging. Combining the vessel model with the refill curves allowed absolute perfusion to be estimated, and a consistent comparison was made to kidney cortex measurements found in the literature [2]. The

consistency in the perfusion measurements made using interval imaging and the dual transducer scans, with the large difference in contrast clearance patterns, suggest that ultrasound contrast perfusion measurements are independent of contrast clearance pattern. As such, one would expect volumetric contrast perfusion measurements, whether obtained using a 2D array or otherwise, to be similar to each other. The work described in this chapter is adapted from a paper that is in press and will appear in *Ultrasound in Medicine and Biology* [3].

3.2 Review of blood flow quantification

In a perfused vascular bed, contrast agent fills the blood vessels, and it is assumed that the agent follows the fluid flow perfusing the bed. After the cessation of the contrast clearance pulses, contrast agent from outside the disruption zone refills the cleared volume. The refill can be measured either continuously with low-power pulses (real-time refill imaging) [4] or intermittently [5-6] at only specified times (interval imaging). The contrast signal intensity (assumed proportional to the contrast concentration) [7] at the measured time points can then be fitted to an exponential equation of the form $y(t) = A[1-exp(-t/MTT)]$ after subtraction of the tissue baseline, where A is the signal intensity at the asymptotic limit, t the time interval, and MTT the mean transit time [8]. Other models have been previously described such as the error function fit [9-10], which systematically accounts for the elevational beam shape, and the sigmoidal function model [11]. The estimated refill curves presented are derived from the exponential model in order to facilitate comparison with other studies.

Perfusion is the amount of fluid (typically blood) that passes through a tissue per unit time per unit volume. From a refill curve described with the exponential equation above, the value *A/MTT* is indicative of perfusion (reviewed in [12]). Values of *A* are proportional to the moving fractional blood volume; and *MTT* is inversely proportional to the rate at which the fluid passes through. If one can properly normalize *A* as a fraction of the value that corresponds to the circulating fluid itself, $A_{100\%}$, one would be able to estimate the absolute perfusion. Incidentally, the initial slope of the exponential expression is *A/MTT,* and hence the successful estimation of it would allow perfusion estimation. As illustrated by the acquired data, measured points on the refill curve contain substantial noise and this noise is reflected in the level of precision of the perfusion estimates. The initial upslope has previously been used [13] to estimate renal perfusion in canines.

3.3 Experimental methods

3.3.1 Modification of dual transducer apparatus

The dual transducer apparatus described in chapter 2 was modified by the addition of circuitry that allowed the controlled triggering of image acquisition through the footswitch. This circuitry was used, through a LabVIEW script (National Instruments Corporation, Austin, TX, USA) that opened and closed a solid-state relay (PVN 012-ND International Rectified, El Segundo, CA, USA) in order to trigger image acquisition. The additional control over triggering image acquisition was used to control image spacing in the elevational direction when performing dual transducer scans as well as to perform interval imaging.

3.3.2 Low-power interval imaging

A modified interval imaging technique was developed that allows the acquisition of interval imaging data at the minimally destructive acoustic power that was used for the dual transducer scans. As illustrated in Fig. 3.1, the insertion of a single low-power frame immediately before the contrast clearance sequences provides a series of low-power images corresponding to the same flow being monitored by the traditional high power interval imaging sequence. By obtaining interval imaging images at the same power as the dual transducer scans, any possible differences in measured perfusion would be due to the differences in contrast clearance patterns.

3.3.3 Image acquisition

The previously preserved porcine kidney was rehydrated and degassed by perfusion through the renal artery with (> 5 L) degassed water. The kidney was then perfused with a 1:5000 suspension of Definity (Lantheus Medical Imaging Inc., North Billerica, MA, USA) at 17 mL/min and 33 mL/min (referred to here as the slow and fast rates, respectively) using a peristaltic pump (Cole-Parmer L/S pump and drive, Cole-Parmer Instrument Corporation, Barring, IL, USA). Contrast agent was not recirculated as with the tube phantom; rather, agent was pumped through the kidney in a single pass.

Ultrasound scans were conducted within a tank lined with 13 mm thick sound absorbent ultra-soft polyurethane (Sorbothane Inc., Kent, OH, USA) and filled with water that had been allowed to come to gas saturation. A schematic of the overall experimental

setup is shown in Fig. 3.2. Each motor turns a threaded rod to translate a platform with an attached transducer holder. Motors are connected to a control module (Microkinetics Corporation, Kennesaw GA, USA) containing the electronics driving the motors. The control module contains circuitry needed to operate the footswitch trigger and is linked to the footswitch control of the GE Logiq 9 (General Electric Corporation, Milwaukee, WI, USA) in order to trigger image acquisition from the imaging transducer. The DAQCard-700 (National Instruments Corporation, Austin, TX, USA) linked the module to a laptop computer that controlled transducer motion and triggering through a LabVIEW (National Instruments) script. The kidney phantom was mounted beneath the water on a stand and secured with two elastic bands. The transducer assembly was mounted above the kidney being scanned.

Dual transducer scans in the transverse orientation as shown in Fig. 3.3 were made with the Toshiba Powervision (Toshiba America Medical Systems, Tustin, CA, USA) system using the PVN-375AT transducer for contrast clearance. A constant power output and firing rate were maintained by placing the Toshiba system transducer in harmonic mode (power setting of P16 (MI=1.0) at a frame rate of 127 Hz and a center frequency of 2.3 MHz). The GE Logiq 9 (General Electric Corporation, Milwaukee, WI, USA) in pulse inversion (PI) mode was used at low power (1% acoustic output-AO MI=0.05) with the 7L transducer to image at a receive center frequency of 7.0 MHz.

Images for a 42 mm thick volume were acquired for refill times of 8, 10, 15, 20, 25, 30, 40, 60, 70, 120, and 150 s with a 1 mm slice separation using the dual transducer apparatus with the transducers separated with a center-to-center distance of 45 mm (n=4 for each flow rate, with the exception of the 150 s point for 2 acquisitions at the fast flow

rate due to technical difficulties). The scans encompassed a total phantom volume of 100-cm^3, with each image slice being approximately 4.7 cm in the lateral direction and 5 cm in the axial direction. A LabVIEW script (National Instruments Corporation, Austin, TX, USA) was used to both control transducer translation and slice separation via the DAQCard-700. The transducers were translated at a speed of 6 mm/s, which was the maximum translation speed attainable with the apparatus. The 1 mm slice separation was obtained by triggering a solid-state relay (PVN 012-ND International Rectifier, El Segundo, CA, USA) linked to the GE Logiq 9 footswitch control at 6 Hz. The acoustic output of the clearance transducer was manually stopped at the start of image acquisition in order to eliminate transducer cross-talk.

Refill data using low power interval imaging (n=5 for both flow rates) were collected using the GE L9 at a transverse slice position (20 mm from the start of the acquired volume) with the same orientation for comparison to dual transducer results. The 20 mm position was near the center of the cleared volume; therefore, any differences in measured perfusion arising from differences in contrast clearance zone thickness would be more pronounced than in cases where the position was further from the center. The refill times acquired using interval imaging were also the same as those acquired with the dual transducer technique, except for the substitution of 5 s in place of 8 s and the lack of a 10 s point for one fast flow acquisition due to technical difficulties. Using the footswitch trigger, twenty-five clearance pulses at 5 Hz were fired at high power (100% AO MI=0.4) and low-power interval imaging frames were acquired by observing contrast signal for different intervals at 1% AO immediately prior to contrast clearance. All acquired images were decompressed to a linear echo power scale prior to analysis.

Due to variations in the contrast agent during the course of the acquisitions (details in appendix A), interval imaging subtraction images were computed at each time point by subtracting the low power baseline tissue image acquired at the end of the contrast clearance sequence from the corresponding refill image, and recompressing to a log power scale. Dual transducer subtraction images were computed similarly by subtracting the mean baseline tissue image (average of all the interval imaging baseline images) from the raw images, and again recompressing.

3.3.4 Contrast variation and normalization-reference artery contrast model

Variations in concentration of the infused contrast agent suspension alter the signal intensity observed during the course of refill. These variations include both differences in initial concentration, as well as decay over the course of acquisition. Agent variation within a refill curve acquisition distorts the curve, and if ignored would yield erroneous flow parameters. Properly normalizing the signals obtained from the cortex to the input contrast agent would correct for contrast agent variation. In addition, such normalization would allow estimation of the FBV and perfusion (perfusion being r = FBV/MTT). The input contrast agent can be monitored through any relatively large blood vessel with a high flow rate. Due to its large size and high flow velocity, one can assume that the renal artery is always filled with contrast whenever the kidney is being perfused regardless of the refill state of the remainder of the kidney. Therefore, the renal artery was used as a reference vessel to normalize measured cortex signals to account for contrast variability. *In vivo*, contrast decay is not expected to play a significant role due to

the short (< 30 s) contrast transit times; however, the normalization process is still required in order to estimate absolute perfusion and FBV.

The normalization process must account for the following factors: (1) overlying attenuation, (2) reference vessel size, and (3) reference vessel position. First, any difference in overlying attenuation between the renal artery and cortex region of interest (ROI) would distort the signal intensity of one relative to the other. Both the renal artery and cortex ROI, denoted in Fig. 3.4, however, have negligible overlying attenuation; therefore overlying attenuation does not play a significant role for this specific study. Second, the signal intensity within the reference vessel can be applied to a model described below to estimate the intensity A of 100% contrast suspension at the vessel depth. The model accounts for effects arising from vessel size. Third, since the reference vessel is located at a different depth than that of the kidney cortex, A needs to be scaled in order to account for signal intensity changes from differences in beam geometry and imaging system parameters.

To account for reference vessel size, the reference artery was modeled as an in-plane cylindrical tube with a fixed radius a and angle θ as indicated in Fig. 3.5 which shows both its side view and its elliptical cross-section. The transducer point-spread function is assumed constant throughout the vessel. Since attenuation at any point (x, y) within the tube is due solely to overlying material with thickness d, the signal F for (x, y) is given by the following (A being the unattenuated signal intensity level):

$$F(x,y) = A\left(10^{-0.1(\alpha_f+\alpha_h)d}\right) = A\left(10^{-0.1\alpha\left(b\sqrt{1-\frac{x^2}{a^2}}-y\right)}\right). \qquad \textbf{(3.1)}$$

In eqn 3.1, b is the length of the semi-major axis, α_f and α_h the attenuation (dB/unit length) respectively at the fundamental frequency and harmonic frequencies. The addition of α_f and α_h produces an effective attenuation coefficient α that is observed through the course of this study. The expression of the thickness d as a function of the geometric parameters a, b, x, and y is presented in appendix B. For an idealized beam with constant elevational thickness K, the expected signal at each depth y is

$$P(y) = \int_{-K/2}^{K/2} F(x,y)dx \qquad \textbf{(3.2)}$$

The axial and elevational beam widths can be modeled as Gaussian curves with total area 1 [14]. The computation of $P(y)$ is illustrated in Fig. 3.6. The mean observed profile through the vessel is the convolution of the axial Gaussian function B_{axial} with the integral of the product of the ideal $F(x,y)$ and the elevational Gaussian function $B_{elevational}$. Therefore, the observed profile $P(y)$ through the vessel is

$$P(y) = B_{axial} * \int_{-\infty}^{\infty} [F(x,y)](B_{elevational})dx = B_{axial} * \int_{-\infty}^{\infty} A\left(10^{-0.1\alpha\left(b\sqrt{1-\frac{x^2}{a^2}}-y\right)}\right)(B_{elevational})dx \qquad \textbf{(3.3)}$$

with convolution denoted by $*$. Given an observed profile P, one can fit the profile to parameters A, α, a, B_{axial}, and $B_{elevational}$ with the latter three assumed constant throughout.

Finally, to account for reference vessel position, the value A is then scaled to the value A_{scaled} that it would have been were the vessel located at the axial location of the cortex by a factor S (i.e. $A_{scaled}=SA$). The factor S accounts for changes in signal intensity due to focal gain differences and the differences in time-gain compensation at the two differing axial locations.

Therefore, corrections are finally made to signal intensity measurements to account for variations in contrast signal by normalizing all measurements to A_{scaled}. This normalization estimates the FBV of the cortex. From the FBV of the cortex and the contrast MTT, perfusion is estimated as the value of r = FBV/MTT.

3.3.5 Application of reference artery contrast model

The renal artery was used as the reference vessel for all measurements. The model was first used to obtain estimates of both the renal artery size (a) and transducer beam widths B_{axial} and $B_{elevational}$, which remained constant throughout the experiment. Second, the model was used to obtain the signal intensity of 100% dilute contrast A at the vessel depth for every acquired image along with the attenuation coefficient α due to the contrast agent within the artery.

The renal artery size, a, and the beam width parameters, B_{axial} and $B_{elevational}$, were estimated as follows. First, the interval imaging frames were selected for analysis because of the lack of transducer motion during their acquisition and therefore reduced noise from vessel motion. Vessel profiles $P(y)$ were computed and averaged in the θ direction (as denoted in Fig. 3.6) over a limited depth range in order to reduce noise. Using a least-squares criterion, each profile was fitted to eqn 3.3 for all five parameters (A, α, a, B_{axial}, and $B_{elevational}$). For each refill time and flow rate (n=5), fits containing outliers in any parameter were rejected using Dixon's criterion [15]. The remaining fits were used to calculate the mean and standard deviation of the beam width parameters B_{axial}, and $B_{elevational}$, as well as the vessel size a.

The values of A and α were then estimated by fixing the constant parameters a, B_{axial}, and $B_{elevational}$ as calculated above in eqn 3.3, and subsequently refitting the same observed profiles. Since the constant parameters physically have only one value, fixing them at their estimates places the emphasis on the relationship between the remaining parameters A and α. Values of A and α were recorded for every refill time, flow rate, and acquisition. The correlation coefficient of A and α was calculated.

For the dual transducer acquisitions, estimates of A and α were made by following the same procedure described above with a, B_{axial}, and $B_{elevational}$ fixed at their previously determined values. Profiles with fitted values of $\alpha<0$, indicative of a distorted fit, were refit using a least absolute residuals criterion in order to reduce noise effects. Since the time required to pass the transducers over the volume was short compared to expected changes due to the contrast input, each value of A was assumed to apply throughout the acquired volume.

The scaling factor S was estimated by obtaining images from a Model 44 Ultrasound Resolution Phantom (Computerized Imaging Reference Systems Inc., Norfolk, VA, USA) at standoff distances equal to that of the kidney cortex and renal artery minus a constant thickness of overlying material. The ratio of the signal intensities S for the two cases was used to correct for the renal artery being located at a different axial depth than the cortex ROI. Using this ratio, values of A_{scaled} were computed from estimated values of A.

3.3.6 Refill curve estimation

Measurements of the kidney cortex after degassing but before introduction of contrast agent indicated that the tissue baseline signal intensity level was essentially constant throughout the cortex at each flow rate. These tissue baseline intensities were subtracted from the mean signal intensities from the cortex ROI at each refill time point and then normalized to values of A_{scaled}. These normalized mean signal intensities were then plotted as a function of refill time for each flow rate and imaging method. Each measured point y_{tj} on the refill curve was assumed normally distributed with an underlying value μ_{tj} (subscripts refer to time t of the jth acquisition). The values of μ_{tj} were then assumed to follow the exponential expression $FBV_j[1-exp(-t/MTT)]$, where FBV_j is a random normal variable with mean FBV. Values of FBV_j may vary from run to run due to contrast agent variation between runs. Modeling the refill in this manner accounts for any correlation between time points within a given acquisition. All measured y_{tj} values were then fit using SAS 9.1.3 (SAS Institute, Inc., Cary, NC, USA) with these assumptions. Estimates of the underlying FBV and MTT were determined along with their standard errors. Due to the relatively long MTTs, some of the measured refill curves may not have achieved saturation and thus fit poorly to an exponential. For these cases, indicated by an estimated correlation coefficient between FBV and MTT of 1, a line of the form $m_j t$ were fit to the data instead. The linear fit was used in these cases to estimate perfusion without knowledge of either FBV or MTT. Fits were performed on a series of transversely oriented image slices from the dual transducer acquisitions for positions of 10, 15, 20, 25, 30, 35, and 40 mm (all measured from the first acquired frame of the volume) with the ROI kept at the same axial and lateral position. The same fitting process

was used on the low power interval imaging images acquired at the 20 mm position for comparison.

In addition to the selected transverse slices, a plane oriented in the longitudinal direction was selected from the dual transducer acquired volumes for analysis. Images were reconstructed for a selected axial-elevational plane. Refill curves for an ROI in the kidney cortex with the same size as the transverse ROI were estimated using the model described above. This ROI was at the same axial distance as the transverse case ROI. Estimated parameters were compared with those of the cortex obtained in the transverse direction.

3.4 Results

3.4.1 Resulting images

Representative subtraction images in Fig. 3.7 show the 20 mm transverse slice imaged using low-power interval imaging compared with corresponding dual transducer images. The images show the kidney refilling with time, as expected for corresponding delay times. The fast flow images at any given time are brighter than the slow flow images due to the increased flow rate. Brightness variations between the acquisitions are probably due to differences in contrast concentration. Representative images of the reconstructed images, available as a result of the dual transducer volumetric acquisitions and not otherwise obtainable, of the kidney in the longitudinal direction are shown in Fig. 3.8. The change in contrast levels from the reconstructed images is less apparent than the change from the transverse cases because the reconstructed images are not subtraction images. In addition, the images are of lower quality than those oriented transversely due

to the elevational point-spread function of the imaging transducer being wider than the lateral point-spread function. Finally, slice separation effects are present. The 1 mm slice spacing was selected due to speed limitations of the translation apparatus (v≤6 mm/s) and maximum trigger rate (~6 Hz) of the imaging system (therefore in order to obtain slice spacings <1 mm, the translation apparatus would have to be slowed, making the acquisition of the shorter duration refill images impossible). In theory, slice separation can be decreased, and the decrease should improve image quality as slice spacing approaches the width of the elevational point-spread function.

3.4.2 Transducer and vessel parameter estimates

Based on the fits of all interval imaging frames of the vessel excluding outliers determined using Dixon's criteria as previously described (n=93), transducer parameters were estimated (see Table 3.1). After refitting the profiles with the constant physical parameters (a, B_{axial}, and $B_{elevational}$) held steady, values of A and α were obtained. An example of a vessel profile and its fitted curve is illustrated in Fig. 3.9. Due to the effects of beam shape and attenuation, note how A is generally not given by the peak of the fitted profile. The correlation coefficient between A and α was determined to be 0.767 ($p<0.001$) which is consistent with the linear relation with contrast concentration (related to A) and attenuation as reported in the literature [16]. The ratio $S=A_{scaled}/A$ accounting for the difference between the upper and lower regions of the kidney due to geometric differences in the beam was found to be 4.7 for the imaging transducer at the specified settings based on the measurement of the contrast phantom. This value was used to scale all estimated A values to their corresponding A_{scaled} values for the perfusion estimates.

3.4.3 Refill curve estimates

After normalizing all of the raw kidney cortex values by their corresponding A_{scaled} values just described, underlying refill curves were estimated. The refill curves for the 20 mm transverse slice are illustrated in Fig. 3.10. Combining all the interval imaging data for the transverse case (n=5 for slow flow; n=4 for fast flow after the exclusion of one set due to contrast agent anomalies) and dual transducer data (n=4 for both flow rates) at the 20 mm position, estimates were made of the perfusion in the kidney cortex.

Depicted in Fig. 3.11 are the refill curves for the selected longitudinal slice extracted from the dual transducer acquisitions. The exponential fit was used to estimate FBV and MTT when the correlation coefficient between FBV and MTT was less than 1. Otherwise, the linear fit was used to estimate perfusion without separately estimating the FBV and MTT. Points from the fast flow case tend to be dispersed more widely than points from the slow flow case. The similarity of the exponential and linear fits is shown for the DT fast flow cases in each orientation. Linear fits are illustrated in all the other plots. A comparison of measured perfusion values is shown in Fig. 3.12 for the 20 mm transverse slice. There was no statistical difference between the interval imaging and dual transducer results for each flow rate ($p>0.05$ for both rates and both models), with better agreement using the linear model (linear fit dual transducer results were 1.03 ± 0.26 and 1.08 ± 0.37 times interval imaging results for respectively slow flow and fast flow). In addition, perfusion estimates of the kidney cortex were obtained at a number of transverse slices from the dual transducer volumetric acquisitions. These estimates, all derived from the linear fit in order to facilitate comparisons, are shown in Fig. 3.13. The

perfusion varies within the cortex at differing slice locations. Changes in the perfusion follow similar trends at both input flow rates to the kidney, with a possible exception at the 25 mm position. The expected perfusion ratio of the fast flow cases to the slow flow cases would be 2, given the 2:1 ratio in infusion rates; however, the measured perfusion ratio of 5.7 ± 2.8 differed significantly ($p=0.013$) from 2. Estimates for the longitudinal slice are shown in Fig. 3.14. Since the longitudinal slice is composed of portions of the transverse slices, the perfusion values of the longitudinal slice were indeed not statistically different ($p>0.05$ for both slow and fast flow) from the values of the transverse slices, as determined by a Student t-test taking the transverse slice values as a group and comparing them to the longitudinal value.

The comparison between exponential and linear expressions in estimating perfusion for long transit times is depicted in Fig. 3.15. Given the exponential expression $y(t) = A[1-\exp(-t/\mathrm{MTT})]$ [8], with A denoting the FBV, if the measured points on the refill curve are distributed such that the FBV is well defined, then the linear fit substantially underestimates the perfusion. In contrast, when the points present on the curve only define the initial quasi-linear portion of the exponential expression, then the curve is well-approximated by a straight line of the form $y(t) = mt$. The degree of linearity between the FBV and MTT is given by their correlation coefficient. As the correlation coefficient increases, the apparent FBV and MTT increase along with their estimated errors (details given in appendix C). Were the correlation between FBV and MTT essentially 1, indicating that the measured points lie solely on the quasi-linear portion of the refill curve, an exponential cannot be fit to the data. As previously mentioned, perfusion can still be estimated using the linear fit under these circumstances.

3.5 Conclusions and discussion

In this chapter, the results of scanning a perfused vascular bed have been presented. The dual transducer technique allows the imaging of contrast destruction/refill in a three-dimensional volume in a shortened time frame, compared to traditional techniques (2D real-time refill and interval imaging taken at one location at a time). The results would be applicable toward analogous clearance/readout schemes that could be performed with a 2D array. A model was introduced that properly normalizes the measured signal intensity levels to a major vessel, accounting for both vessel (Fig. 3.5) and beam (Fig. 3.6) geometry. Estimation of the signal intensity corresponding to the contrast suspension $A_{100\%}$ is necessary to determine absolute perfusion; otherwise, perfusion estimates can only be relative, and would depend on the contrast suspensions being constant for all the cases being studied. The normalization to $A_{100\%}$ is suitable only for vessels located near the tissue in question due to the effects of overlying attenuation. Were they located far from each other, the differences in overlying attenuation would invalidate the normalization.

As previously mentioned, absolute perfusion values obtained using thermal diffusion of the porcine kidney cortex *in vivo* have been previously reported [2]. For the renal artery infusion rates examined there (with a peak rate of 102.1 ± 26.6 mL/min), the cortex perfusion (reported value of 68.1 ± 25 mL/100 g/min) scales linearly with the infusion rate. The perfusion measurements had standard errors that were essentially constant over the range of infusion rates greater than zero. Assuming a tissue density of 1 g/mL, the perfusion values described in this chapter at the high flow rate (around 0.003 s^{-}

= 18 mL/100 g/min as seen in Fig. 3.14) are not statistically different (p=0.43) from the perfusion value expected (22 mL/100 g/min) from their study after linear scaling to account for the reduced infusion rate. The infusion at the slow flow rate was less than the minimum non-zero rate measured there, and any comparison to an extrapolated value has limited utility. Nonetheless, the general consistency between the perfusion measurements reported here and those previously reported using thermal diffusion suggests that this approach is viable as a means of obtaining absolute perfusion measurements.

The acquired data presented in this chapter extended to a refill time of 150 s. In retrospect, had the acquisition included longer time points, estimates of the FBV and MTT would be more accurate, and would be possible in more cases. Such long refill times were the result of study limitations, namely the maximum input flow rate to the kidney phantom. As such, these refill times would not be expected *in vivo*. Nevertheless, the estimation of perfusion is useful in its own right, and being able to do so independent of acquiring latter portions of the refill curve may reduce the overall scan time.

The measured perfusion ratios of the fast flow cases to the slow flow cases differ from the expected value of 2, possibly due to variation within the phantom vasculature with flow rate changes. Nevertheless, the elimination of contrast from a block of tissue whose thickness is much larger than the imaging beam width (as in the dual transducer cases) did not result in statistically significant differences between perfusion measurements from that calculated from clearance at a single position (as in the interval imaging cases) at either flow rate. The reconstructed longitudinal images and their associated refill curves yielded results (Fig. 3.14) that were not statistically different ($p>0.05$) from those of the originally acquired transverse images, despite the fact that

contrast clearance was performed in the transverse orientation. This similarity further suggests that the measured perfusion may be independent of the contrast agent volumetric elimination pattern such as that from a 2D array configured to clear and readout the contrast refill with two independent beams. The independence of the measured perfusion from the contrast clearance pattern probably arises from the kidney cortex refill being dominated by capillary filling. Since the large vessels that feed the capillary bed fill rapidly after contrast clearance regardless of clearance zone or clearance manner, the subsequent capillary fill is not affected by clearance zone differences. In addition, the manner in which a volume is cleared, whether from the transducer used for the interval imaging sequence, the dual transducer clearance transducer, or likely by extension from pulses arising from a 2D array, does not affect the fact that contrast was cleared as long as the clearance is completed quickly in comparison to refill in the vascular space of interest. The contrast refill dynamics into the cleared region therefore are not expected to be affected by the manner of contrast clearance. The dual transducer technique was used to demonstrate the effects of volumetric scanning and several possible dual beam methods possibly available from 2D arrays that could be used to image a three-dimensional volume. The dual-beam techniques should be clinically applicable to living tissues in order to produce a practical means of obtaining three-dimensional absolute contrast perfusion images.

3.6 Appendix A – Estimation of baseline tissue harmonic signal

An estimation of the baseline tissue harmonic signal is possible without the subtraction image, if the contrast agent were stable throughout the course of the refill

curve acquisition. The signal intensities would simply be fitted to the exponential expression $y(t) = A[1\text{-}\exp(-t/MTT]) + C$, where C is the non-zero constant tissue harmonic. Normalization to $A_{100\%}$ would be performed after first subtracting C from every point on the curve. If the signal intensities do not extend sufficiently far in time to accurately delineate A, necessitating the use of a linear fit, C would be the y-intercept of the fitted line. However, since the contrast agent was not stable throughout the course of the refill curve acquisitions, a separate estimate of C was necessary, and it was obtained from the baseline values in the interval imaging sequence to then compute the subtraction images described.

3.7 Appendix B – Derivation of overlying thickness *d* as a function of geometry

Starting with Fig. 3.5(b), the overlying thickness of contrast agent d can be expressed in terms of the geometric parameters a, b, x, and y as follows. From the equation of an ellipse,

$$\frac{x^2}{a^2} + \frac{y^2}{b^2} = 1 \qquad \textbf{(3.4)}$$

the upper edge can be written in terms of x, a, and b

$$y = b\sqrt{1 - \frac{x^2}{a^2}}\,. \qquad \textbf{(3.5)}$$

Note how this expression is equal to d for all points (x_0, y_0) lying on the x-axis ($y_0 = 0$). Generalizing to any point (x_0, y_0),

$$d = b\sqrt{1 - \frac{x_0^2}{a^2}} - y_0 = b\sqrt{1 - \frac{x^2}{a^2}} - y\,. \qquad \textbf{(3.6)}$$

3.8 Appendix C – Effect of covariance on perfusion estimates

Covariance plays a significant role in the perfusion estimates described in this chapter. Its effects are especially large when the asymptotic limit of the refill curve is not well defined by the available data (i.e. there was insufficient elapsed time to substantially refill the tissue with contrast agent after clearance). When measured points only define the initial quasi-linear portion of the refill curve, a large family of exponential curves can fit the points well. Given this situation, the errors of the parameters *A* and *B* (*B* being the MTT) in the expression *y(t)=A[1-exp(-t/B)]* become large (described in more general terms here [17]). As the covariance between A and B approaches 1, their estimated errors grow without bound. However, the perfusion is the ratio *r=A/B* as previously described. The error of *r* is described by eqn 3.7 [18].

$$\mathrm{var}(r) = \begin{bmatrix} \frac{\partial r}{\partial A} & \frac{\partial r}{\partial B} \end{bmatrix} \begin{bmatrix} \sigma_A^2 & \sigma_{AB} \\ \sigma_{AB} & \sigma_B^2 \end{bmatrix} \begin{bmatrix} \frac{\partial r}{\partial A} \\ \frac{\partial r}{\partial B} \end{bmatrix} \qquad \textbf{(3.7)}$$

where

var(*r*) is the variance of *r*,

$\partial r/\partial A$ and $\partial r/\partial B$ are the partial derivatives of *r* with respect to *A* and *B*,

σ_A^2, σ_B^2 are the variances of A and B,

and σ_{AB} is the covariance between A and B.

Expanding eqn 3.7 yields

$$\mathrm{var}(r) = \left(\frac{\partial r}{\partial A}\right)^2 \sigma_A^2 + 2\left(\frac{\partial r}{\partial A}\right)\left(\frac{\partial r}{\partial B}\right)\sigma_{AB} + \left(\frac{\partial r}{\partial B}\right)^2 \sigma_B^2 \qquad \textbf{(3.8)}$$

The first and third terms are always positive. The second term though is negative for positive σ_{AB} given the partial derivatives of r ($\partial r/\partial A = 1/B$ and $\partial r/\partial B = -A/B^2$). The covariance between FBV and MTT was found to be positive during refill curve estimation. A sufficiently large covariance would then cause the variance of the perfusion to be less than that of either the FBV or MTT. This effect from the covariance accounts for the precision of perfusion estimates obtained through an exponential fit in spite of large errors in FBV and MTT estimates. Illustrated in Fig. 3.16 are the experimental results of estimates of the FBV, MTT, and perfusion $r = FBV/MTT$ (all found with an exponential fit) as a function of the correlation coefficient between FBV and MTT. As the correlation coefficient between FBV and MTT increase, estimates of both the FBV and MTT rise along with their error estimates. However, perfusion values remain relatively steady due to the effects of covariance.

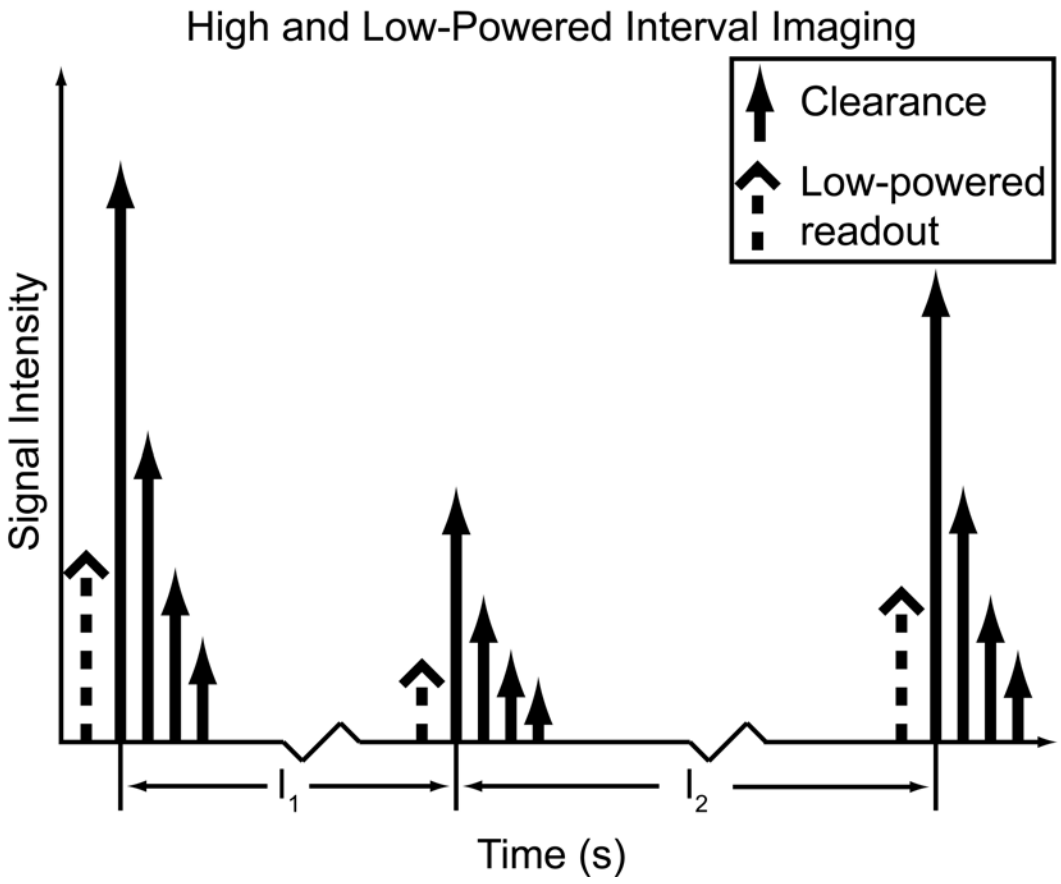

Fig. 3.1. Traditional and low-power interval imaging. In a traditional interval imaging sequence, a series of high-power pulses is applied starting with the tissue being fully perfused and clearing the volume of contrast. After waiting durations *I*, additional clearance sequences are fired. The signal intensity from the first clearance frame of each sequence corresponds to the level of refill in interval *I*. Combining the refill levels after various intervals produces a refill curve. Inserting a minimally destructive low power frame immediately prior to the start of the clearance sequences allows the measurement at low power of the contrast agent signal immediately prior to each clearance sequence. These low-power data can then be directly compared to dual transducer measurements of the same volume.

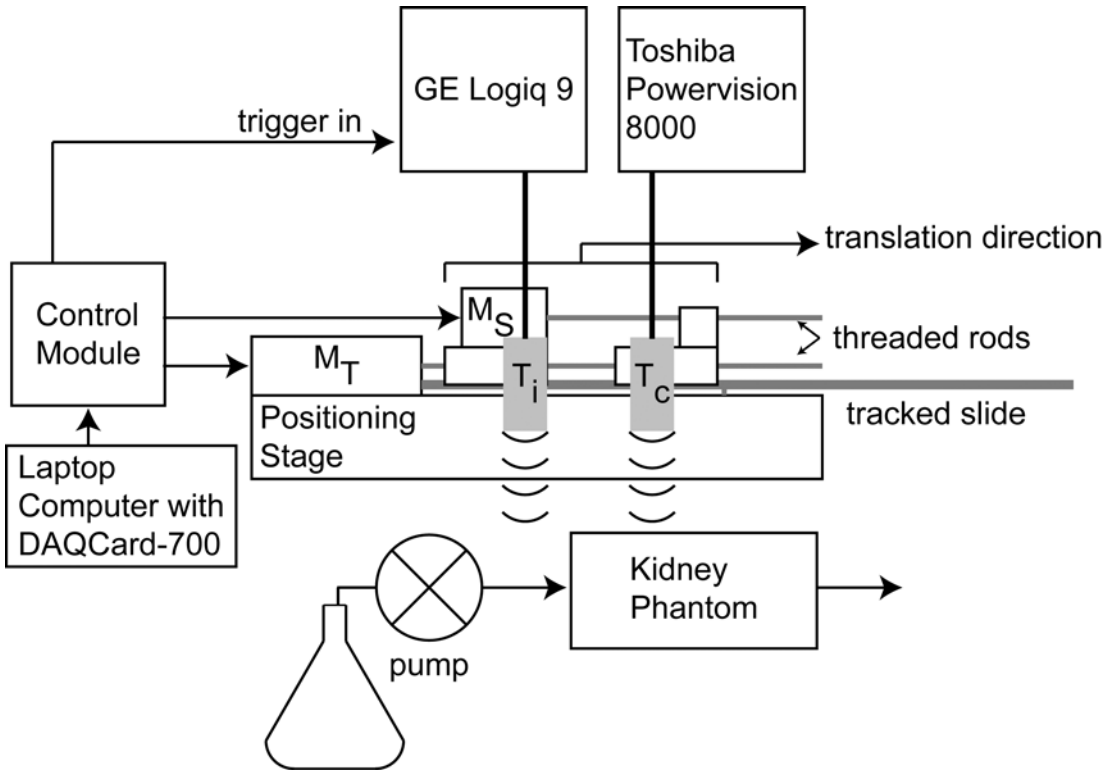

Fig. 3.2. Schematic of dual transducer apparatus and experimental setup. The dual transducer apparatus, slightly modified from that apparatus described in chapter 2, consists of a dual transducer positioning stage driven by translation (M_T) and separation (M_S) motors. A trigger was added to the control module to control image acquisition by the GE Logiq 9. The clearance transducer is positioned at the edge of the volume of interest. A pump continuously delivers dilute contrast agent from a stirred flask to the phantom. Contrast agent is pumped through the phantom without recirculation.

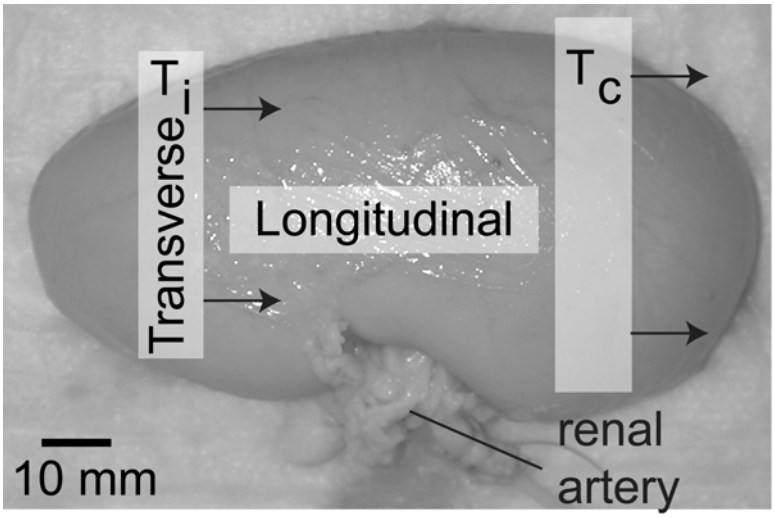

Fig. 3.3. Kidney phantom with transducer orientations. The kidney phantom is perfused through the renal artery that is connected to a pump. All dual transducer scans are acquired by translating the transducers (T_i and T_c refer to the imaging and clearance transducers, respectively) as indicated by the arrows, with the transducers oriented in the transverse orientation. Interval imaging was performed in the transverse orientation for a selected slice that constitutes a portion of the scanned volume. Reconstructed images in the longitudinal direction, extracted from scans performed using the dual transducer technique, are oriented perpendicular to the transverse orientation as shown.

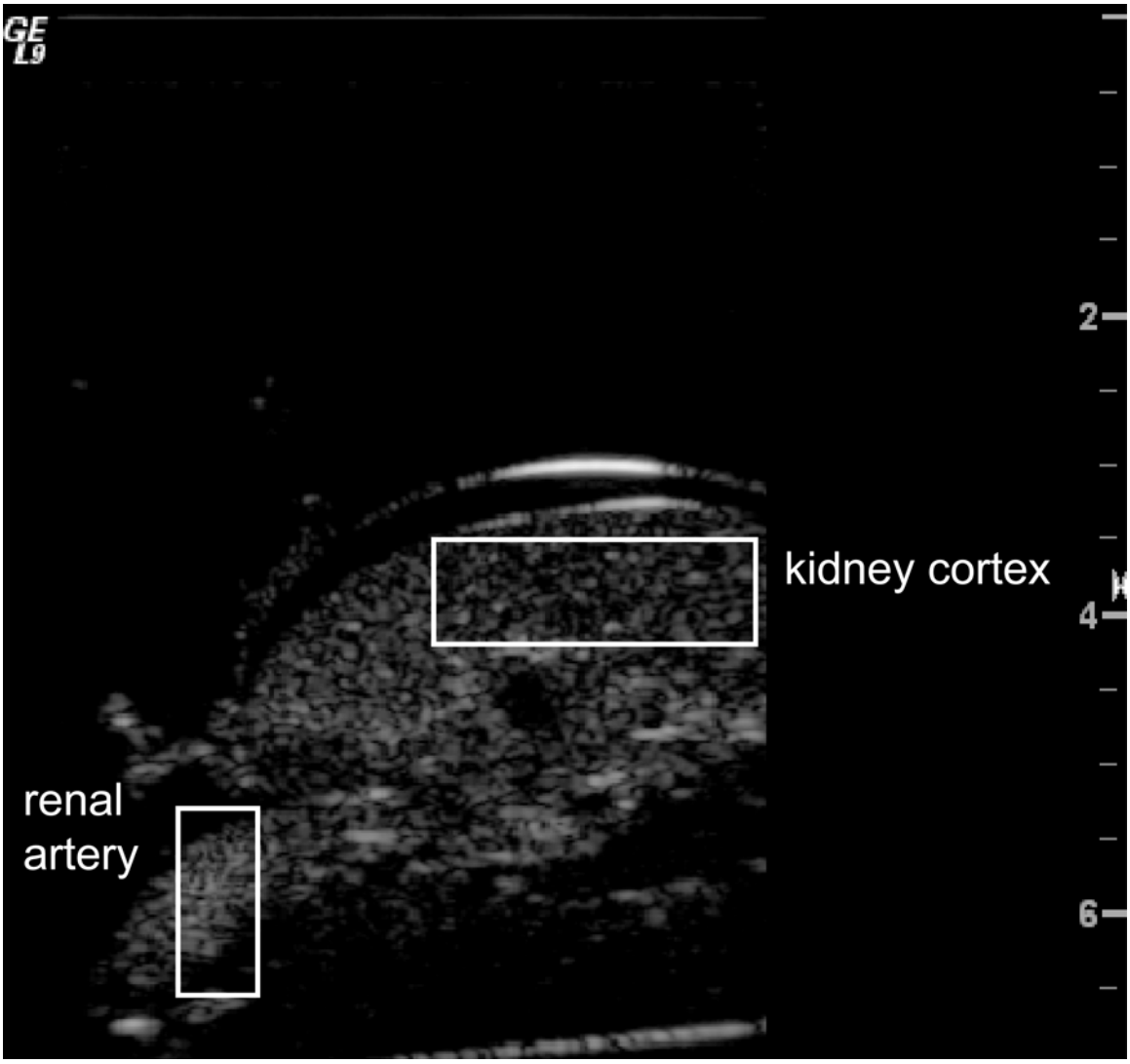

Fig. 3.4. Example of kidney image. Depicted is a transverse image of the kidney phantom with ROIs indicated in both the cortex and renal artery. The renal artery is considered a major vessel that is always filled with contrast. From the signal profile across the vessel in the axial direction, a value *A* equal to the signal intensity of the contrast suspension can be derived (details in text). This value *A* can be used to correct for variations with the infused contrast agent suspension.

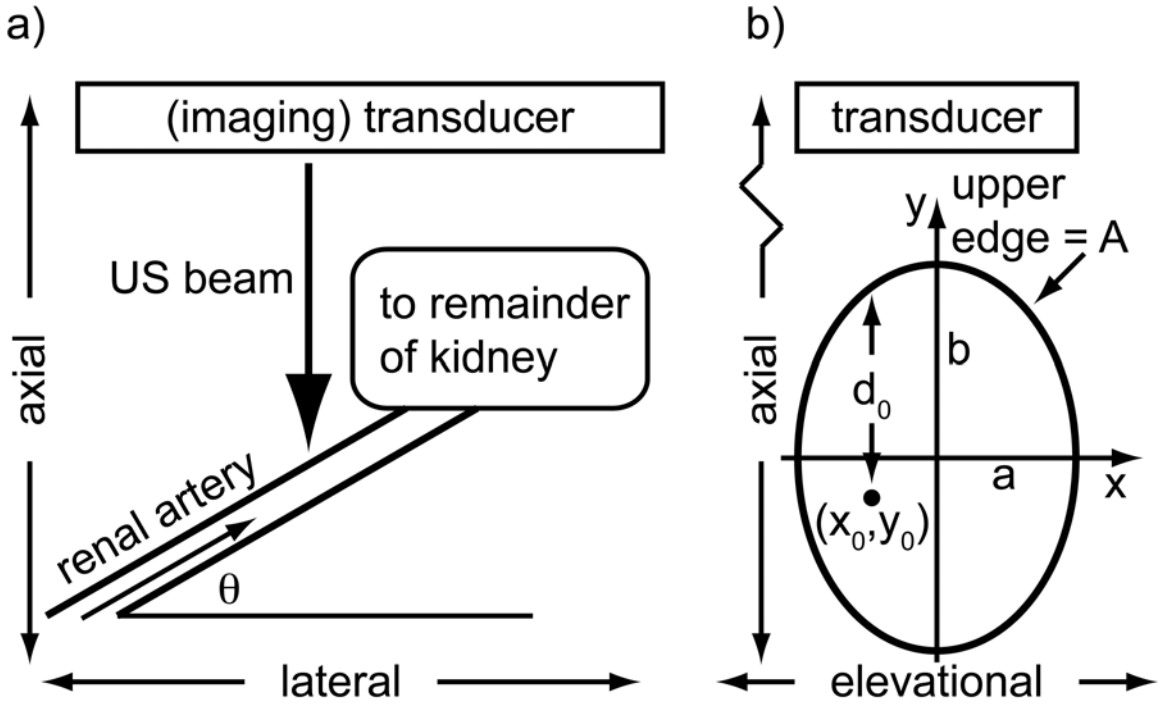

Fig. 3.5. Renal artery normalization model with imaging transducer directions indicated. a) The renal artery is modeled as a cylindrical tube tilted at an angle θ from the horizontal, in the same plane as the transducer. The contrast agent is intercepted by the ultrasound beam as shown. b) The intersection of the beam with the artery is an ellipse with a vessel radius a. From the geometry, the semi-major axis $b = a/\cos\theta$. The distance d_0 from the upper-half of the curve determines the level of attenuation the agent experiences at any point (x_0, y_0) due to overlying contrast, while the unattenuated upper edge has a baseline signal level of A. The integration of the signal levels across the vessel at each depth yields the observed intensity profile (see details in the text).

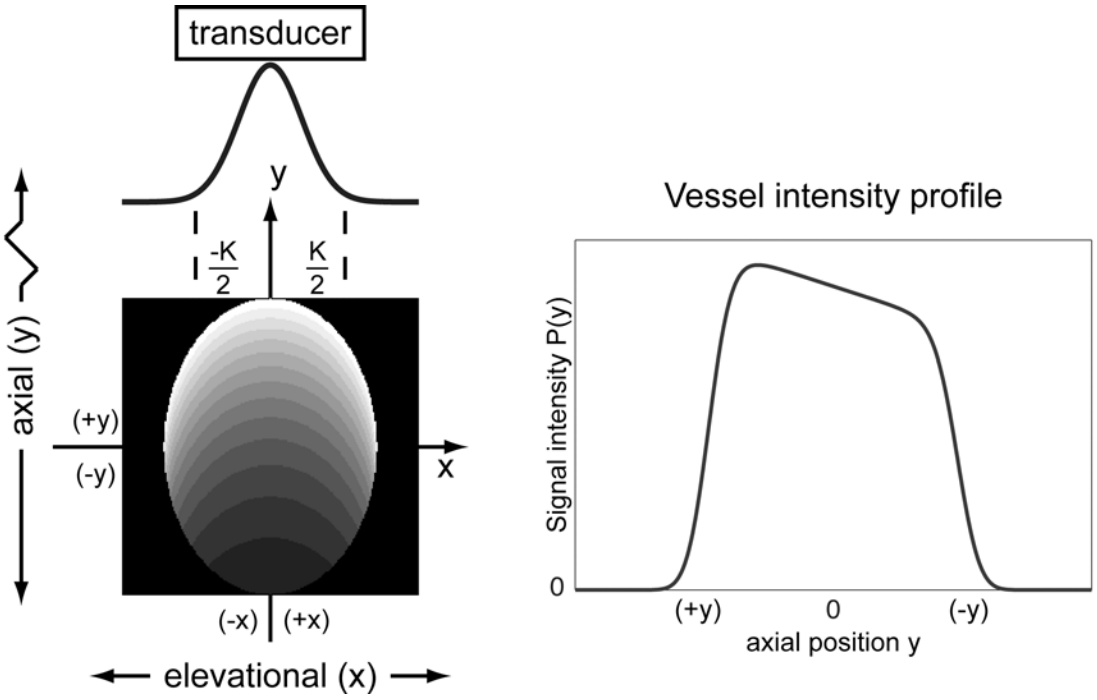

Fig. 3.6. Computation of vessel profile. The intensity profile across the vessel is computed as follows. At every axial position *y*, the signal intensity *P(y)* is the integration of all the intensities at *y* with respect to the elevational direction x. These intensities are weighted by $B_{elevational}$ prior to integration in order to account for the elevational beam shape. Due to the presence of attenuation from contrast agent, the intensity *F(x,y)* is non-uniform and is given in the text. An example of a vessel intensity profile is depicted on the right. Note how the presence of attenuation causes the peak of *P(y)* to shift toward the transducer from the vessel center.

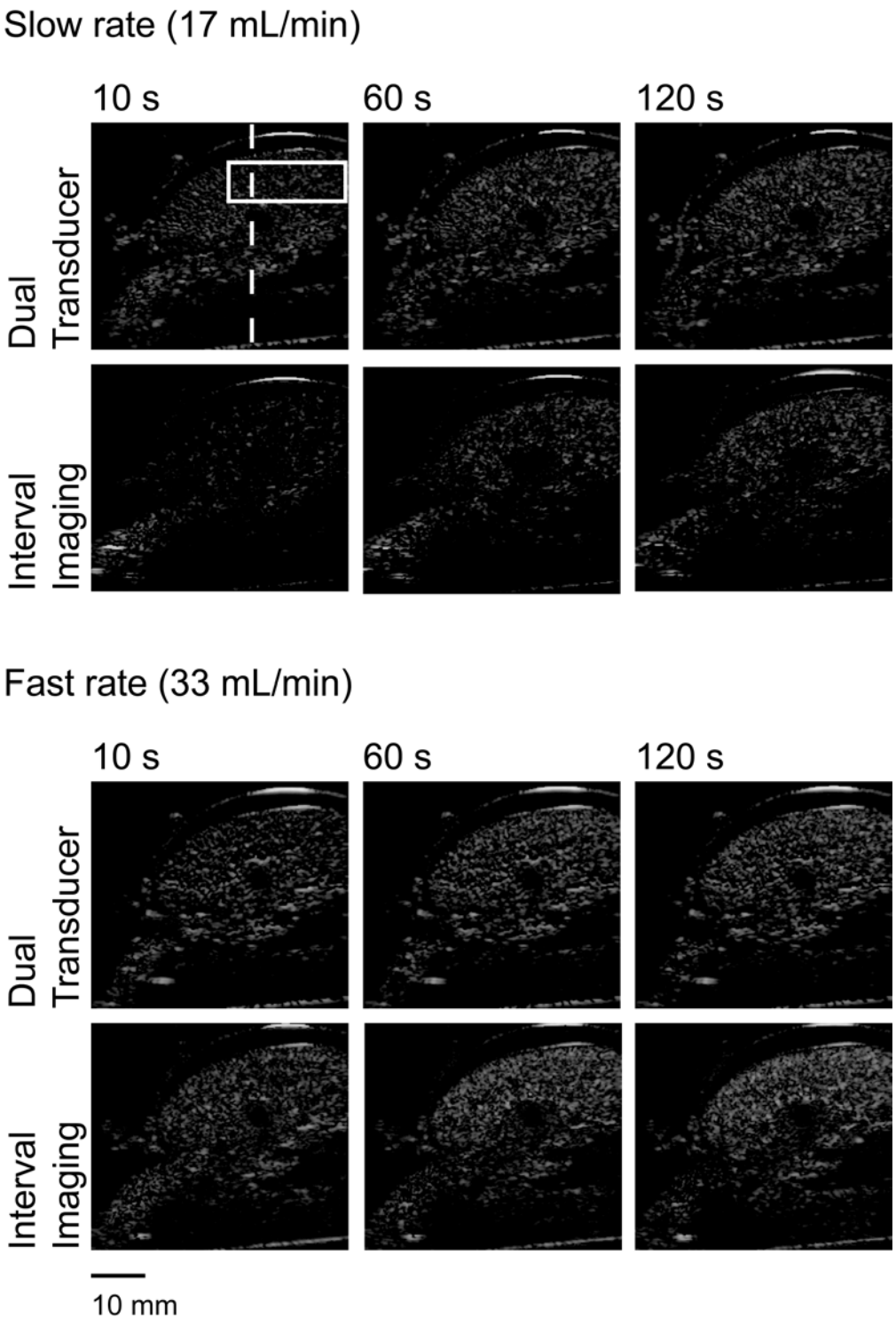

Fig. 3.7. Representative ultrasound subtraction images obtained from a transverse slice (20 mm position) from preserved porcine kidney with low-power II and the dual-transducer technique. The kidney cortex ROI is indicated by the white box. The dashed line indicates the orientation of the longitudinal slice examined with respect to the transverse slice. Note the increased echogenicity as the kidney fills with contrast over time.

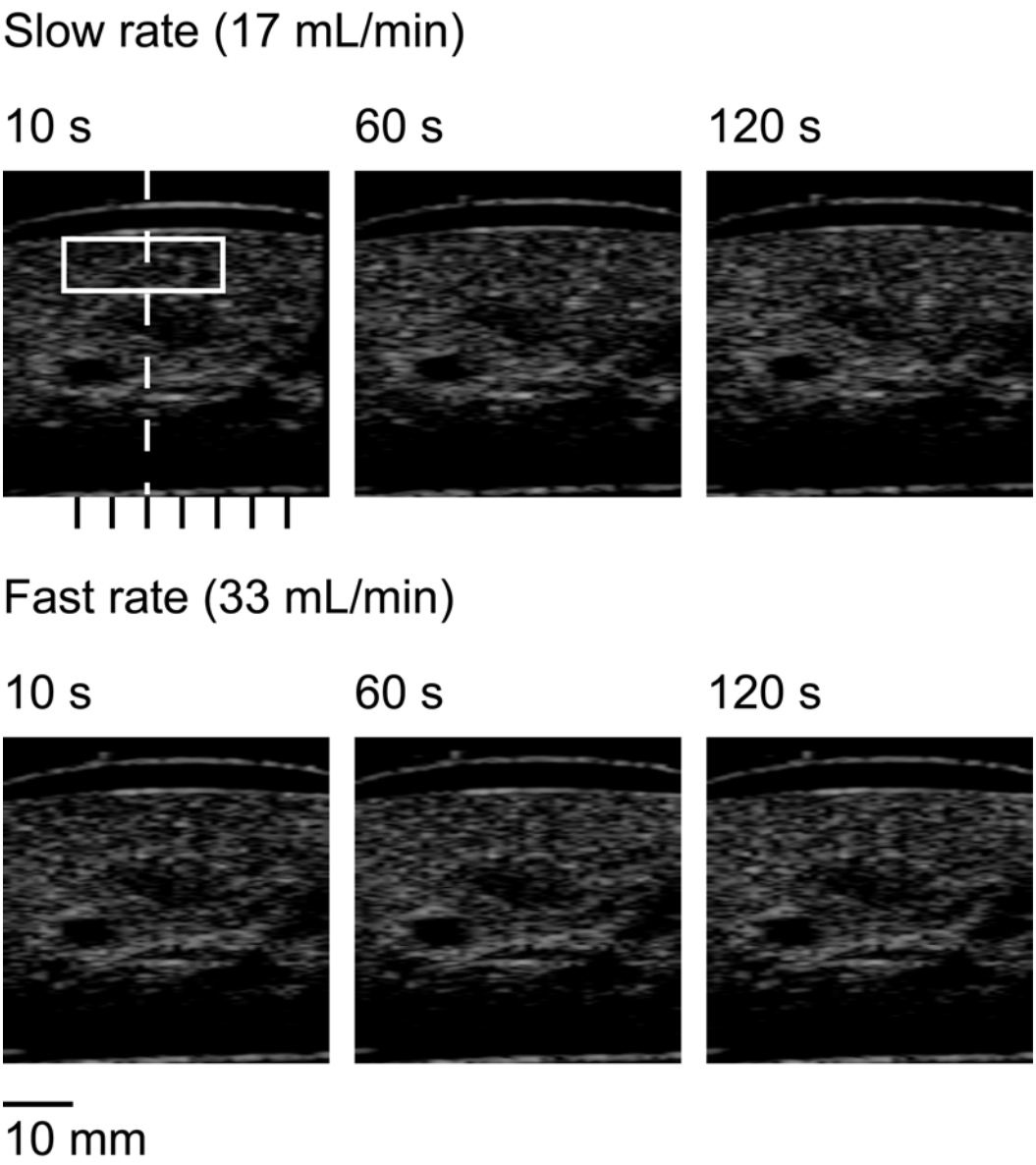

Fig. 3.8. Representative DT longitudinal images. Analogous to the images in Fig. 3.7, the kidney is shown to fill with time. The reconstructed images are of lower quality than those directly obtained because the transducer point-spread function in the elevational direction is wider than in the lateral direction. In addition, the transducer spacing affects image quality in the reconstructed images. The longitudinal ROI is indicated by the white box, with the location of the 20 mm transverse slice shown by the dashed line. The locations of the other examined transverse slices from 10 to 40 mm are indicated by markers located beneath the image. Since these images are *not* subtraction images, the change in contrast levels is less apparent than those shown for the transverse cases in Fig. 3.7.

	a	B_{axial} (FWHM)	$B_{elevational}$ (FWHM)
Value (mm)	2.9	1.3	6.3
Standard error	0.05	0.10	0.53

Table 3.1. Transducer parameters for the imaging transducer and renal artery radius a. Values corresponding to estimates made from fitting observed contrast profiles across the renal artery (n=93) are indicated. Both B_{axial} and $B_{elevational}$ are modeled as Gaussian curves, with their full width at half-maximum (FWHM) values indicated. Their values were subsequently fixed at these means and contrast profiles refit in order to obtain estimates of A and α.

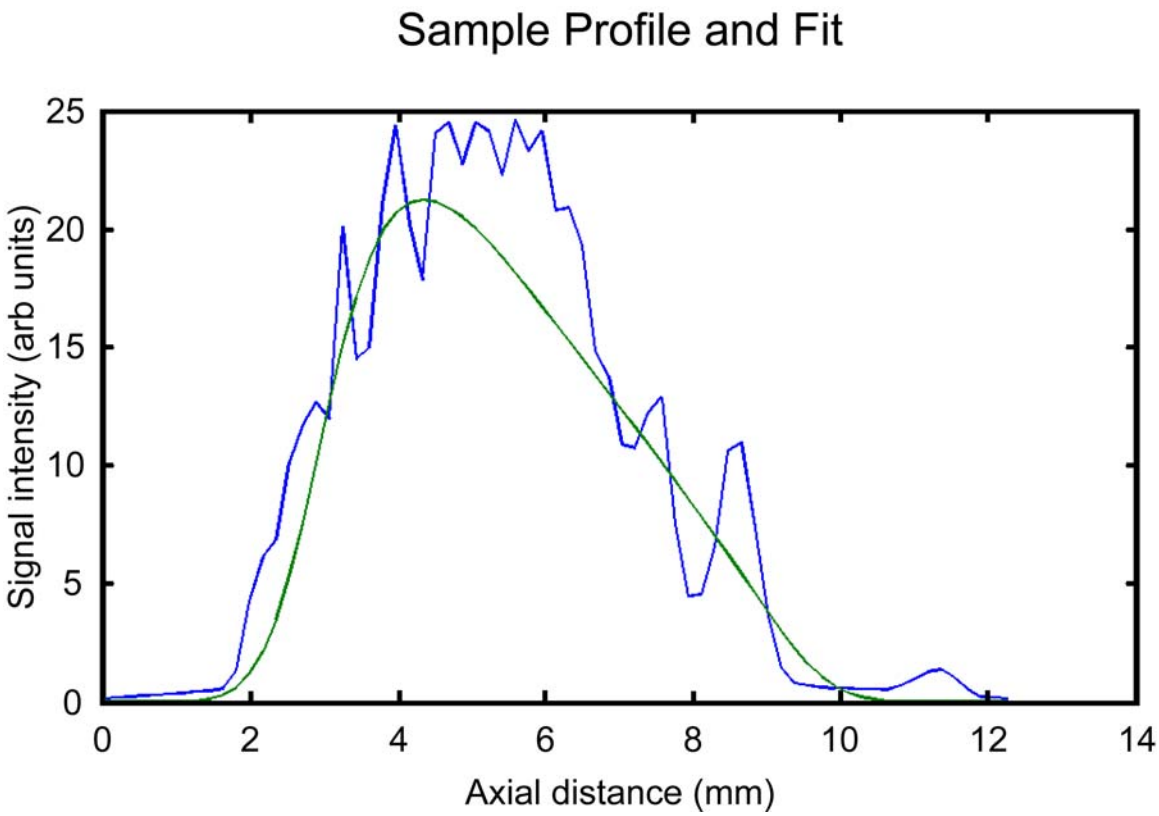

Fig. 3.9. Sample vessel intensity profile through renal artery. The signal intensity through the renal artery, oriented as described in the model illustrated in Fig. 3.5, is plotted with zero being the axial distance of the renal artery ROI closest to the transducer. The fitted curve (described in the text) is used to estimate A for the image with this profile. Note that, due to beam shape and attenuation effects, A is not the peak of the fitted curve.

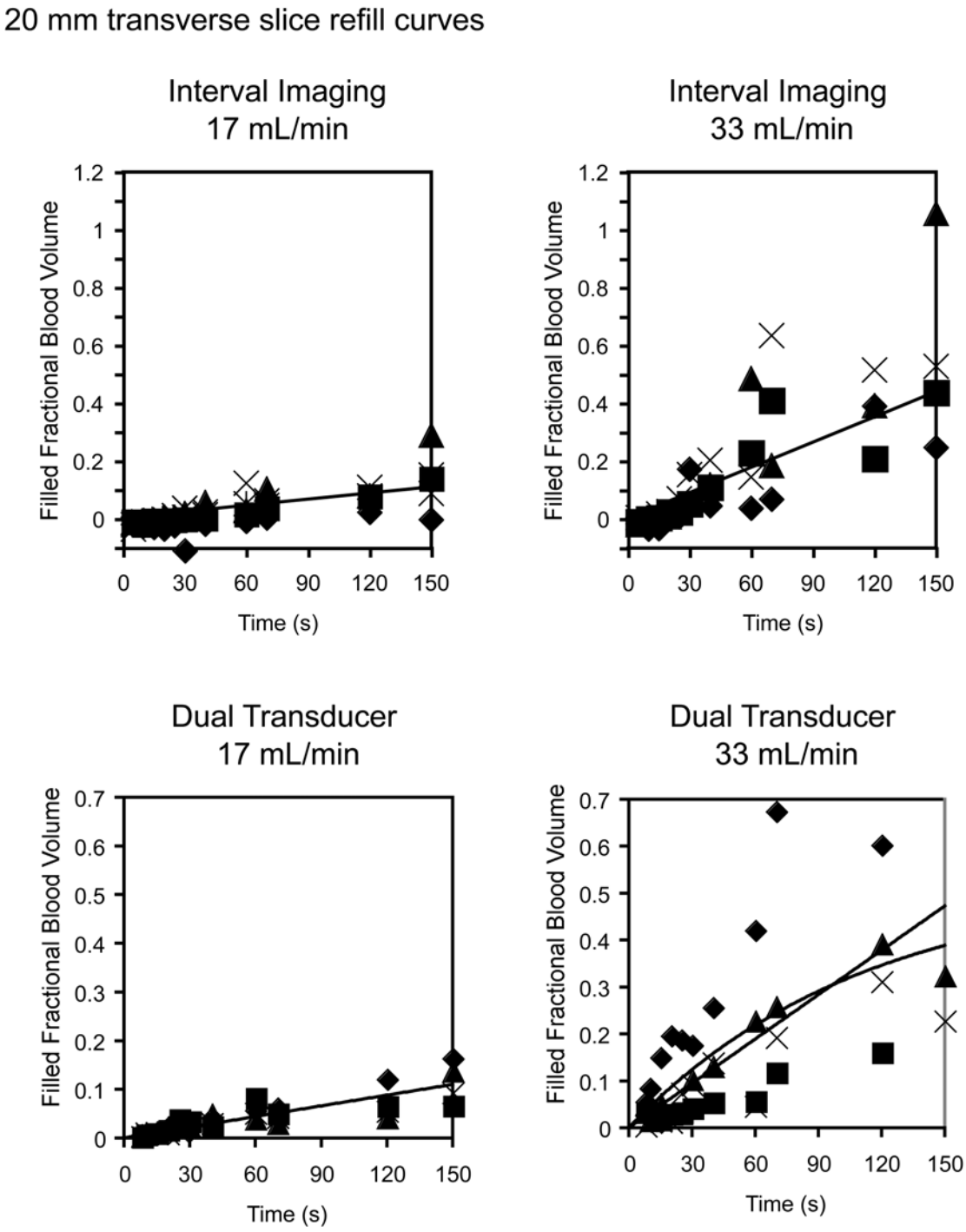

Fig. 3.10. Fitted curves for each refill scenario (transverse slice - 20 mm position). Shown are normalized data points for each refill scenario (acquisition method, flow rate) and their fitted curve. Symbols denote individual acquisitions (each individual n) where a contrast suspension was prepared. One sees the similarity between results from the two techniques as well as the difference with the change in flow rate. The 17 mL/min cases along with the 33 mL/min II scenario were fitted with linear fits because acquired data did not extend sufficiently to permit fitting to the exponential equation. The 33 mL/min DT case depicts both its linear fit and fitted exponential.

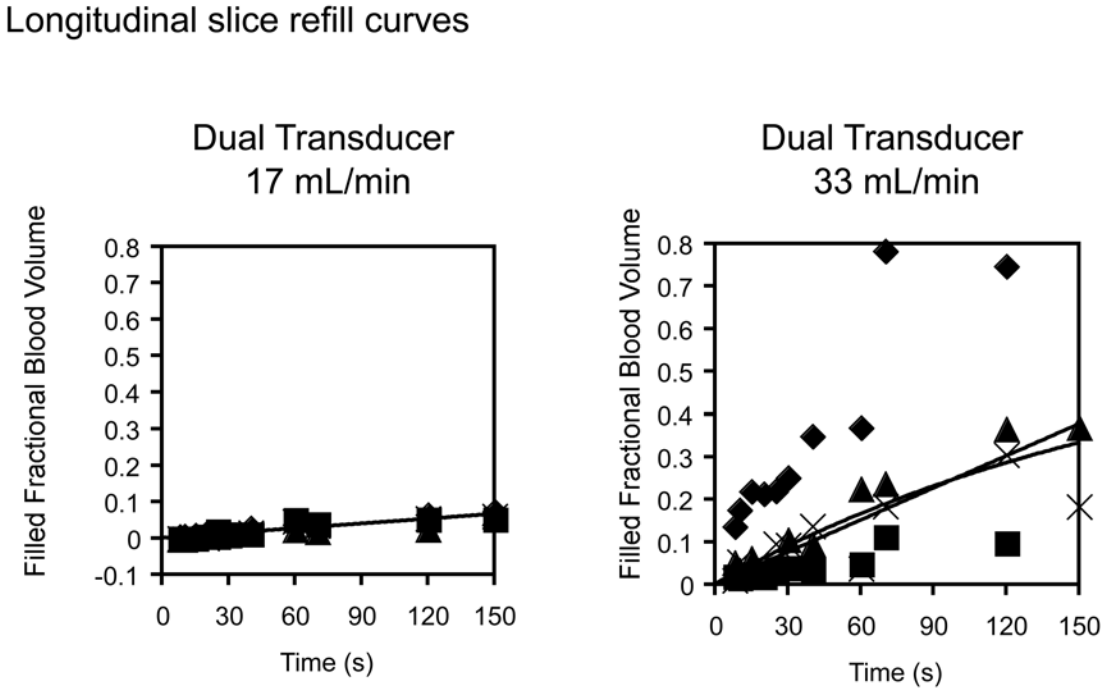

Fig. 3.11. Fitted refill curves for the reconstructed longitudinal cases. Analogous to Fig. 3.10, the normalized data points for each flow rate are plotted with their fitted curve. Since the longitudinal images are extracted from the DT imaging, the normalization factors A_{cortex} used to normalize the obtained values are identical to the ones used for the DT transverse cases.

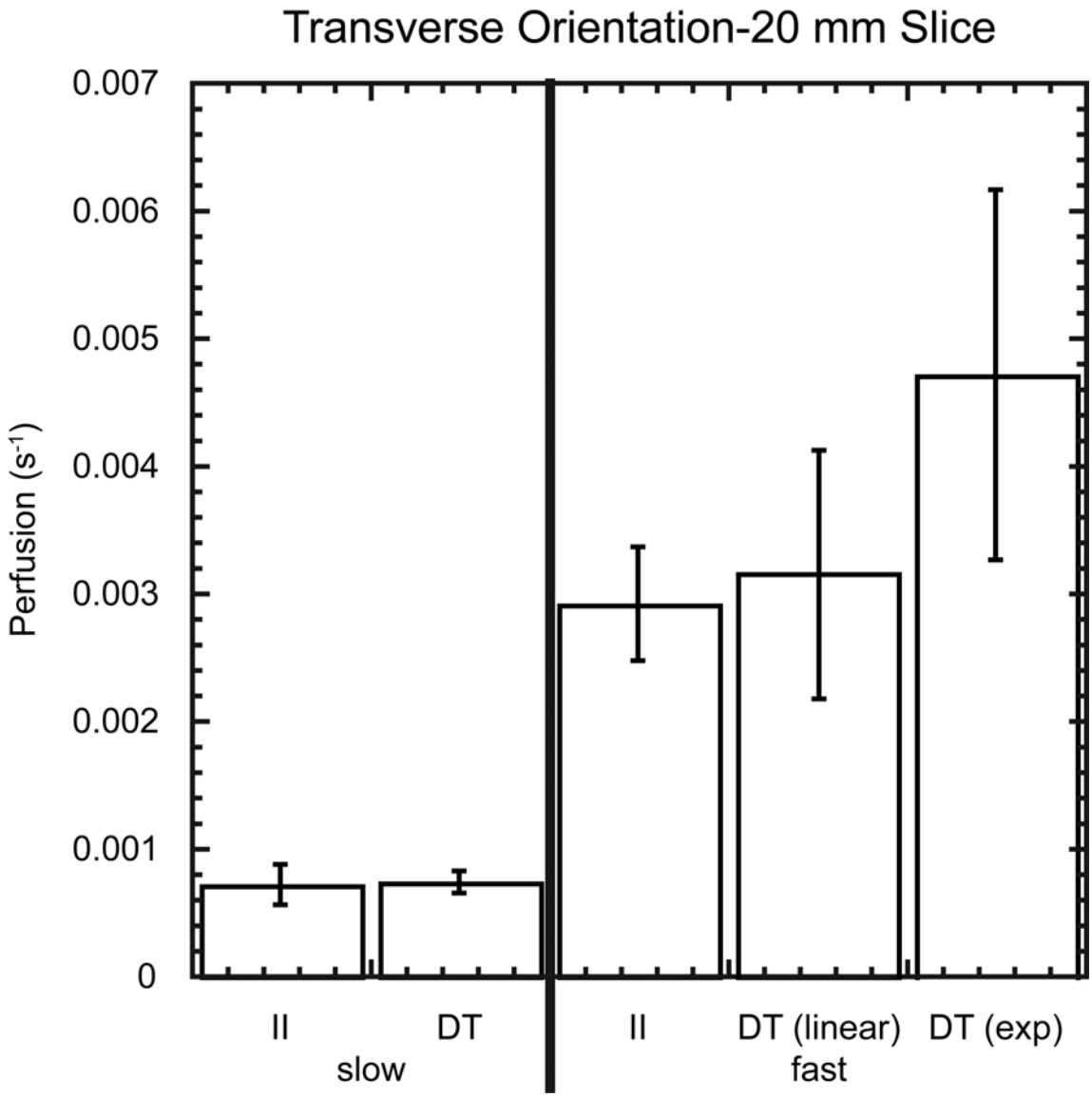

Fig. 3.12. Comparison of perfusion estimates for low-power interval imaging (II) and the dual transducer (DT) technique (20 mm position transverse slice). Slow and fast refer to the renal artery input flow rates of 17 and 33 mL/min. Error bars refer to estimated (±1 standard deviation) errors in the measurement of the parameters in question. The fast flow DT measurements were fit using both the linear and exponential models. All other measurements were fit using the linear model. The DT perfusion estimates using the linear model appear consistent (slow flow p=0.81, fast flow p=0.68) for both flow rates with those measured through II. The perfusion estimate from the exponential model fit also was not inconsistent with the II value (p=0.08).

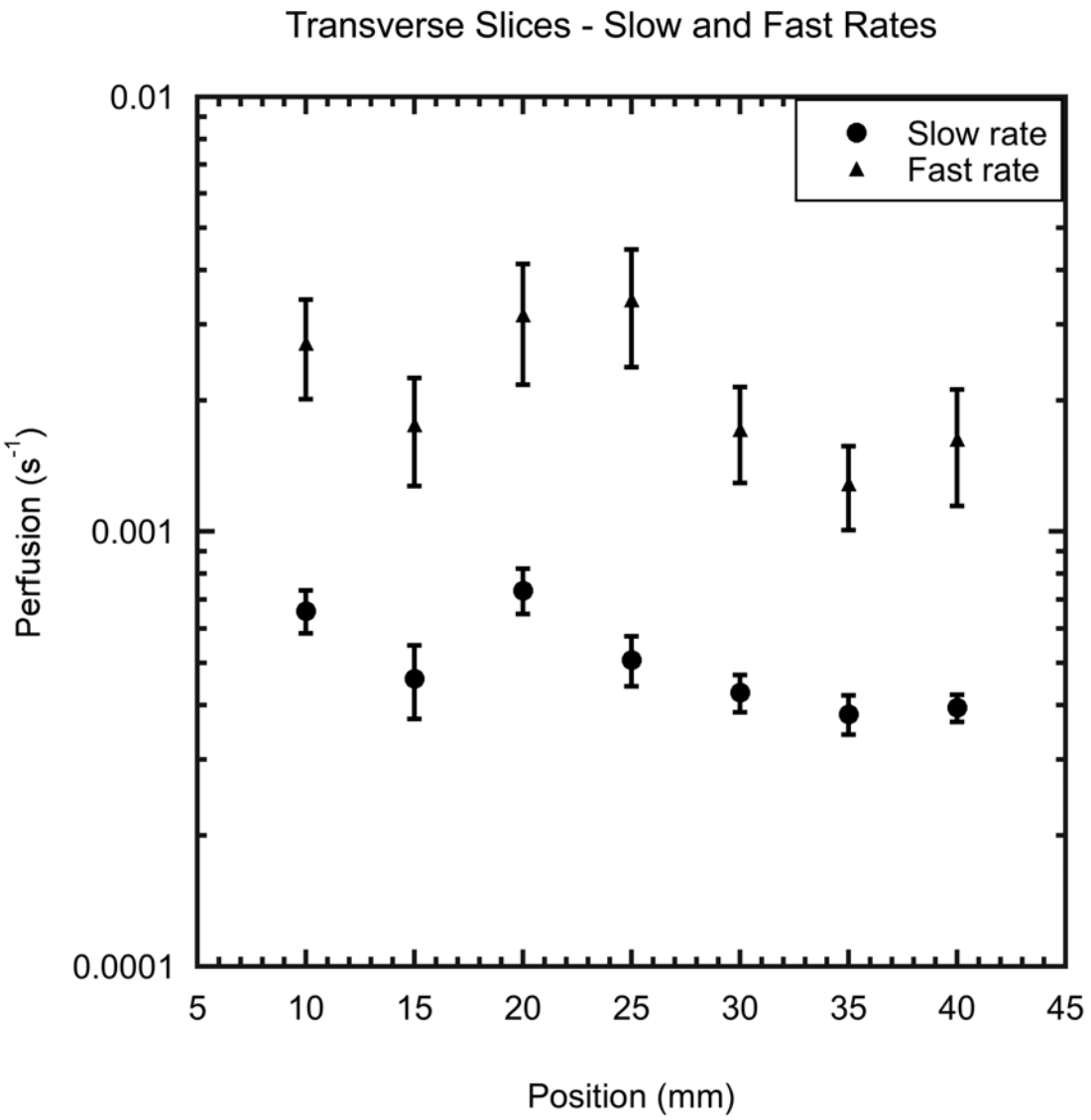

Fig. 3.13. Kidney cortex perfusion values, estimated using the linear fit in order to facilitate comparisons, for selected transverse slices throughout the imaging volume. The measured perfusion at the fast rate was 5.7 ± 2.8 times that of the corresponding slow rate. The fast rate to slow rate perfusion ratio was statistically different ($p=0.013$) from the expected value of 2. With the possible exception of the 25 mm position, perfusion trends through the volume were consistent with the change in flow rate.

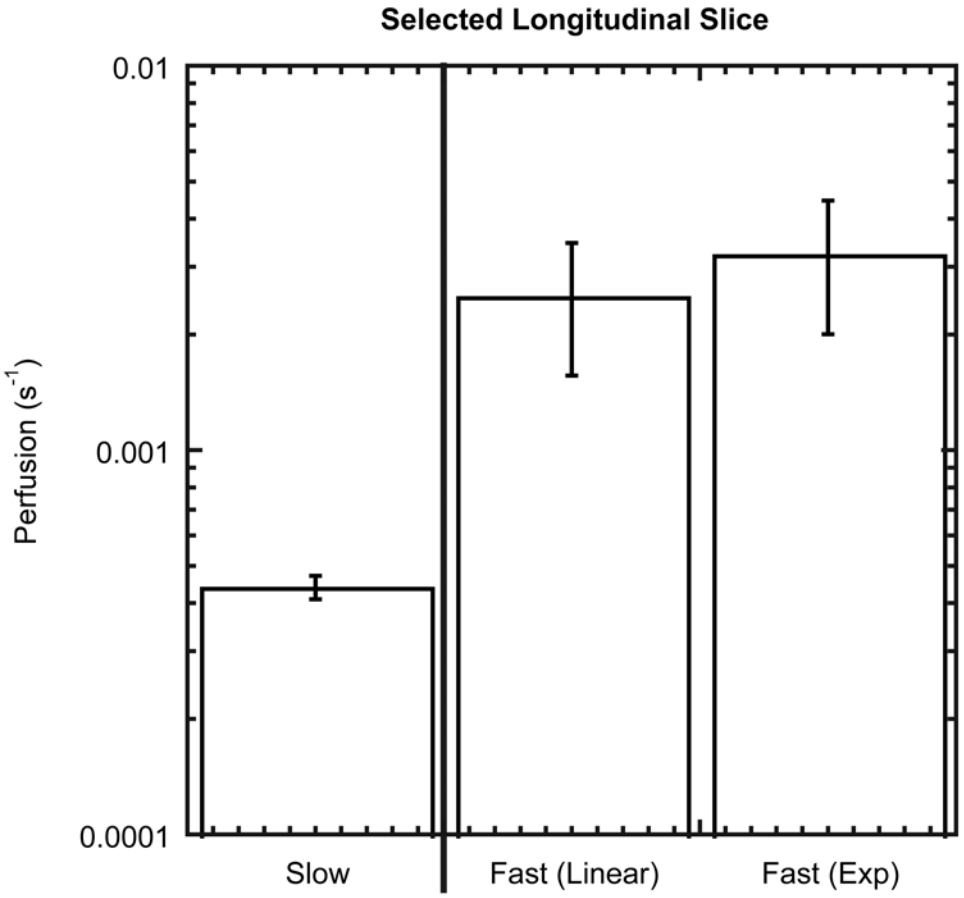

Fig. 3.14. Comparison of perfusion of the selected longitudinal slice at both flow rates (slow and fast being respectively 17 and 33 mL/min). The ratio of the fast rate (linear fit) to slow rate perfusion was found to be 5.7 ± 2.2, which is statistically different ($p<0.05$) from the expected value of 2.

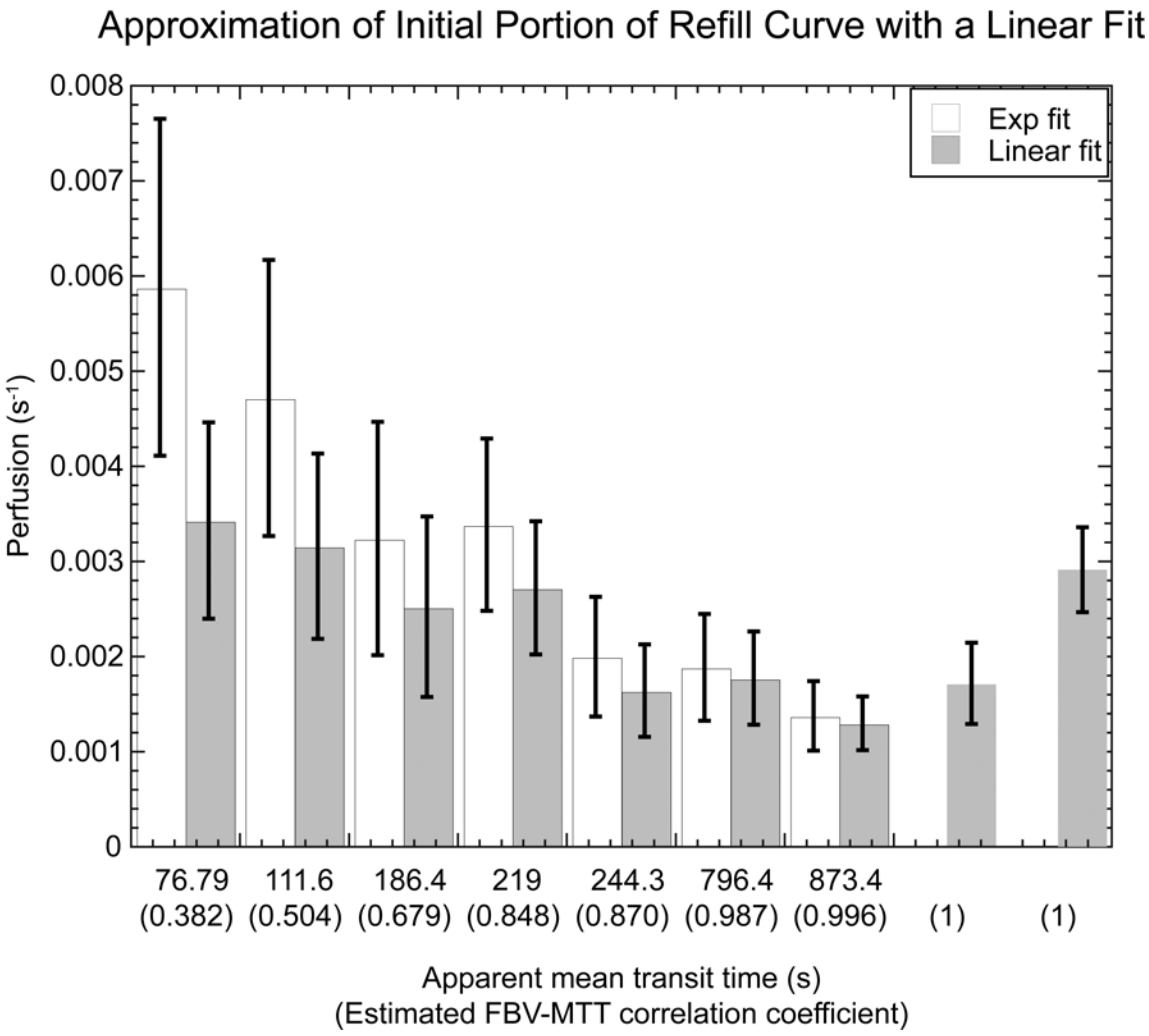

Fig. 3.15. Approximation of the initial portion of the refill curve. Shown are the perfusion estimates found using both an exponential fit and a linear fit approximation for all fast flow cases plotted as a function of their apparent MTTs and estimated correlation coefficients between FBV and MTT from the exponential fit. The horizontal axis denotes the apparent MTT and the correlation coefficient between FBV and MTT. An exponential cannot be fit to the data as the correlation coefficient approaches 1. The horizontal axis is labeled “apparent” MTT because it is strongly suspected that the actual transit time is significantly shorter, with a corresponding reduced FBV (the 796.4 s and 873.4 s MTT cases had physically impossible values of A of 1.49 and 1.19 respectively).

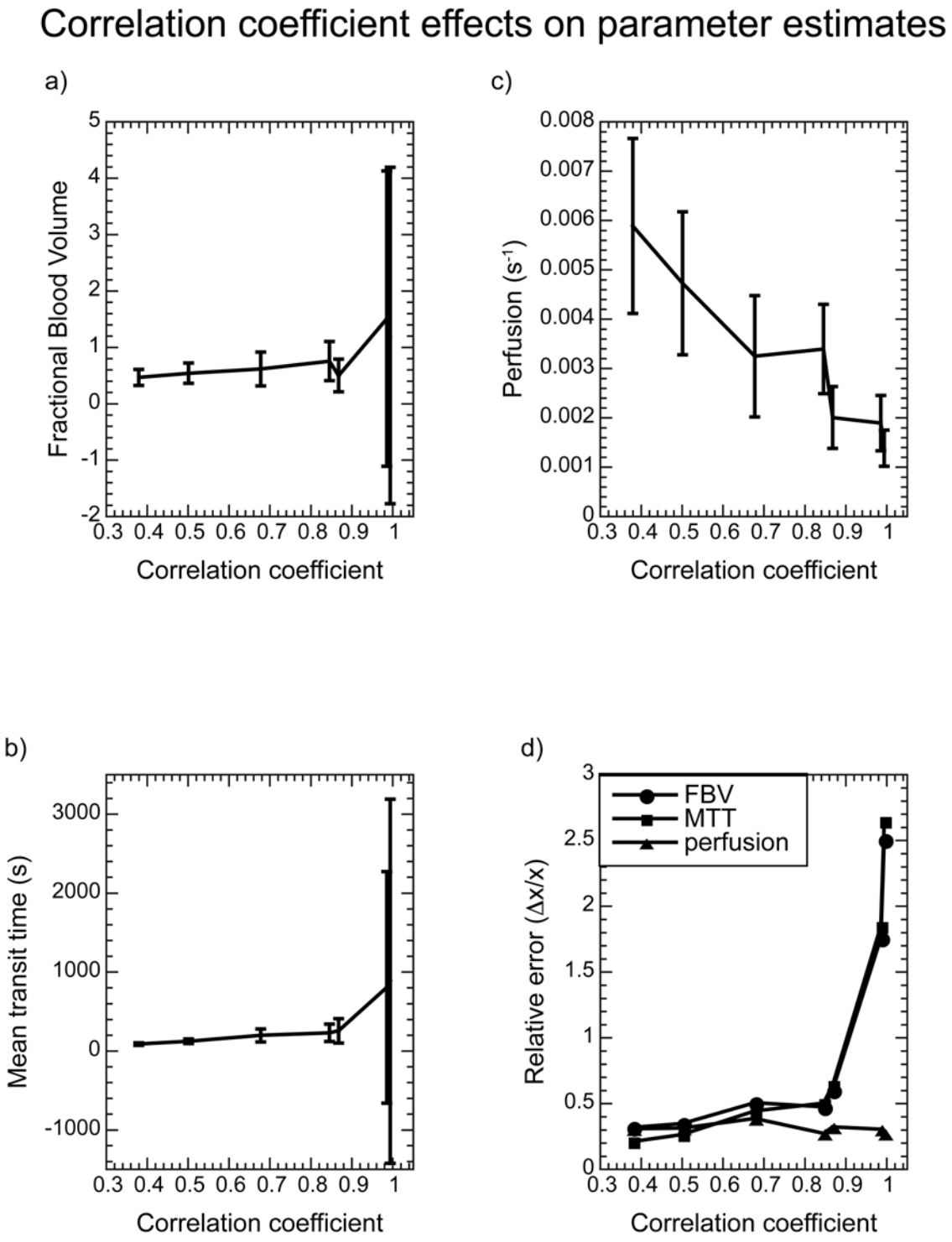

Fig. 3.16. Effects of correlation coefficient between FBV and MTT on estimated parameters. Shown are the parameter estimates of the cases where the refill curve was estimated using the exponential expression y(t) = FBV[1-exp(-t/MTT)] plotted as a function of the estimated correlation coefficient between a) FBV and b) MTT. As the coefficient approaches 1, both the estimated parameters and their errors show large increases. c) The perfusion, *r = FBV/MTT*, however, does not exhibit this effect due to the effects of covariance on error estimates. d) The relative error (error of parameter/value of parameter) of the FBV and MTT also shows a large increase as the correlation coefficient approaches 1.

3.9 References

[1] Holmes KR, Ryan W, Weinstein P, Chen MM. A fixation technique for organs to be used as perfused tissue phantoms in bioheat transfer studies. ASME ADV BIOENG, 1984; 9-10.

[2] Kraus T, Klar E, Osswald BR, Fernandes L, Mehrabi A, Gebhard MM, Herfarth C. Continuous Measurement of Porcine Renal Cortex Microcirculation with Enhanced Thermal Diffusion Technology. J. Surg. Res. 1996; 61: 531-536.

[3] Chen NG, Fowlkes JB, Carson PL, Schipper MJ, LeCarpentier GL. Rapid 3D Imaging of Contrast Flow: Application in a Perfused Kidney Phantom. Ultrasound Med Biol 2008 (in press).

[4] Schlosser T, Pohl C, Veltmann C, Lohmaier S, Goenechea J, Ehlgen A, Köster J, Bimmel D, Kuntz-Hehner S, Becher H, Tiemann K. Feasibility of the flash-replenishment concept in renal tissue: which parameters affect the assessment of the contrast replenishment? Ultrasound Med Biol 2001; 27(7): 937-944.

[5] Kamiyama N, Moriyasu F, Mine Y, Goto Y. Analysis of flash echo from contrast agent for designing optimal ultrasound diagnostic systems. Ultrasound Med Biol 1999; 25(3): 411-420.

[6] Moriyasu F, Kono Y, Nada T, Matsumura T, Suginoshita V, Kobayashi K. Flash echo (passive cavitation) imaging of the liver by using US contrast agents and intermittent scanning sequence. Radiology 1996; 201(374).

[7] Marsh JN, Hughes MS, Hall CS, Lewis SH, Trousil RL, Brandenburger GH, Levene H, Miller JG. Frequency and concentration dependence of the backscatter coefficient of the ultrasound contrast agent Albunex. J Ac Soc Am 1998; 104: 1654-1666.

[8] Wei K, Jayaweera AR, Firoozan S, Linka A, Skyba DM, Kaul S. Quantification of Myocardial Blood Flow With Ultrasound-Induced Destruction of Microbubbles Administered as a Constant Venous Infusion. Circulation 1998; 97(5): 473-483.

[9] Potdevin TC, Fowlkes JB, Moskalik AP, Carson PL. Analysis of refill curve shape in ultrasound contrast agent studies. Med Phys. 2004; 31(3): 623-632.

[10] Arditi M, Frinking PJA, Zhou X, Rognin NG. A New Formalism for the Quantification of Tissue Perfusion by the Destruction-Replenishment Method in Contrast Ultrasound Imaging. IEEE Trans. Ultrason. Ferroelect., Freq. Contr. 2006; 53(6): 1118-1129.

[11] Lucidarme O, Franchi-Abella S, Correas JM, Bridal S, Kurtisovski E, Berger G. Blood flow quantification with contrast-enhanced US: “Entrance in the section” phenomenon-Phantom and rabbit study. Radiology 2003; 228: 473-479.

[12] Fleischer AC, Niermann KJ, Donnelly EF, Yankeelov TE, Canniff KM, Hallahan DE, Rothenberg ME. Sonographic Depiction of Microvessel Perfusion: Principles and Potential. J Ultrasound Med 2004; 23:1499-1506.

[13] Waller KR, O’Brien RT, Zagzebski JA. Quantitative contrast ultrasound analysis of renal perfusion in normal dogs. Vet Radiol Ultrasound 2007; 48(4): 373-377.

[14] Kallel F, Bertrand M, Meunier J. Speckle Motion Artifact Under Tissue Rotation. IEEE Trans Ultrason Ferroelec Freq Contr 1994; 41(1): 105-122.

[15] Dixon WJ. Ratios involving extreme values. Ann Math Stat 1951; 22(1): 68-78.

[16] Sarkar K, Shi WT, Chatterjee D, Forsberg F. Characterization of ultrasound contrast microbubbles using *in vitro* experiments and viscous and viscoelastic interface models for encapsulation. J. Acoust. Soc. Am 2005; 118(1) 539-550.

[17] Motulsky HJ, Christopoulos A. Fitting Models to biological data using linear and nonlinear regression. A practical guide to curve fitting. San Diego, CA, USA: GraphPad Software Inc., 2003.

[18] Billingsley, P. Probability and Measure. Second Edition, New York: John Wiley & Sons, Inc. 1986.

Chapter 4

Contrast agent signal intensity within vessels for determination of absolute perfusion

4.1 Chapter overview

The preceding chapter described absolute perfusion estimates obtained in a porcine kidney phantom using contrast destruction/refill. The absolute perfusion estimates were obtained through normalization to the renal artery, which provided a measure of the contrast signal intensity corresponding to the perfused agent alone ($A_{100\%}$). The combination of both mean transit time MTT and fractional blood volume FBV (found by normalizing the observed asymptotic value of the refill curve by the perfused agent signal in the reference vessel) gives the absolute perfusion as FBV/MTT. In this chapter, the vessel model is generalized, and a series of experiments is described that test the consistency of the $A_{100\%}$ values obtained across a range of vessel sizes and orientations. In addition, the $A_{100\%}$ values obtained using the vessel model are compared to those obtained using two simpler approaches. The systematic elevation of the values obtained using the vessel model over those obtained otherwise suggests that partial voluming effects are significant in almost all cases one would expect *in vivo* in terms of

extracting $A_{100\%}$ from a vessel. This chapter is adapted from a manuscript that is being prepared for submission to *Ultrasound in Medicine and Biology.*

4.2 Introduction

Contrast-enhanced ultrasound is especially suitable for highlighting capillary flow because ultrasound contrast agent can be assumed non-diffusible [1]. However, current perfusion estimates with ultrasound are typically not absolute and cannot be directly compared with estimates obtained using other methods such as MRI [2]. (MRI perfusion measurements can be made on both relative and absolute bases, although contrast leakage from the circulation is a complicating factor.) Perfusion comparisons between ultrasound and other modalities usually are made only on a relative basis since the ultrasound perfusion measurement is made relative to the asymptotic level of the refill curve A, which denotes the signal intensity level of the tissue in question upon complete filling of its vasculature with contrast. Although related to the fractional blood volume, A also depends upon the contrast concentration of the infusion [3]. Fractional blood volume estimates have been attempted in previous studies by using the cumulative distribution of the power Doppler signal [4] and the cumulative distribution of the contrast echo power [5]. Being able to properly normalize to $A_{100\%}$ would allow comparison of contrast enhanced ultrasound perfusion measurements with those made using other methods and modalities. In addition, proper normalization would generate a standard for perfusion measurements that is neither dependent upon variations in contrast concentration, such as the variations expected between patients (due to differences in circulating blood volume), nor difference in machine settings. Finally, absolute perfusion measurements would

permit the monitoring of perfusion within a given tissue over time, which could provide a means for evaluating the efficacy of treatments that affect blood flow such as anti-angiogenesis therapies.

Two ultrasound studies that have reported absolute perfusion values are a cardiac study [6] and the *in vitro* kidney study described in the previous chapter. The cardiac study used the left ventricle for normalization, while a simplified beam profile model was combined with the renal artery for normalization in the kidney study. A generalized model is presented here which allows use of larger vessels present within an image to normalize the asymptotic value A to the full blood value $A_{100\%}$ in order to obtain the moving fractional blood volume in question. With knowledge of the moving fractional blood volume (FBV) and mean transit time (MTT), the absolute perfusion (given in units of inverse time assuming a tissue density of 1 g/mL) within the tissue could be determined.

4.3 Methods

4.3.1 Beam-corrected vessel model

The vessel in question is modeled as a thin-walled cylinder of infinite length with a constant diameter embedded within a homogeneous tissue. The vessel is oriented in an arbitrary direction relative to the transducer. The underlying signal intensity from contrast present is given by a function $F(x,y,z)$, with x, y, and z giving the spatial location. The value of F is equal to the constant $A_{100\%}$ within the vessel, neglecting attenuation due to overlying contrast. Outside the vessel, F is equal to a constant A_{out}. However, since contrast agent does attenuate the ultrasound traversing it, F is not constant within the

vessel but rather is $A_{100\%}$ ($10^{-0.2\alpha d}$), where α is the effective attenuation coefficient (in dB/unit distance) and d the thickness of overlying contrast as previously described in chapter 3. The vessel orientation in space and axial-lateral plane cross-section are depicted in Fig. 4.1.

The ultrasound beam width in the axial, lateral, and elevational directions (B_{axial}, $B_{lateral}$, and $B_{elevational}$, respectively) are modeled as Gaussian distributions [7] for simplicity. The beam widths in all directions are assumed constant in the region surrounding the vessel. The resultant image I is the two-dimensional convolution of the combination of the axial and lateral point-spread functions $B_{combined}$ with the vessel $F(x,y,z)$ weighted in the z-direction by $B_{elevational}$. Expressed symbolically,

$$I = B_{combined} * \int_{-\infty}^{\infty} [F(x,y,z)][B_{elevational}]dz \qquad \textbf{(4.1)}$$

with the asterisk denoting convolution. With this model, the resulting image can be predicted given any vessel orientation, beam widths, $A_{100\%}$, and A_{out}. This study demonstrates the validity of this model by showing that the predicted values of $A_{100\%}$ for a series of tubes are similar over varying tube sizes. In addition, attempts to obtain $A_{100\%}$ through either taking a global mean or taking a mean while compensating only for attenuation produce $A_{100\%}$ values substantially less than those found using this model.

4.3.2 Transducer axial/lateral beam width measurement

In order to determine the B_{axial} and $B_{lateral}$ values that would be used in this work, the ultrasound contrast agent Definity (Lantheus Medical Imaging Inc., North Billerica, MA, USA) was diluted at a $1{:}2 \times 10^7$ concentration into a container, and imaged with a

Logiq 9 scanner (General Electric Corporation, Milwaukee, WI, USA) using the 7L transducer in coded phase inversion mode. At this extremely low concentration, the contrast agent was assumed to act as single point scatterers, and a series of images were collected. The images were decompressed to a linear scale and subsequently analyzed using a MATLAB (The Mathworks, Inc., Natick, MA, USA) script. The script automatically segmented echoes from individual bubbles and fitted them to two-dimensional Gaussian surfaces based on the selection of regions with a initial threshold value of at least 20 (of a typical range of pixel values of 1 to 80) and expanded the region to include all surrounding pixels with pixels with a value of at least 10 (all in arbitrary intensity units). Doing so was found to reasonably segment the individual echoes from the region in question. The FWHM (full width at half-maximum) values of the fitted surfaces in the axial and lateral directions were respectively recorded as the axial and lateral beam widths. A previous study [8] has shown that microbubbles such as those comprising Definity should be suitable as point targets. The elevational beam width was determined separately from analysis of the tube measurements described below.

4.3.3 Tube flow experiments

Regenerated cellulose dialysis tubing (Spectrum Laboratories Inc., Rancho Dominguez, CA, USA), with nominal diameters of 3.8, 6.4, and 14.6 mm were hydrated and subsequently mounted across an open rectangular container with a length of 16 cm and width of 14 cm. The tubes were connected to a variable-rate peristaltic pump (Cole-Parmer L/S pump and drive, Cole-Parmer Instrument Corporation, Barring, IL, USA), as shown in Fig. 4.2 and a series of two 4-way stopcocks (Medex, Dublin, OH, USA)

allowed flow to be directed to any selected subset of tubes. The tubes were imaged in adjacent pairs (large/medium, medium/small) throughout the course of the experiment in order to permit the comparison of images from each tube. The vessel orientation relative to the transducer (the x-y plane being the axial-lateral plane) is denoted by the angles θ and ϕ.

For a given pair of tubes, the flow rate in each was precisely controlled using a clamp placed before one inlet to partially obstruct the flow, and the flow rates were independently confirmed by timing the delivery of a fixed volume from each tube. By imaging two tubes simultaneously, the comparison of images obtained from each pair becomes independent of possible contrast variation between (and even during) infusions. Specifically, effects arising from variations in contrast agent would simultaneously appear in both tubes.

A constant mean flow velocity of 15 mm/s (determined assuming a circular cross sectional area and aforementioned volume flow rate) was selected in order to ensure that the frames acquired are essentially independent of each other for the 1 Hz imaging frame rate. (Modeling the beam $B_{elevational}$ as a Gaussian, flow at this rate with the tube perpendicular to the axial-lateral plane would pass through almost all, or at least $\pm 3\sigma$, of the beam with each acquired frame for full-width at half maximum beam widths up to 5.9 mm.) The flow velocity was set by adjusting the pump speed to deliver the required volumetric flow rates (measured at the tube outlets) given nominal tube diameters. To reduce specular reflections at the tube walls, an elevational angle ϕ of 10° was selected. Baseline images of the large/medium and medium/small tube pairs were obtained with no contrast agent circulated. Multiple (n=120) images were then obtained of the tube pairs

with the transducer held steady for values of angle θ of 0° and 30° with Definity at a 1:30000 dilution. Values of θ>30° were not examined due to transducer field-of-view limitations (i.e. a larger angle would preclude simultaneous imaging of the tube pairs). The acquisition process was subsequently repeated two additional times for each pair of tubes and both angular positions of θ.

4.3.4 Image analysis

Images from the tube-flow experiments were decompressed to a linear scale. Subsequently, the contrast agent images were baseline subtracted. For every acquisition, a series of 12 averaged images were computed by averaging groups of n=10 frames in order to reduce noise effects. The elevational beam width $B_{elevational}$ was found as follows. All of the averaged images of the medium tube with tilt angles of θ=30°, ϕ=10°, were fitted to the previously described model using a least-absolute residuals criterion, with the axial and lateral beam widths fixed to their previously measured values. The medium tube oriented at θ=30° was selected because (1) it did not appear to suffer from substantial beam refraction effects as was the case with the large tube (the large tube image cross-sections being substantially less elliptical than those expected from its geometry), (2) there were more acquisitions of this tube than the others, due to the manner in which vessel *pairs* were imaged, and (3) its orientation is such that elevational beam width effects are most prominent among the orientations examined. Parameters A, the effective attenuation coefficient α, the tube radius r, and $B_{elevational}$ were determined

by the fit. The mean value of $B_{elevational}$ was used as the elevational beam width through the remainder of this analysis.

Subsequently, all of the averaged images were individually fit to the beam-corrected vessel model with $B_{elevational}$ fixed to its value as determined above and thus obtaining values of A, α, and r for each tube size at every orientation and acquisition. Values of A were next compared between tube sizes at each orientation, and to values that would have been obtained had one used (1) the global mean observed intensity value within the vessel, and (2) the intensity value within the vessel, compensating only for the effective contrast attenuation obtained. The latter attenuation-only model is computed through fitting the observed pixel intensity values to a decaying exponential expression $A \cdot 10^{-0.2\alpha d}$ in the axial direction, where d is the axial distance, to global values of A and α as illustrated in Fig. 4.3.

4.4 Results

4.4.1 Transducer beam widths

Following the methods described in 4.3.2, the full-width at half maximum (FWHM) values of the axial and lateral point-spread function were measured (n=2520) to be (±1 standard deviation) respectively 0.87±0.26 mm and 1.25±0.38 mm. After fixing the axial and lateral beam widths at these estimated values, the elevational beam width was found to be 1.53±0.60 mm (n=69) using the methods described in 4.3.4. Three images with fitted elevational beam widths of zero were excluded due to the physical impossibility of a zero elevational beam width. An example of an image showing the

points present in the container, indicative of the axial and lateral beam widths, is shown in Fig. 4.4 along with histograms showing the distribution of the measured values.

4.4.2 Sample images and fit results

Sample images of each acquisition for each vessel pair and orientation are illustrated in Fig. 4.5. Slight variations in the distances to the transducer are present between acquisitions for given vessel pairs and orientations. Examples of small, medium, and large averaged images (from n=10 frames) and their fits and residuals are plotted in Fig. 4.6 in false color. Note from the difference image how the error is concentrated at the vessel edges, with the model closely tracking what is observed in the vessel interiors. In addition, the fact that the observed cross-sections are less elliptical than those predicted by the model suggests that refraction artifact is present, presumably due to the vessel wall.

4.4.3 Comparison of estimated $A_{100\%}$ values

A comparison of the estimated $A_{100\%}$ values using the beam-corrected vessel model for each vessel pair taken at each orientation is plotted in Fig. 4.7, with each symbol denoting the results from a single acquisition for an average of n=10 frames each (frames consisting of those immediately following the previous timepoint to the indicated one inclusive). Although the $A_{100\%}$ values between individual acquisitions sometimes vary substantially, the ratio of the $A_{100\%}$ values between tube sizes remain relatively close to 1. Analogous plots for the global mean and attenuation-only models are shown in Fig.

4.8 and Fig 4.9. The average ratios (averaged from all 3 acquisitions) for each pair of tubes at each orientation using each model are summarized in Table 4.1. With the exception of only one case, the beam-corrected vessel model yielded ratios between tubes that were closer to the expected value of 1 than the two simpler models, suggesting the correctness of this approach.

4.4.4 Comparison to global mean and attenuation model

Estimates of $A_{100\%}$ for each acquisition for each vessel computed from the vessel model are compared to the results from the global mean and attenuation-only model in Fig. 4.10. The global mean and attenuation-only models generally produce results that are less than those obtained from the beam-corrected vessel model proposed here. Since the observed attenuation for the contrast concentration used was small, the attenuation-only model typically produced results similar to those from the global mean. The estimated $A_{100\%}$ values obtained using the vessel model were on average 1.71±0.55 and 1.71±0.49 times, respectively, of that found using the global mean and attenuation-only model for the small vessel, 1.43±0.89 and 1.38±1.05 times for the medium vessel, and 1.15±0.08 and 1.10±0.05 times for the large vessel. Increases in vessel size correlate with decreases of the ratio of the estimated $A_{100\%}$ found using the vessel model to that estimated using the other two approaches. This correlation is probably due to the decreasing role of partial voluming with increasing vessel size. The differences between the values obtained using the global mean and the attenuation-only model were slight throughout, due to the low attenuation due to contrast.

4.5 Conclusions and discussion

The estimation of absolute perfusion using ultrasound contrast agents requires a measure of the signal intensity ($A_{100\%}$) for pure dilute contrast. A model has been presented that accounts for both partial voluming and contrast attenuation within a vessel being used to normalize for $A_{100\%}$ in a contrast agent based perfusion measurement. The model has been shown to give results that were more consistent across vessel sizes at differing orientations than those obtained using two simpler approaches. Approaches such as taking the global mean and attempting to solely account for contrast attenuation tend to underestimate $A_{100\%}$. *In vivo*, the available vessels would tend to be smaller than those examined in this study, further exaggerating the effects arising from partial voluming.

Due to phase-aberration effects, the effective beam widths in an *in vivo* scan cannot be directly derived from the *in vitro* measurements described here. A substantial beam widening has been reported [9]. However, the axial and lateral beam widths in the focal zone and far field can be approximated by examining the speckle pattern, and noting the speckle spot size [10]. The elevational beam width could then be estimated by combining Doppler data from the vessel, which would provide velocity information, and the speckle decorrelation rate in a manner analogous to that described in [11]. In the near field, the speckle pattern is fine due to the incoherent nature of the beam, and the decorrelation is not indicative of the beam widths [12].

The model presented does not account for focusing gain or refraction artifacts. The two effects might be substantial enough to affect the estimation of $A_{100\%}$. First, focusing gain would potentially play a much larger role in a strongly focused transducer,

where echoes from scatterers located near the focus are significantly stronger than echoes arising elsewhere. Experimentally, if a pair of tubes were compared and one tube were located nearer to the focus than the other, identical contrast agent would have differing echogenicity, and different estimates of $A_{100\%}$ would result. For larger tubes, parts of the image may be brighter than other parts due to this effect rather than contrast attenuation.

Looking at Fig. 4.6, one observes some level of refraction artifact due to the tube wall's refraction of the ultrasound beam. The refraction causes the images to appear less elliptical than expected from their geometry alone. *In vivo*, refraction has been known to cause the appearance of doubling of cardiac structures [13] as well as artifacts in imaging pediatric spinal cords [14]. Refraction has been previously known to cause images of the underlying geometric structures to become distorted (e.g. reported in a phantom in [15]). For a 2D scan *in vivo*, refraction artifact can cause the vessel geometry to be misjudged and cause an error in the estimate of $A_{100\%}$.

For a 3D/4D scan *in vivo*, refraction artifact is expected to play less of a role since the artifact generally is not uniform. The vessel geometry can be further refined from the straight circular cylinder modeled here with the actual vessel geometry applied toward estimating $A_{100\%}$. Knowledge of the echogenicity of the tissues surrounding the vessel would allow more accurate modeling of partial voluming effects through the improved estimation of A_{out}. Small errors in the estimation of $A_{100\%}$ cause the estimated FBV to have an error of approximately the same percentage in the opposite direction. That is, underestimating $A_{100\%}$ by 10% would cause FBV, and hence perfusion, to be overestimated by ~10%. Partial voluming effects have been shown to play a significant role in the signal intensity level observed in a major vessel. Properly compensating for

partial voluming and (depending on the contrast concentration) contrast attenuation is required in order to correctly estimate $A_{100\%}$. The vessel model presented accounts for both of these phenomena.

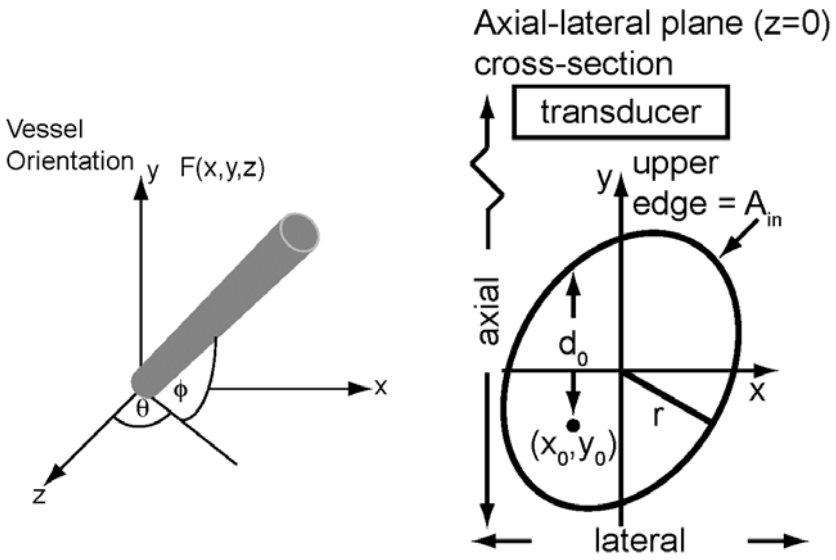

Fig. 4.1. Vessel geometry and orientation. The vessel is modeled as a cylindrical tube of infinite length oriented arbitrarily in space. *F(x,y,z)* denotes the intensity level of contrast at any location *(x,y,z).* The intersection of the vessel with the axial-lateral plane is an ellipse with vessel radius *r*. The angles θ and ϕ, which determine the orientation of the tubing relative to the transducer are also depicted.

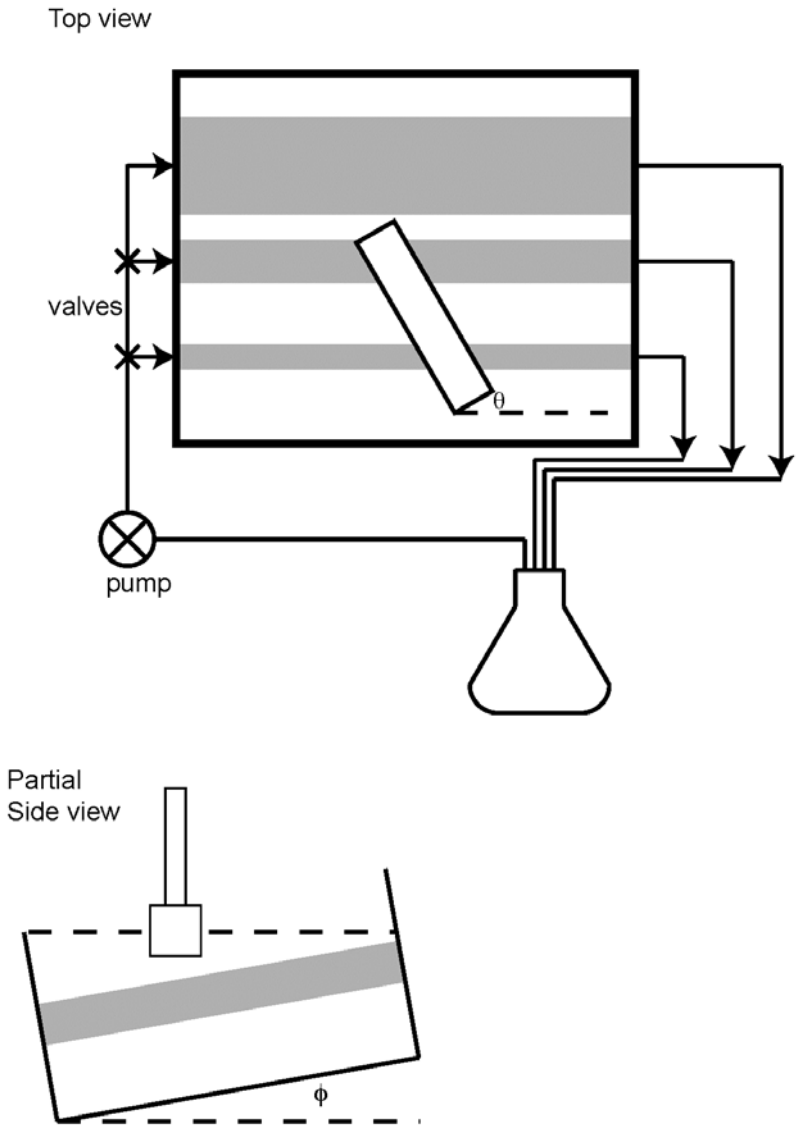

Fig. 4.2. Experimental setup. Three pieces of dialysis tubing (Spectrum Laboratories Inc., Rancho Dominguez, CA, USA) were mounted across a water-filled container and connected to a variable rate pump as shown. The pump drew dilute contrast (1:30000 in water) from a stirred flask and pumped it through a selected pair of tubes. A clamp was used before one of the inlets on each pair of tubes being imaged at a given time in order to control the flow to each. The contrast agent then was returned to the flask. The angles θ and ϕ, determining the orientation of the tubing relative to the transducer, are implemented as shown.

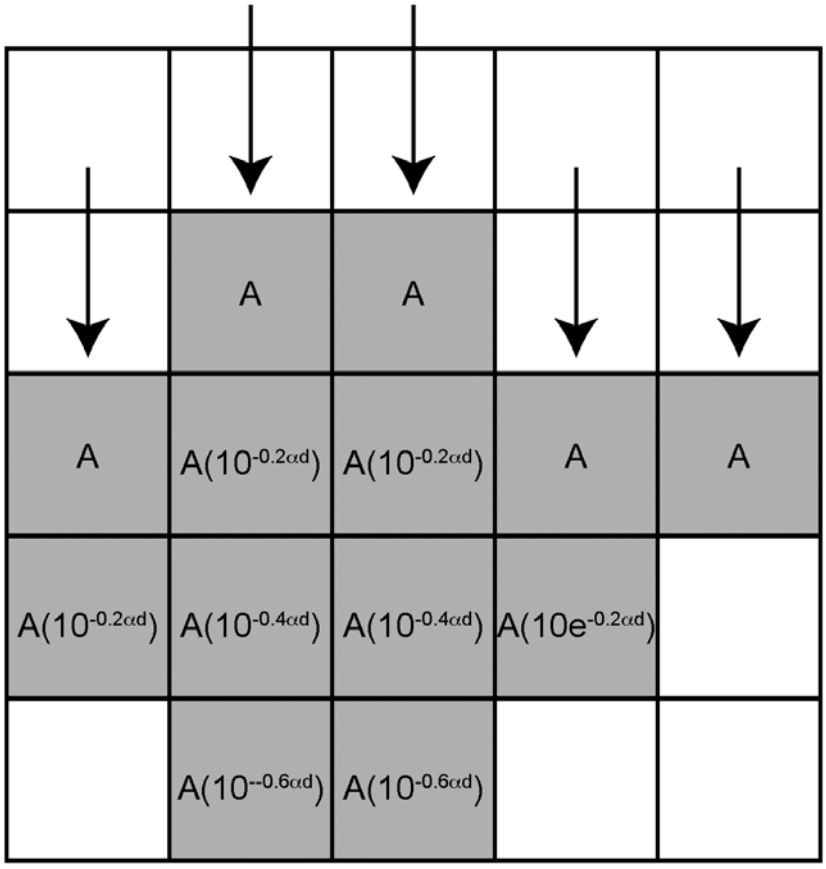

Fig. 4.3. Attenuation-only model. The attenuation-only model takes the pixels composing the vessel cross-section, and assigns the edge nearest the transducer the value A. Pixels located at various distances away from the upper edge are assigned attenuated values consistent with their distance. Both A and the attenuation coefficient α are global parameters that are fitted to constant values that minimize the absolute difference between the observed and fitted values.

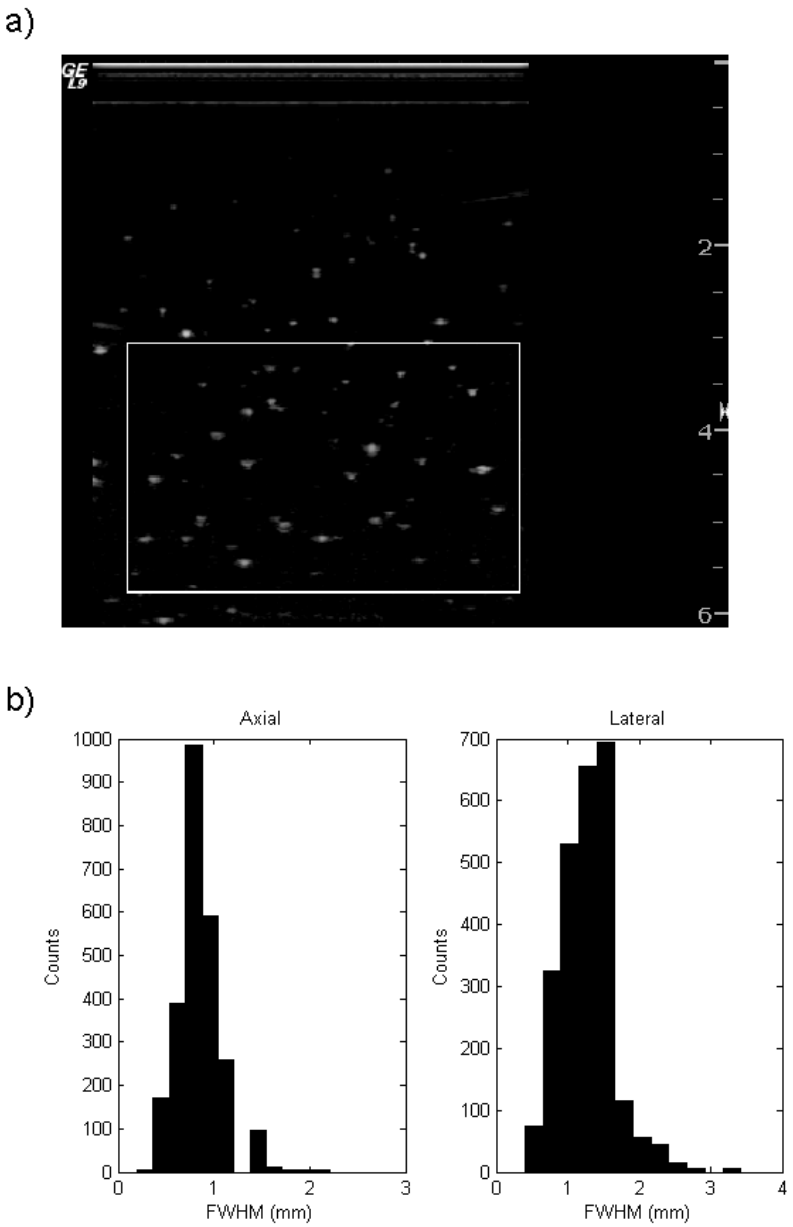

Fig. 4.4. – Sample image of axial-lateral point-spread function measurement. a) The box delineates the range from which points were selected from the image by an automated script used to measure axial and lateral beam widths. The selected range covers the distance to the tubes of Fig. 4.2 from the transducer. Numerals on the right denote axial distance to the transducer face in cm. b) Histograms of the distribution of the measured axial and lateral beam widths.

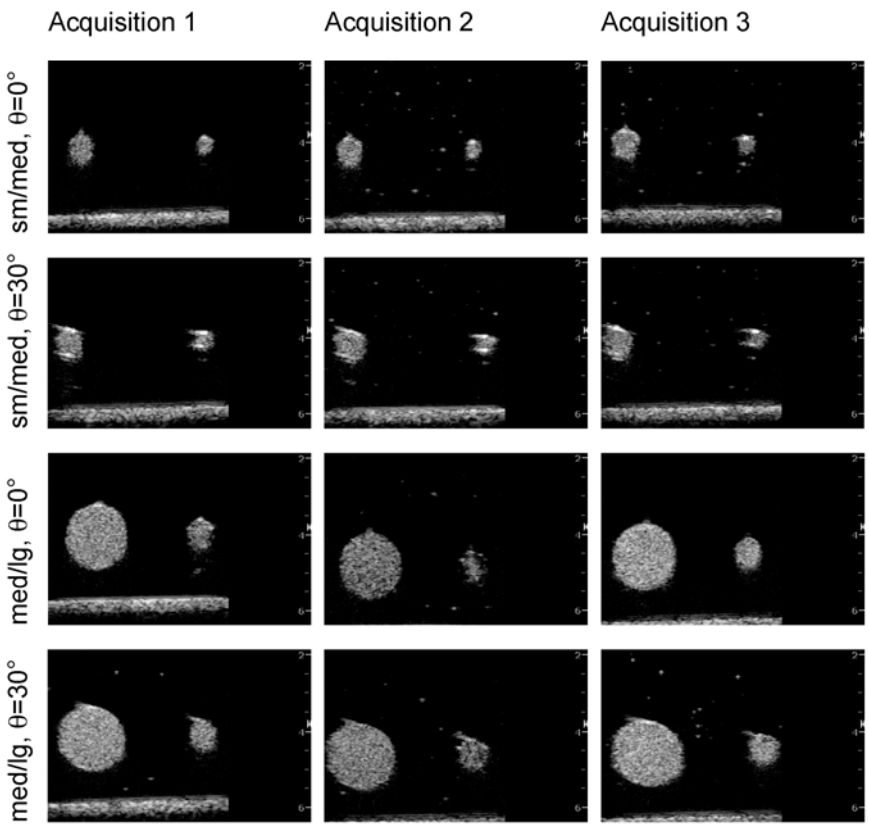

Fig. 4.5. Sample images of tube cross-sections. Images of the tubes are shown for each acquisition at each orientation. Images are shown of an individual frame. The scale ranges from 2-6 cm.

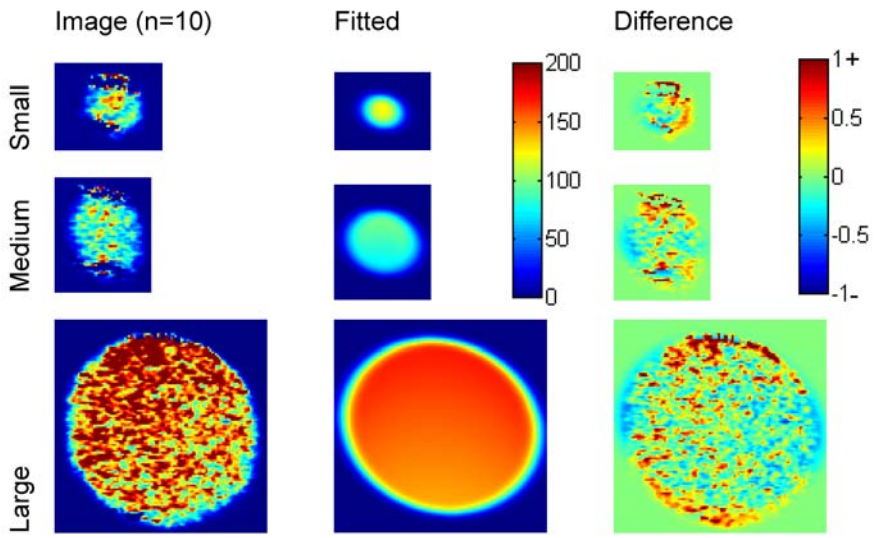

Fig. 4.6. – Sample average tube subtraction false-color images and fit results. Sample average subtraction images (calculated from n=10 frames) for the θ=30° case are illustrated for vessels of each size in the first column together with their fitted images in the second column and the differences between these in the third. Note how the model fits the observed images especially well around the tube center, with the majority of error occurring near the edges. The mean and fitted images are shown in arbitrary intensity units. The difference images are displayed as (measured-fitted)/estimated $A_{100\%}$.

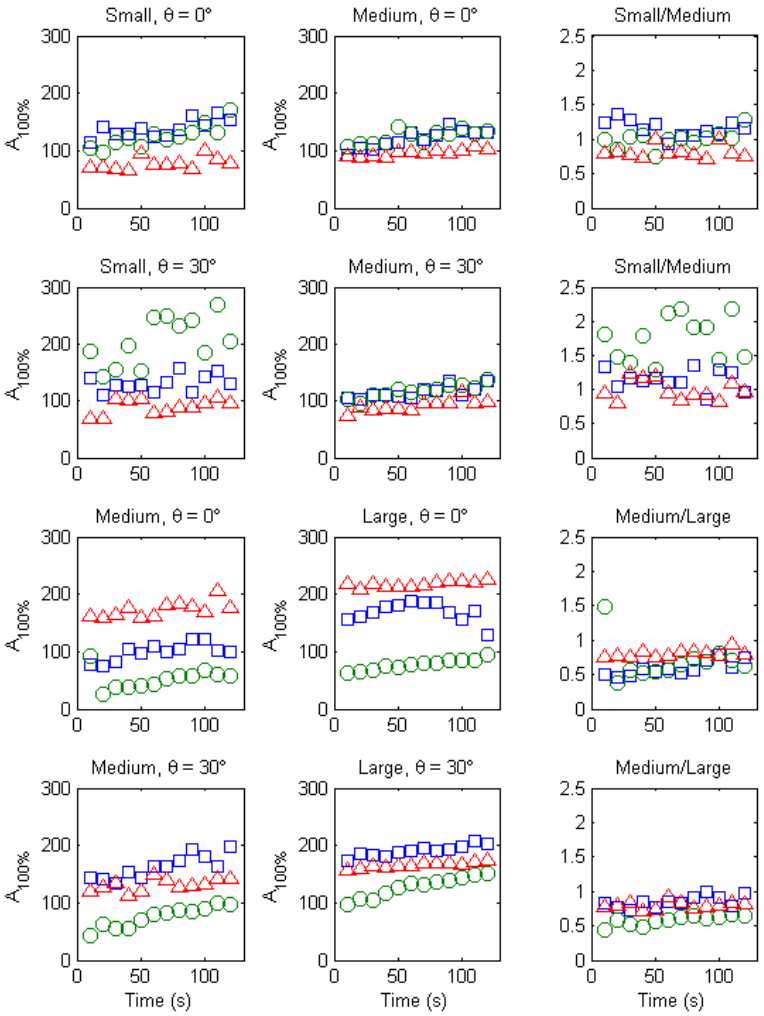

Fig. 4.7. $A_{100\%}$ values for vessel pairs found with the beam-corrected vessel model. Plotted in the left two columns are the fitted values of $A_{100\%}$ in arbitrary intensity units for each vessel and angle θ that was examined as a function of the composite image (calculated from the average of n=10 individual frames). Different symbols denote results from different acquisitions. Plotted in the right column are the ratios of the $A_{100\%}$. The ratios are near 1, as expected (details in text).

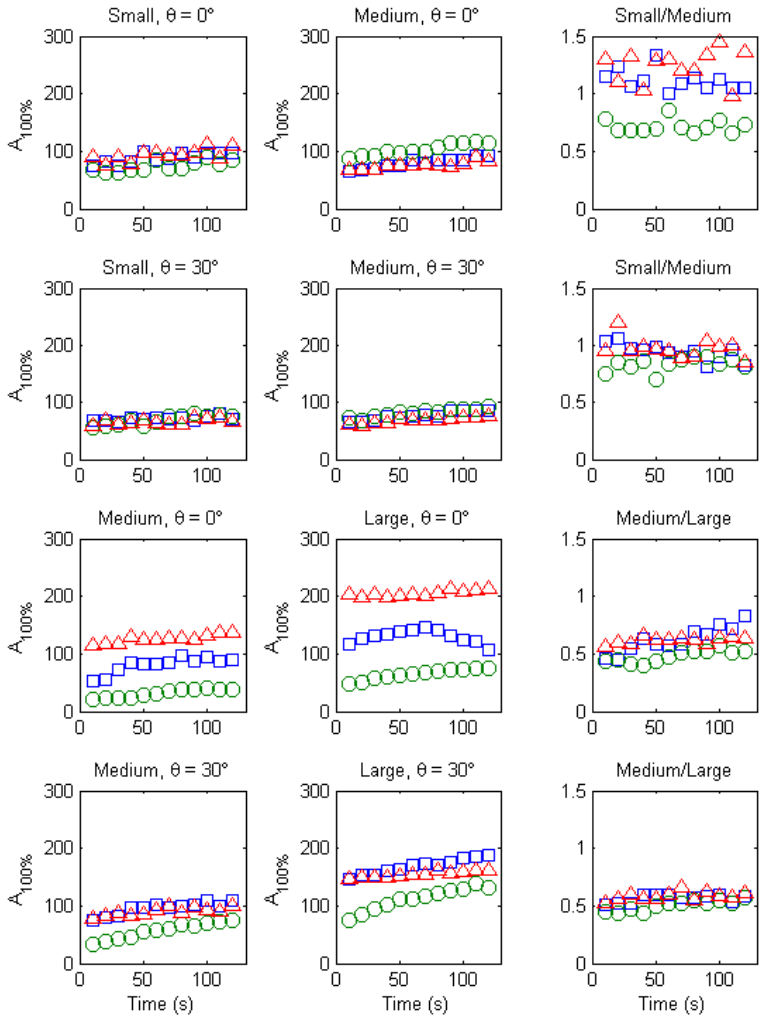

Fig. 4.8. Global mean estimates of $A_{100\%}$. Analogous to Fig. 4.7 are the values obtained using the global mean of the vessel. Notice how, although the numbers may be closer between acquisitions, the ratios tend to be farther from the expected value of 1.

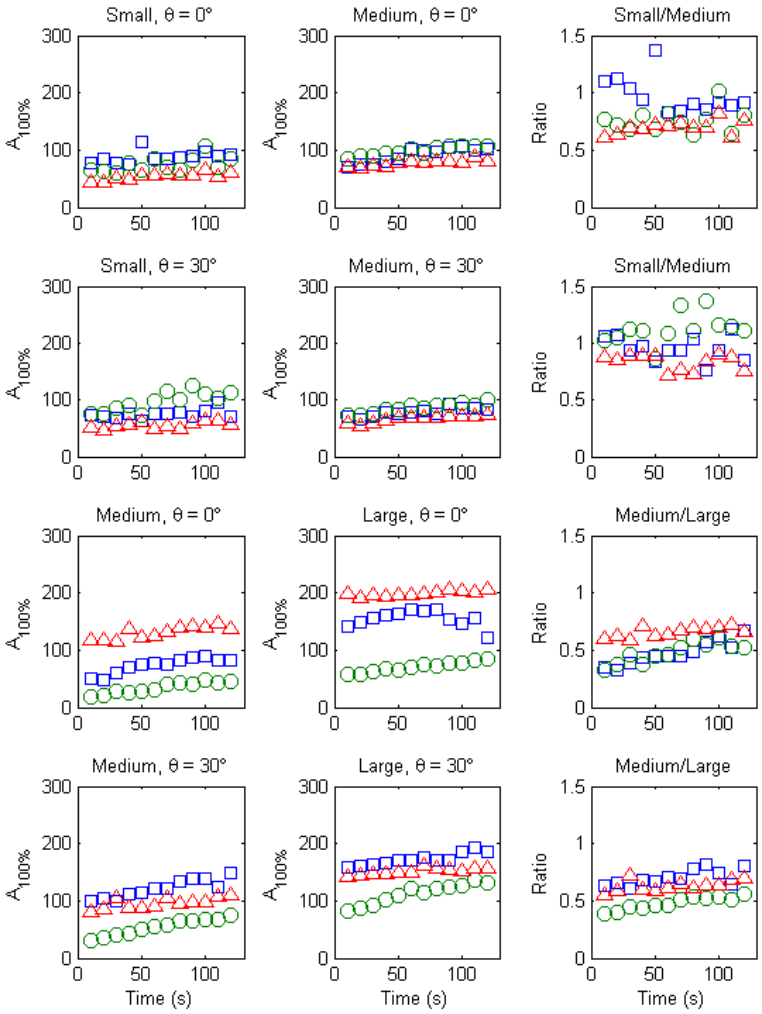

Fig. 4.9. Attenuation-only model estimates of $A_{100\%}$. The attenuation-only model produces results similar to those from the beam-corrected vessel model, and with variation. However, as will be shown in Fig. 4.10, both the global mean and attenuation-only models underestimate the value of $A_{100\%}$ since partial voluming is neglected.

Tube pair	θ (degrees)	Beam-corrected vessel model	Global mean	Attenuation-only model
Small/medium	0	0.99 ± 0.19	1.02 ± 0.18	0.81 ± 0.20
Small/medium	30	1.29 ± 0.38	0.92 ± 0.13	0.97 ± 0.18
Medium/large	0	0.69 ± 0.30	0.57 ± 0.13	0.54 ± 0.14
Medium/large	30	0.74 ± 0.12	0.55 ± 0.07	0.60 ± 0.10
All cases	————	0.93 ± 0.53	0.77 ± 0.27	0.73 ± 0.32

Table 4.1. Comparison of vessel models. The beam-corrected vessel model on average predicted ratios of $A_{100\%}$ that were closer across tubes, with the exception being the small/medium pair at θ=30°. Although there is more variation overall in the beam-corrected vessel model results, the proximity of the ratio of the estimated values of $A_{100\%}$ suggests the overall correctness of this approach.

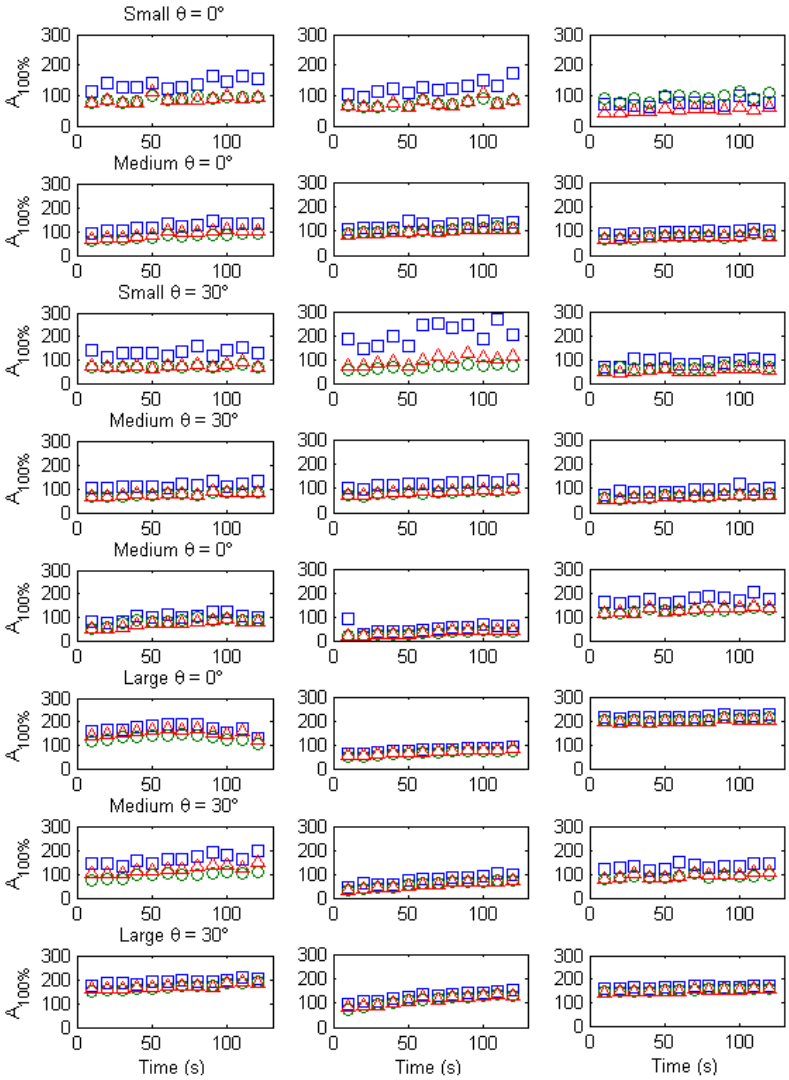

Fig. 4.10. Comparison of $A_{100\%}$ values found with beam-corrected vessel model versus other estimates. For each vessel oriented at each orientation, estimated $A_{100\%}$ values are plotted. Columns denote individual acquisitions. The squares, circles, and triangles denote respectively the estimated values as found with the vessel model, global mean, and attenuation-only models. The values obtained from the vessel model are substantially greater from those obtained from the presented simpler approaches (details in text).

4.6 References

[1] Lucidarme O, Kono Y, Corbeil J, Choi SH, Golmard JL, Varner J, Mattrey RF. Angiogenesis: Noninvasive Quantitative Assessment with Contrast-enhanced Functional US in Murine Model. Radiology 2006; 239(3):730-739.

[2] Yankeelov TE, Niermann KJ, Huamani J, Kim DW, Quarles CC, Fleischer AC, Hallahan DE, Price RR, Gore JC. Correlation between estimates of tumor perfusion from microbubble contrast-enhanced sonography and dynamic contrast enhanced magnetic resonance imaging. Ultrasound Med Biol 2006; 25: 487-497.

[3] Wei K, Jayaweera AR, Firoozan S, Linka A, Skyba DM, Kaul S. Quantification of Myocardial Blood Flow With Ultrasound-Induced Destruction of Microbubbles Administered as a Constant Venous Infusion. Circulation 1998; 97(5): 473-483.

[4] Rubin JM, Bude RO, Fowlkes JB, Spratt RS, Carson PL, Adler RS. Normalizaing Fractional Moving Blood Volume Estimates with Power Doppler US: Defining a Stable Intravascular Point with the Cumulative Power Distribution Function. Radiology 1997; 205: 757-765.

[5] Potdevin TCU, Fowlkes JB, Moskalik AP, Carson PL. Refill model of rabbit kidney vasculature. Ultrasound Med Biol 2006; 32(9): 1331-1338.

[6] Vogel R, Indermuhle A, Reinhardt J, Meier P, Siegrist PT, Namdar M, Kaufmann PA, Seiler C. The quantification of absolute myocardial perfusion in humans by contrast echocardiography – Algorithm and validation. J Am Coll Cardiol 2005; 45(5): 754-762.

[7] Kallel F, Bertrand M, Meunier J. Speckle Motion Artifact Under Tissue Rotation. IEEE Trans Ultrason Ferroelec Freq Contr 1994; 41(1): 105-122.

[8] Psychoudakis D, Fowlkes JB, Volakis JL, Carson PL. Potential of Microbubbles for Use as Point Targets in Phase Aberration Correction. IEEE Trans Ultrason Ferroelec Freq Contr 2004; 51(12): 1639-1648.

[9] Anderson ME, McKeag MS, Trahey GE. The impact of sound speed errors on medical ultrasound imaging. J. Acoust. Soc. Am 2000; 107(6): 3540-3548.

[10] Smith SW, Trahey GE, Hubbard SM, Wagner RF. Properties of acoustical speckle in the presence of phase aberration part II: correlation lengths. Ultrasonic Imaging 1988; 10:29-51.

[11] Rubin JM, Fowlkes JB, Tuthill TA, Moskalik AP, Rhee RT, Adler RS, Kazanjian

SN, Carson PL. Speckle decorrelation flow measurement with B-mode US of contrast agent flow in a phantom and in a rabbit kidney. Radiology 1999; 213(2): 429-437.

[12] Tuthill TA, Krücker JF, Fowlkes JB, Carson PL. Automated Three-dimensional US Frame Positioning Computed from Elevational Speckle Decorrelation. Radiology 1998; 209(2): 575-582.

[13] Spieker LE, Hufschmid U, Oechslin E, Jenni R. Double aortic and pulmonary valves: An artifact generated by ultrasound refraction. J Am Soc Echocardiogr 2004; 17(7): 786-787.

[14] Austin MJ, Gerscovich EO, Fogata M, Gillen MA, Bijan B. Sonographic duplication artifact of the spinal cord in infants and children. J Ultrasound Med 2004; 23(6): 799-803.

[15] Weichselbaum RC, Feeney DA, Jessen CR, Osborne CA, Dreytser V, Holte J. Relevance of sonographic artifacts observed during *in vitro* characterization of urocystolith mineral composition. Vet Radiol Ultrasound 2000; 41(5): 438-446.

Chapter 5

Conclusions and future work

5.1 Summary: Imaging of contrast agent in three/four dimensions

This dissertation has examined the imaging of ultrasound contrast agent in three dimensions and the methods of perfusion estimation. Three-dimensional imaging is possible using either a one-dimensional linear array that is mechanically translated or a two-dimensional array. A mechanical system was constructed that translated one-dimensional arrays in the elevational direction, thereby acquiring volumetric images.

Volumetric imaging of contrast agent was performed, first in the tube phantom in order to test its effectiveness in imaging contrast refill with a known theoretical profile. In the tube phantom, the observed contrast profiles were visually compared to their theoretical counterparts, and they were largely in agreement, except at the center of the leading edge. The differences there were probably caused by slight contrast destruction since contrast located at that location was preferentially insonated. In spite of those differences, estimated center velocity values did not statistically differ from values expected based on the known flow rates.

The mechanical system was subsequently used to scan a perfused kidney phantom. Properly normalizing the refill curve was necessary to correct for contrast decay over the course of the lengthy *in vitro* experiment. A vessel model was developed that accounted for (1) vessel geometry, (2) beam shape and its associated partial

voluming, and (3) vessel position. The normalization process also enabled estimates of the fractional blood volume (FBV) to be made. Absolute perfusion was estimated based on the normalized refill curves at two different infusion rates, and the values obtained for the slice in question using the dual transducer apparatus and interval imaging did not differ, which suggests the independence of perfusion measurements from contrast clearance patterns.

Finally, the beam-corrected vessel model which accounts for both partial voluming and contrast attenuation was developed that allows estimation of the signal level corresponding to 100% "blood," or $A_{100\%}$. The model was tested in three perfused tubes, and was shown to yield consistent values over varying tube sizes. In addition, the model was shown to produce $A_{100\%}$ values that were greater than those found using the global mean and an attenuation-only model, indicating the importance of correcting for partial voluming.

Imaging in three spatial dimensions is widely believed to be advantageous over imaging in two, due to the additional information obtained. The imaging of contrast agent in three/four dimensions was studied, and the key results of this work are summarized below.

5.2 Experimental conclusions

<u>CONTRIBUTION 1</u>: Volumetric contrast clearance and imaging is achievable through the use of a pair of 1D linear arrays.

(Results are published in [1].)

The dual transducer technique, illustrated in chapter 2, produced volumetric images consistent with the parabolic velocity profiles of viscous laminar flow. Contrast clearance followed by imaging with a transducer set to a minimally destructive power produced images with expected contrast cross-sections. The imaging process, incidentally, was not completely non-destructive, which accounts for the small discrepancies observed at the "tip" of the profile. Nevertheless, center velocity estimates did not differ statistically from those expected from theory. Due to the requisite acquisition time for the translating probes the contrast position profile over time was derived as a function of both tube diameter and time in order to compare experiment to theory. The end result was the demonstration that the dual transducer technique permits the investigation into the dynamics of volumetric contrast destruction/refill without the need for a 2D array.

CONTRIBUTION 2: **A vessel model was developed in order to correct for contrast instability through the use of a major vessel, as well as to estimate the echo intensity level corresponding to the contrast agent $A_{100\%}$.** The model, described in chapter 3 and further developed in chapter 4, accounts for both partial voluming and contrast attenuation. Not only does the model correct for contrast decay, but it also allows normalization of points on the refill curve to the value of $A_{100\%}$. Although contrast decay is not expected to play a significant role in most studies *in vivo* due to shorter acquisition times, being able to correct for variations in contrast concentration nevertheless would allow for studies of longer duration. In addition, compensation for contrast variations over the course of an infusion would be achieved. Proper accounting for contrast

attenuation and partial voluming was shown to be essential in correctly estimating $A_{100\%}$. This normalization allows one to estimate the filled fractional blood volume and contrast mean transit time in question if the refill curve extends sufficiently to delineate its asymptotic value.

CONTRIBUTION 3: **Absolute perfusion was estimated from the normalized refill curve.** Given knowledge of both the contrast mean transit time (MTT) and the fractional blood volume (FBV) absolute perfusion is simply FBV/MTT if a tissue density of 1 g/mL is assumed. The FBV can be estimated through a proper normalization to a major vessel, assumed filled with contrast, present within the image. Normalized refill curves had their initial slopes recorded as perfusion in the study with the kidney phantom described in chapter 3. At the high flow rate, the slopes yielded absolute perfusion values that were consistent with those found in the literature using thermal diffusion [2].

CONTRIBUTION 4: **In cases where the acquired portions of the refill curve do not adequately delineate the FBV, perfusion was estimated regardless.** Since perfusion is the initial slope of the refill curve, perfusion can be estimated by fitting the acquired portions of the refill curve using the linear fit in spite of the inability to estimate the FBV and MTT separately under such circumstances. The near-equivalence of the linear fit results and corresponding exponential fit perfusion results is illustrated in Fig. 3.15. In cases where FBV and MTT cannot be separately estimated, their combination FBV/MTT (absolute perfusion) can still be accurately estimated due to the effects of covariance as described in appendix C of chapter 3.

CONTRIBUTION 5: In a perfused tissue that has been cleared of contrast, contrast refill is dominated by capillary filling; as such, the refill is independent of the pattern in which contrast was cleared. As seen in Fig. 3.12, the lack of a difference in perfusion estimates obtained using the dual transducer technique and those using interval imaging of the kidney phantom at the selected transducer position suggests that contrast refill is essentially independent of the clearance volume. This independence is probably due to the refill being dominated by capillary filling since the major vessels refill promptly after clearance.

5.3 Future experimental directions

5.3.1 Verification of kidney phantom perfusion values

The kidney phantom, in which absolute perfusion values were estimated as described in chapter 3, should have the perfusion measurements compared to a standard technique such as microspheres in order to verify the accuracy of the new technique. Microsphere studies provide an independent "gold-standard" measure of absolute perfusion. The studies can be conducted using radiolabeled [3], colored [4-6], X-ray fluorescent [7], or neutron-activated microspheres [8]. Previous studies such as the tissue occlusion study [9] have used microspheres to verify changes in perfusion in kidneys. Independent measurement of fractional blood volume (FBV) should also be investigated to determine the relative contributions to perfusion by FBV and blood flow velocity. Measurement of FBV can be obtained using labeled particles such as ^{99m}Tc to label circulating red blood cells [10], or through the injection of a fluorescent dye, as described

in the xenografted tumor study [11]. However, the size of the capillaries in the fixed kidney would need to be measured or some means determined to ensure the presence of free circulation.

5.3.2 Investigation of phase-aberration effects

When an ultrasound beam passes through tissue, the beam is distorted due to phase aberration as mentioned in chapter 4. This distortion causes the beam to widen, and also causes its shape to deviate from its unaberrated form. The extent to which the model presented in chapter 4 can continue to be effectively applied with phase-aberration effects present should be investigated by repeating the experiments described there with the addition of one or more phase aberrators (constructed as described in [12]) and examining the resultant estimated $A_{100\%}$ values. One would expect results to degrade with increases in phase-aberration, even after compensating for the increases in beam width because of the changes in beam shape that occur. The level of degradation that occurs and the amount of error introduced to $A_{100\%}$ estimates should be quantified.

5.3.3 Effect of normalization vessel size relative to point-spread function

The experiments described in chapter 4 covered a range of vessel diameters from 3.8 mm to 14.6 mm. *In vivo*, one would expect normalization vessels to be smaller than those investigated. Since the degree of partial voluming is a function of the ratio of the vessel size to the point-spread function, more comprehensive studies on a larger range of tubes, with an emphasis on smaller tubes, should be performed. In addition, the level of accuracy that one obtains of the $A_{100\%}$ estimates as both a function of frame averaging

and vessel size to point-spread function ratio should be quantified. Finally, the minimum vessel size to point-spread function ratio necessary to obtain a sufficiently accurate estimate of $A_{100\%}$ needs to be determined.

5.3.4 Effect of variations in background tissue

The experiments described in chapter 4 were conducted with vessels that were suspended in water. How well the described model accounts for non-zero backgrounds, as well as variable backgrounds such as that found in actual tissues will need to be studied. First, parallel tubes (as seen in Fig. 4.2) should be studied in a two-compartment phantom with a watertight barrier separating the tubes. One half of the phantom can then be filled with a nonzero background using contrast diluted relative to that present within the tubes. This setup would allow direct comparison of the background effects in a manner similar to that in chapter 4. Second, additional information may be available from the combination of estimated $A_{100\%}$ values obtained at differing background levels, such as that obtained during a refill sequence as the background tissue refills. These dynamic effects may permit more accurate estimates of $A_{100\%}$ than those available from individual image frames. Finally, the background could also contain scatterers that are not contrast agent such that the level of static signal could be adjusted to match that level not cancelled by the contrast imaging pulse sequence. This would provide a more realistic assessment of the contrast imaging and normalization process under controlled conditions.

5.3.5 Effect of increased contrast attenuation within vessel

The experimental vessels described in chapter 4 had relatively little attenuation due to the contrast present. As such, estimates of $A_{100\%}$ made using the simple mean and the attenuation only model were quite similar, even though they were both less than the vessel model estimate. An increase in contrast concentration such as to the 1:5000 level used in the study described in chapter 3 would be expected to increase the effect of contrast attenuation and this increase would be expected to cause the simple mean and attenuation only model results to diverge. Studies should be conducted in order to test under which circumstances contrast attenuation would be significant *in vivo*; concentrations *in vivo* may be higher, but smaller vessel size tends to mitigate the effect.

5.3.6 Applications to 2D arrays

The development of commercially available two-dimensional arrays, which allow the direct acquisition of complete image volumes with a single transducer, has made the study of contrast destruction and refill *in vivo* in four-dimensions feasible. Scans *in vivo* would combine background variations as well as vessel variations and phase-aberration effects. The contrast normalization model should be tested *in vivo* in order to obtain absolute perfusion maps. The maps could be displayed in a manner analogous to that used in power Doppler. These results would then be verified through comparison with absolute perfusion measurements made otherwise. With acquisitions that are sufficiently complete such that all three parameters of the refill curve (FBV, MTT, and perfusion) can be reliably estimated, three-dimensional studies of these parameters in distinguishing between benign and malignant tumors using contrast-enhanced ultrasound could be undertaken. Since FBV has been reported in few studies, ultrasound contrast agent

studies using the normalization presented may provide a means to measure FBV for a variety of tissues. In addition, the result of tumor treatment on these parameters could be monitored over time.

5.4 References

[1] Chen NG, Fowlkes JB, Carson PL, LeCarpentier GL. Rapid 3D Imaging of Contrast Flow: Demonstration of a Dual Beam Technique. Ultrasound Med Biol 2007; 33(6) 915-923.

[2] Kraus T, Klar E, Osswald BR, Fernandes L, Mehrabi A, Gebhard MM, Herfarth C. Continuous Measurement of Porcine Renal Cortex Microcirculation with Enhanced Thermal Diffusion Technology. J Surg Res 1996; 61(2): 531-536.

[3] Rudolph AM, Heymann MA. The circulation of the fetus *in utero.* Circ Res 1967; 21: 163-184.

[4] Hale SL, Alker KJ, Kloner RA. Evaluation of nonradioactive, colored microspheres for measurement of regional myocardial blood flow in dogs. Circulation 1988; 78: 428-434.

[5] Kowallik P, Schulz R, Guth BD, Schade A, Paffhausen W, Gross R, Heusch G. Measurement of regional myocardial blood flow with multiple colored microspheres. Circulation 1991; 83: 974-982.

[6] Glenny RW, Bernard S, Brinkley M. Validation of fluorescent-labeled microspheres for measurement of regional organ perfusion. J Appl Physiol 1993; 74: 2585-2597.

[7] Mori H, Haruyama S, Shinozaki Y, Okino H, Iida A, Takanashi R, Sakuma I, Husseini WK, Payne BD, Hoffman JIE. New nonradioactive microspheres and more sensitive X-ray fluorescence to measure regional blood flow. Am J Physiol 1992; 263: H1946-H1957.

[8] Reinhardt CP, Dalhberg S, Tries MA, Marcel R, Leppo JA. Stable labeled microspheres to measure perfusion: validation of a neutron activation assay technique. Am J Physiol Heart Circ Physiol 2001; 280: H108-H116.

[9] Kripfgans OD, Orifici CM, Carson PL, Ives KA, Eldevik OP, Fowlkes JB. Acoustic droplet vaporization for temporal and spatial control of tissue occlusion: A kidney study. IEEE Trans Ultrason Ferr Freq Cont 2005; 52(7): 1101-1110.

[10] Desai AG, Thakur ML. Radiolabeled blood cells: techniques and applications. Crit Rev Clin Lab Sci 1986; 24(2): 95-122.

[11] Wall A, Persigehl T, Hauff P, Licha K, Schirner M, Müller S, von Wallbrunn A, Matuszewski L, Heindel W, Bremer C. Differentiation of angiogenic burden in human cancer xenografts using a perfusion-type optical contrast agent (SIDAG). Breast Cancer Res 2008; 10(2): R23.

[12] Krücker JF, LeCarpentier GL, Fowlkes JB, Carson PL. Rapid Elastic Image Registration for 3-D Ultrasound. IEEE Trans Med Imaging 2002; 21(11): 1384-1394.